2010

Study on electrolytic plasma discharging behavior and its influence on the plasma electrolytic oxidation coatings

Riyad Omran Hussein
University of Windsor

Study on electrolytic plasma discharging behavior and its influence on the plasma electrolytic oxidation coatings

by

Riyad Omran Hussein

A Thesis

Submitted to Faculty of Graduate Studies

through Materials Engineering

in Partial Fulfilment of the Requirements for

the Degree of Master of Applied Science at the

University of Windsor

Windsor, Ontario, Canada

2010

Library and Archives
Canada

Bibliothèque et
Archives Canada

Published Heritage
Branch

Direction du
Patrimoine de l'édition

395 Wellington Street
Ottawa ON K1A 0N4
Canada

395, rue Wellington
Ottawa ON K1A 0N4
Canada

NOTICE:

AVIS:

Canada

DECLARATION OF CO-AUTHORSHIP/PREVIOUS

PUBLICATIONS

I hereby declare that this thesis incorporates material that is the result of a research undertaken under the supervision of professors Derek O. Northwood and Xueyuan Nie. In all cases, the key ideas, primary contributions, experimental designs, data analysis and interpretation, were performed by the author, and the contributions of the co-authors was in the capacity of supervision of the research in the form of technical advice and suggestions.

I am aware of the University of Windsor Senate Policy and Authorship and I certify that I have properly acknowledged the contribution of other researchers to my thesis, and have obtained written permission from each of the co-authors to include the above materials in my thesis.

I certify that, with the above qualification, this thesis, and the research to which it refers, is the product of my own work.

This thesis includes material from 3 original papers that have been previously published in peer reviewed journals, as follows:

1. Hussein R.O., Nie X., Northwood D.O., Yerokhin A. and Matthews A. Spectroscopic study of electrolytic plasma and discharging behavior during the plasma electrolytic oxidation (PEO) process. Journal of Physics D: Applied Physics, 43 (2010) 105203(13pp).

2. Hussein R.O., Nie X. and Northwood D.O. Coating growth behavior during the plasma electrolytic oxidation process. The Journal of Vacuum Science and Technology A, 28 (2010) 766-773.

3. Hussein R.O., Nie X., Northwood D.O. Influence of process parameters on electrolytic plasma discharging behavior and aluminum oxide coating microstructure. Surface & Coatings Technology, (2010), doi:10.1016/j.surfcoat.2010.08.059.

I certify that I have obtained permission from the copyright owners to include the above published materials in my thesis. I certify that the above material describes work completed during my registration as a graduate student at the University of Windsor.

I certify that, to the best of my knowledge, my thesis does not infringe upon anyone's copyright nor violate any proprietary rights and that any ideas, techniques, quotations, or any other material from the work of other people included in my thesis, published or otherwise, are fully acknowledged in accordance with the standard referencing practices. Furthermore, to the extent that I have included copyrighted material that surpasses the bounds of fair dealing within the meaning of the Canada Copyright Act, I certify that I have obtained a written permission from the copyright owner(s) to include such material(s) in my thesis.

I declare that this is a true copy of my thesis, including any final revisions, as approved by my thesis committee and the Graduate Studies office, and that this thesis has not been submitted for a higher degree to any other University or Institution.

Abstract

In this study, aluminum oxide was deposited on a pure aluminum substrate to produce hard ceramic coatings using a Plasma Electrolytic Oxidation (PEO) process. The process utilized DC, unipolar pulsed DC in the frequency range (0.2 KHz – 20 KHz) and bipolar pulsed DC current modes. The effects of process parameters (i.e., electrolyte concentration, current density and treatment time) on the plasma discharge behavior during the PEO treatment were investigated using optical emission spectroscopy (OES) in the visible and near ultraviolet (NUV) band (285 nm – 900 nm). The emission spectra were recorded and plasma temperature profile versus processing time was constructed using the line intensity ratios method. Scanning Electron Microscopy (SEM) with energy dispersive x-ray analysis (EDS) was used to study the coating microstructure. It was found that the plasma discharge behavior significantly influenced the microstructure and the morphology of the oxide coatings. The main effect came from the strongest discharges which were initiated at the interface between the substrate and the coating. Through manipulation of process parameters to control or reduce the strongest discharge, the density and quality of the coating layers could be modified. This work demonstrated that by adjusting the ratio of the positive to negative pulse currents as well as their timing in order to eliminate the strongest discharges, the quality of the coatings was considerably improved.

To My Lovely Family

ACKNOWLEDGEMNTS

TABLE OF CONTENTS

List of Tables

List of Figures

Chapter 3 Experiment and Analysis

Chapter 4 Experimental Results and Discussion I:

Chapter 5 Discharge model

Chapter 6 Experimental Results and Discussion III: Effect of process parameters on properties of the coatings

Chapter 1: Introduction

1.1 Motivation for this study

Currently, there is a push in the automotive industry to further reduce vehicle weight. Global trends force the automotive industry to manufacture lighter, more environmentally friendly, safer and less expensive cars [1]. The leading automakers are concentrating on the reduction of car weight and limiting the amount of exhaust emissions due to legislative and consumer, requirements for safer, cleaner vehicles [2]. As CO_2 emission is in direct proportion to fuel consumption car weight has become the most critical criterion of design efficiency assessments [3]. Weight reduction not only saves energy but it also reduces greenhouse gas emissions. Environmental conservation is one of the principal reasons for the focus of attention on Al and its alloys. Environment conservation depends, to a great extent, on transportation industry, particularly CO_2 emissions produced by transport vehicles. European and North American car producers have planned to reduce fuel consumption by 25%, thereby achieving a 30% CO_2 emission reduction by the year 2010 [4,5].

Several surface modification and coating techniques have been developed to enhance the hardness, wear and corrosion resistance of Al alloys. These techniques have included thermal spraying [6], physical vapor deposition (PVD), chemical vapor deposition (CVD) [7-9], ion implantation [10] and sol-gel coating [11]. Plasma Electrolyte Oxidation (PEO) is considered as the most cost-effective and environmentally friendly way to improve the corrosion and wear resistance of light elements [12]. The PEO method can be used to form thick, hard, and highly adherent ceramic-like coatings on the surface of Al alloys as well as the valve metals and their alloys. The oxide layers produced on aluminum alloys can be subdivided in two-sub layers [13-14]: a porous outer layer and a compact internal layer. Several previous studies have investigated the formation mechanisms, and superior tribological properties of PEO coatings produced on different Al alloy substrates [13-16]. As a consequence, the surface properties obtained after PEO treatments are considered promising for industrial application. PEO coatings have been developed for a wide range

of industrial applications including the textile, gas and oil, automotive, electronics, biomedical, aerospace and metal forming industries [17-19].

Recently, several studies have been conducted to better understand the nature of the discharge phenomena and their effect on the mechanisms of coating formation [20,21]. Plasma optical emission spectroscopy (OES) methods have been used to characterize PEO plasmas in terms of electron concentration, ionization temperature, and element-specific ion-to-atom composition [22-23], and their relationships with the layer formation mechanisms. Such parameters are important for better understanding and exploring electrolytic plasmas, a necessary requirement for further development of PEO and associated processes [24]. Based on the OES results, and with an assumption of local thermodynamic equilibrium (LTE) [25], plasma electron temperatures have been calculated using the relative intensities of spectral lines of the same atomic or ionic species [25].

The PEO technology mainly forms an autogeneous oxide coating on the Al-alloy surface and theoretically does not consume the solute. Therefore, the PEO technology is a "clean" treatment because it neither consumes the cathode nor elements in the electrolyte. The PEO process mainly forms an Al_2O_3 coating which is metallurgically bonded to the substrate and has high hardness, high impedance, and high stability and provides Al-alloy with good seawater and high temperature corrosion resistance.

1.2 Objective of the study.

The objectives of this study were to:

   I.   Deposit corrosion and wear resistant protective coatings on commericial purity aluminum (1100 alloy).

   II.   Use an optical emission spectroscopy (OES) method to characterize plasmas in terms of their electron density, ionization temperature, and elemental composition, and their relationships with the layer formation mechanisms.

III. Interpret the emission spectra and plasma temperature profile using a newly-developed discharge model, and relate the discharge behavior to the coating surface morphology and cross-sectional structure.

IV. Analyze the effect of process parameters on the characteristics and properties of the coatings produced using different current modes and different frequencies.

V. Improve the corrosion resistance of the Al alloy.

The optical characteristics of individual discharging events have been addressed by Dunleavy [20]. The collective behavior of the plasma discharge over the entire surface, rather than the individual discharges, will be addressed in this thesis. Various current regimes for example DC, AC and bipolar AC modes, can be utilized in the PEO treatment [26,27]. For the bipolar mode, which has positive and negative charging parts, each part affects the temperature profile. Scanning Electron Microscopy (SEM) with energy dispersive x-ray analysis (EDS) was used to study the coating cross-section and morphologies. The relationship of plasma discharge behavior to surface and cross sectional morphologies of the coating are discussed in detail.

1.3 Organization of the thesis

This thesis is divided into eight main chapters. Following an introduction in Chapter 1, a literature review on the PEO coating process, and OES study are given in Chapter 2. Chapter 3 describes the materials and experimental details. Chapter 4 presents the results of plasma parameters using OES method. The voltage behavior, surface morphology of the coating and a suggested discharge model are described in Chapter 5. Chapter 6 reports on the results of DC, unipolar and bipolar current modes PEO treatment on Al 1100 alloy, respectively. In this chapter the effect of the process parameters including electrolyte concentration (4g/l and 8g/l Na_2SiO_3), current density (0.06, 0.1 and 0.15 A/cm^2), treatment time and pulse frequency, on the coating characteristics of the PEO coatings are systematically examined. The effect of the current mode on the corrosion properties (in 3.5 wt.% NaCl solution) were also determined. Chapter 7 summaries the results from present study and offer some suggestions for future work.

CHAPTER 2 LITERATURE REVIEW

Some interesting historical comments on the Plasma Electrolytic Oxidation (PEO) process can be found in a review by Yerokhin et al [12]. In the mid-1970's, an advanced anodizing process was developed by two Russian scientists, G.A. Markov and G.V. Markova [28-29]. They investigated the wear resistant properties of coatings for light metals. The technology later came to be known as 'micro-arc-oxidation' (MAO) process [30] .In the 1980's, Russian researchers, Snezhko [31-36], Markov [37-39], Fyedorov [40], Gordienko and coworkers [41-42], attempted to apply the new 'micro-arc' oxidation process on various metals. In Germany, Kurze and coworkers [43-45] published the early industrial applications of the MAO. In the past few years, researchers in many countries have also been involved in this field including those from the UK [46-48], China [49], USA [50], and India [51]. Owing to the relatively little information on the process mechanisms and phenomenology, different terminologies have been used in most of the above studies, including anodic spark oxidation [52], micro-plasma oxidation [53], or spark anodizing [54], and plasma electrolytic oxidation (PEO) [19]. In this thesis, the term PEO is used for this process.

Plasma electrolytic oxidation (PEO) is an advanced high-voltage anodizing process consisting of plasma-assisted electrochemical conversion of a metal surface to oxide coatings. The process involves anode electrochemical dissolution, the combination of metal ions with anions to form ceramic compounds, and sintering on the substrate under the action of the sparks. The PEO method is known to involve a large number of short-lived sparks (electrical discharges), caused by localized electrical breakdown of the growing coatings. Micro discharge characteristics determine the thermal and chemical conditions on the oxidizing surface, and play an important role in the formation of phases, structure and stress state of the coatings.

Plasma Electrolyte Oxidation (PEO) is considered as one of the most cost-effective and environmentally friendly ways to improve the corrosion and wear resistance of aluminum and aluminum alloys [55], which makes the process promising for several

industrial applications. The PEO method can be used to form a thick, hard and adherent ceramic-like coating on the surface of Al alloys as well as the valve metals (Mg and Ti) and their alloys [12]: the terminology "valve" metal was coined because on anodization in suitable electrolytes, metals such as aluminum, niobium, tantalum, zirconium and hafnium form thick insulating oxides with rectifying properties [56]. The anodic voltage used in MAO process is relatively high and the high voltage usually induces intensive gas evolution and sparking phenomena and the surface oxide is sintered into like-ceramic coatings.

Previous work on the characteristic phenomenon during the PEO process, coating formation mechanisms, and coating tribological properties are described in this chapter.

2.1 Plasma Electrolytic Oxidation

Plasma Electrolytic Oxidation (PEO) is a process of plasma assisted electrochemical conversion of a metal surface to produce an oxide ceramic layer [12]. PEO operates in a similar configuration to a conventional anodic oxidation but at a much higher applied voltage (400-600 V). Due to a plasma discharge at the metal-electrolyte interface in PEO, the bi-phase electrode/electrolyte interface structure normally encountered during conventional anodizing is transformed into a three-phase electrode/gas (plasma)/electrolyte one [57]. In the plasma discharge region, plasma chemical interactions occur which affect the formation of the coating [12, 57].

The nature of the anodizing process is based upon the electrochemical principle that when a current is passed through an electrolyte in which an aluminum anode is employed, the anion migrates to the anode [58]. The anion is then discharged and ionized, where in an aqueous solution; the anion consists in part of oxygen, which is adsorbed by the aluminum surface via a chemisorption process. As adsorption proceeds, the surface is reconstructed, forming an adjoining oxide as Al_2O_3, which is slightly soluble in the electrolyte, and pores are thus formed in the film allowing continuous access of current via the electrolyte to the metal. During the PEO process a variety of plasma discharges occur at the metal-electrolyte interface. The microdischarges enhance

heating and diffusion processes and plasma thermo-chemical reactions at the electrode surface and thus play an important role in the phase formation and structure of the ceramic layer. Thus, an understanding of the discharge properties is very helpful in revealing the mechanisms of the PEO process.

2.1.1 The PEO equipment

The equipment used for PEO treatment of Al-alloys is relatively similar to that of conventional electroplating except for the need of higher voltage power supply (300-1000V). Typically the PEO unit consists of an electrolyser and a high power voltage supply. The electrolyser is usually a water-cooled bath placed on a dielectric base and fixed in a grounded steel frame, which has an insulated current supply and a window to observe the process in operation. A stainless steel plate in the bath serves as the counter-electrode. In some cases the electrolyser incorporates electrolyte mixing, recycling, and gas exhaust facilities, as well as electrical interlocks for safety purposes.

Various types of power source can be used for the PEO process including DC, unbalanced AC or pulsed DC. Alkaline electrolytes are usually used, containing silicates, polyphosphates, or aluminates to promote strong metal passivation due to formation of near-surface gels or insoluble compounds.

2.2 Current-Voltage characteristics

Electrical plasma process and the current-voltage characteristics during the PEO process were overviewed by Yerokhin et. al. [12], and the two kinds of current-voltage characteristic diagram are shown in Figure 2.1. Firstly, a conventional anodic oxidation of the substrate surface (anode) occurs with the current-voltage characteristics conforming to Ohm's law, corresponding to the region '0-U_1' in type-a system and '0-U_4' in type-b system.

For a type-a system in the region U_1-U_2, an increase in voltage causes a current oscillation accompanied by luminescence. The current increase is limited by a fractional shielding action of gaseous reaction products (O_2 or H_2) surrounding the electrode

surface. However, the increased current in the other parts of the electrodes causes local boiling of the electrolyte close to the electrode. With the further voltage increases reaching U_2 value, the electrode is totally covered by a continuous gaseous vapor envelope of low electrical conductivity. The electric field strength within the envelope then reaches a high enough value (10^6-10^8 V/m) to cause the ionization process in the region. A rapid sparking in the scattered gaseous bubbles is observed as the result of ionization processes, followed by a uniform glow distributed throughout the vapor plasma envelope. Beyond a critical voltage U_3, the glow discharge transforms into severe arcing accompanied by a characteristic low-frequency acoustic emission.

With regard to the type b system, the process is more complicated. Initially, at point U_4, which in practice corresponds to the corrosion potential of the material, the passive film that resulted from the anodic oxidation begins to dissolve. Then, in the region of re-passivation, U_4 to U_5, a porous oxide film grows, across which most of the voltage drop now occurs. At point U_5, the electric field strength in the oxide film reaches a critical value beyond which the film is broken through due to impact or tunneling ionization. In this case, small luminescent sparks are observed to move rapidly across the surface of the oxide film. At point U_6, the beginning of thermal ionization processes causes slower, large arc discharges. In the region U_6 to U_7, thermal ionization is partially blocked by negative charge build-up in the bulk thickening oxide film. Above the U_7, the arc micro discharge occurring throughout the film penetrate through to the substrate and transform into powerful arcs, which may cause destructive effects including thermal cracking of the film.
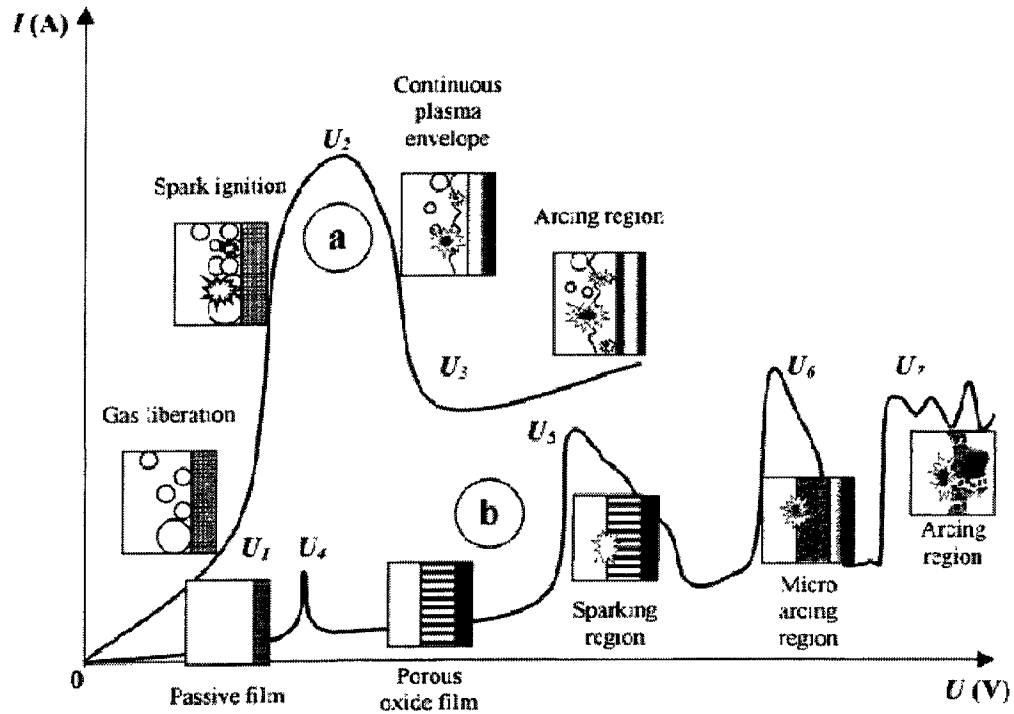
Figure 2.1 Two kinds of current–voltage diagram for the processes of plasma electrolysis: discharge phenomena are developed (a) in the near-electrode area and (b) in the dielectric film on the electrode surface [12].

The evolution of the microdischarge over the PEO process duration of an Al alloy has been studied using real imaging techniques (digital video recording) [23]. The apparent sizes of discharges, as well as discharge nature at different PEO stages of Al alloys were also considered [21,59]. Matykina et al, [60] investigated the discharge behaviour on Ti using video imaging with 10 ms exposure period. Video images show that microdischarges move randomly all around the sample surface. With increase in PEO processing time, both discharge size and color also change as shown in Figure 2.2. The evolution of the micro-discharge aspect as a function of the treatment time is depicted in Figure 2.2 that corresponds to side view pictures of the sample during PEO processing of an aluminum alloy. At the early stage of the process, the growing oxide film breaks down due to an increase in the applied voltage. Intense gas evolution along with some luminescence at the surface is easily observed, this is followed by sparks

flashing randomly all over the aluminum alloy surface (Figure 2.2a), while sparks progressively change to micro-arcs (Figure 2.2c). Finally arcs regime, Figure 2d,e occurring at later stages of the process causing irreversible damages to the oxide layer. However the effect of the entire discharge events occurring on the whole sample surface during the entire PEO process had not been studied and an investigation into the collective behavior of plasma discharges is therefore needed.
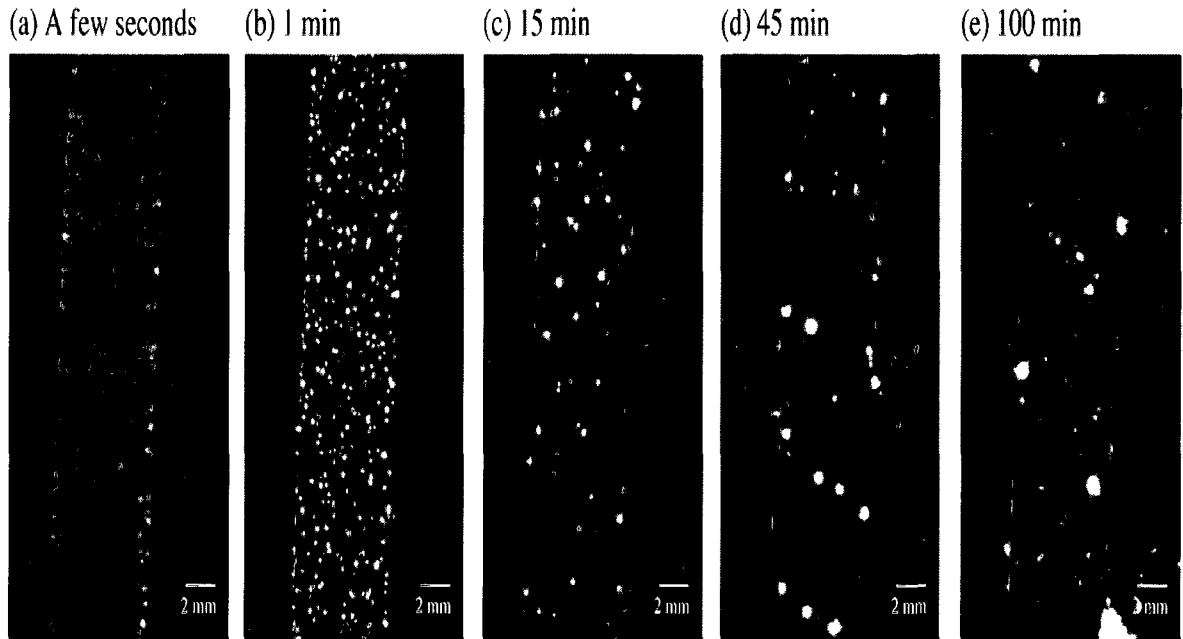
Figure 2.2 Side-view pictures of aluminum alloy samples at different times of the PEO process (R=1.57). The integration time of the camera is set between 8 and 10 ms [23].

2.3 Plasma discharge models

An important consequence of the occurrence of surface discharges is the development of metallurgical processes in the growing of oxide layer, which are induced by the heat liberated in discharge channels from electron avalanches. This instantaneous local heating leads to melting, quenching and recrystallization of the substances deposited onto the surface. The direction and intensity of the deposition processes depend on the density and power of discharges which are a function of the coated thickness. Several microdischarge formation models have been proposed [61-66]. According to Yerokhin et

al [21] there are three different mechanisms of discharge formation in PEO process as shown in Figure 2.3. The first model [61-63], defined the microdischarges appearance as a result of oxide film dielectric breakdown in a strong electric field (Figure 2.3(a)). The breakdown is treated as "streamer propagation" due to the electron avalanche effects induced by film dopants and structure defects. Three main steps can be discerned in the breakdown process. In the first step, the discharge channel is formed in the oxide layer as a result of its dielectric stability in a region of raised conductivity. This region is heated by generated electron avalanches up to temperature of 10^4 K. Due to the strong electric field ($\sim 10^6$ V/m), the anionic components of the electrolyte are drawn into channel. At the same time, owing to the high temperature, aluminum and alloying elements are melted out of the substrate and enter the channel. Thus a plasma column (plasmoid) is formed as a result of these processes. In the second step, plasma chemical reactions take place in the channel, which leads to an increase in pressure inside the channel. So the plasmoid expands to balance it. Concurrently, separation of oppositely charged ions occurs in the channel due to the presence of the electric field. The cations are ejected from the channel into the electrolyte by electrostatic forces. In the last step, the discharge channel is cooled and the reaction products are deposited on to its wall.

The second group of models [64-65] considers each discharge as a gas discharge occurring in micropores of the oxide film, Figure 2.3(b). The formation of a gas phase in the pore (and discharge ignition in it) is believed to be induced by an initial dielectric breakdown of a barrier layer in the bottom of the micropore. An alternative model of microdischarge formation was proposed based on analogy with contact glow discharge electrolysis [66], Figure 2.3(c). In this process, a glow discharge is observed at the interface of the electrolyte and a thin vapor sheath is formed at the surface of a platinum wire anode at $U^+ \geq 420$V. In the case of an aluminum anode, however, the gas bubbles accompanying the oxidation process and the discharge play the role of the vapor sheath:, therefore, it seems as if it is disintegrated into a number of microdischarges. Nevertheless, it is important to recognize that the common condition of discharge initiation in both cases appears to be electron emission from the electrolyte surface (partial cathode) into a gaseous phase, rather than dielectric breakdown of the growing oxide film. It should also be noted that free electrons might appear initially at the oxide–

electrolyte interface in strong electric fields, regardless of the presence of any gas/vapor phase, due to the ionization of anions and molecules of water. The free electrons would then immediately participate in a series of reactions with water, resulting in the formation of gaseous products (H_2 and O_2), thus providing the necessary conditions for maintenance of a stable plasma discharge environment.
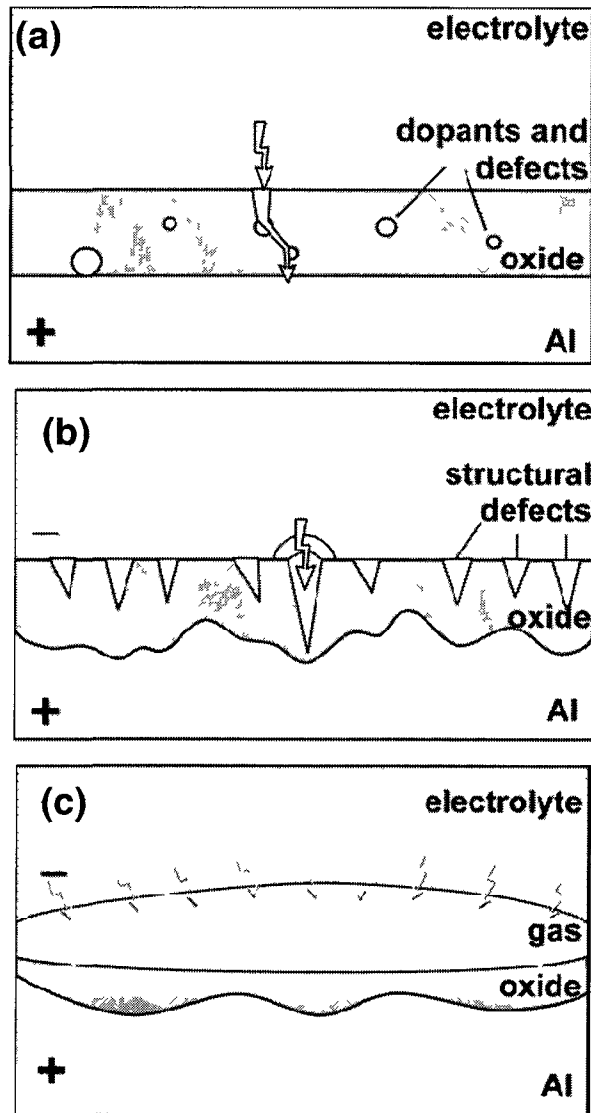
Figure 2.3 Schematic illustration of models describing the appearance of surface discharge during anodic oxidation of Al: (a) model of the oxide film dielectric breakdown; (b) discharge-in-pore model and (c) model of contact glow discharge electrolysis adapted for the presence of an oxide film on the metal surface [21].

Yerokhin et al [21] found that the above models do not fit the spatial, temporal and electrical characteristics of microdischarge phenomena, which were observed in their investigation. A new model was suggested based on the analogy with contact glow discharge electrolysis. The model assumes the possibility of free electron generation and glow discharge ignition in the gaseous media at the oxide-electrolyte interface, which leads to heating, melting and quenching of the underlying oxide layer. The estimated ranges of the microdischarge current density and duration time sufficient for initiating phase transitions in the surface oxide layer are in good consistence with the experimental data.

2.4 Mechanisms of coating formation in PEO process

Prior to a discussion of the PEO coating mechanism, it is important to clarify that the proposed coating mechanism should explain the following features observed experimentally [67], namely:

a. A linear coating deposition rate (Figure 2.4).

b. A linear increase in surface roughness of the PEO coating with increasing time of the coating or equivalently with increasing coating thickness (Figure 2.5).

d. The increase in peak microhardness value (near the interface) with increasing coating thickness (Figure 2.6).
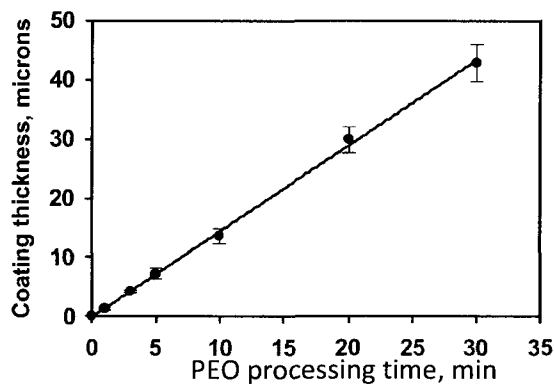
Figure 2.4 Influence of PEO treatment time on coating kinetics [67].
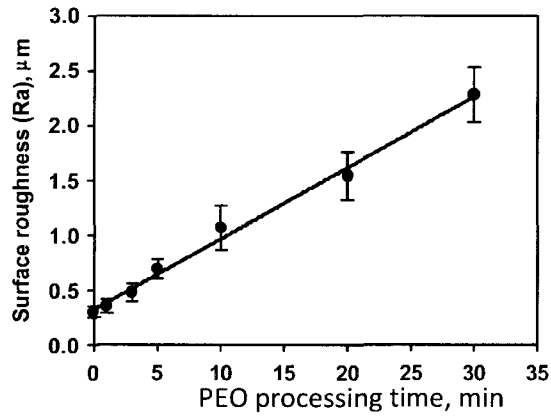
Figure 2.5 Influence of PEO treatment time on surface roughness of the coatings [67].
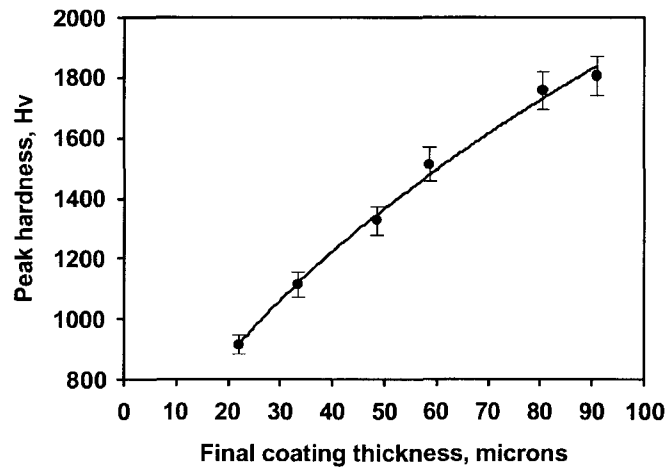
Figure 2.6 Variation in microhardness of PEO coating as a function of the distance from the interface [67].

Based on the literature there is a competition between two mechanisms

I- Growth of plate layer onto the surface

II- Growth of compact layer at film/substrate interface by diffusion or transport of oxygen

2.4.1 Growth of plate layer onto the surface

The growth mechanism of ceramic layers (layer growth) (Figure 2.7) results from molten aluminum which is oxidized when flowing out through the discharge channels that are created due to the oxide layer breakdown. By this way, alumina is formed which contributes to the layer when being ejected from the channels and rapidly cooled at the surface–electrolyte interface (pancake and plate layer formation). From a comparison between Figures. 2.8 and 2.9, it appears that the mechanism proposed in Refs. [67,68] for the pancake formation also holds for the formation of the outer layer constituted by plates and pores.
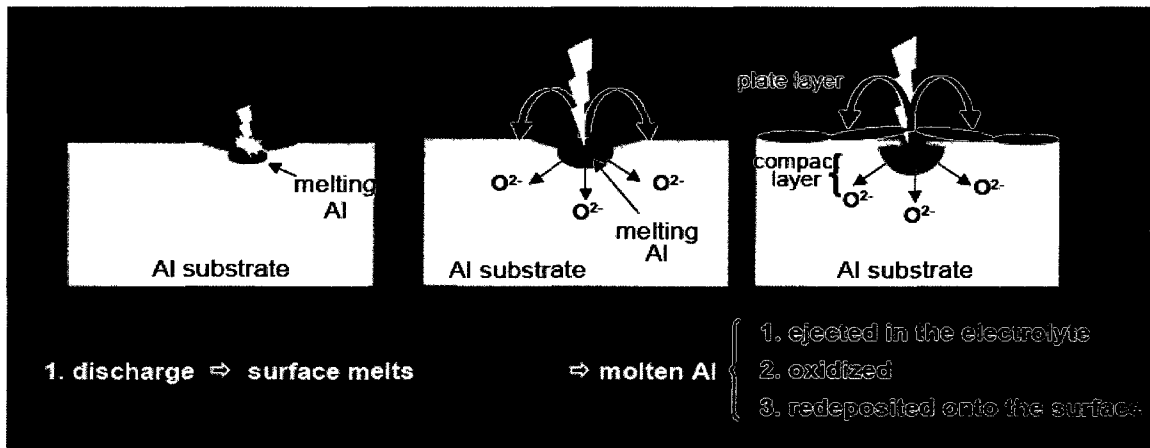
Figure 2.7 Plate layer growth mechanisms

In the PEO process, the observed linear deposition kinetics can be simply related to Faraday's laws of electrolysis. However, the SEM micrographs shown in Figures 2.8 and 2.9 clearly indicate that the coating deposition occurs via the discharge channels which at any time during the coating process connect the coating–substrate interface all the way with the coating top surface which is in close contact with the electrolyte. It is also clear, as indicated by the visual observation of continuous movement of the sparks on the coating surface and also by SEM micrographs, that the discharge channels have a finite life. Thus, the discharge channels are continuously formed and closed throughout the coating process.
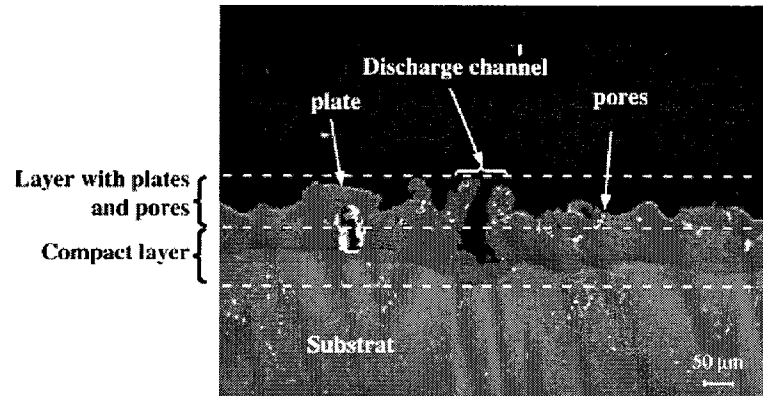
Figure 2.8 SEM micrograph cross-section after a 140 min PEO treatment (R=1.57).
Description of the different sub-layers [59].
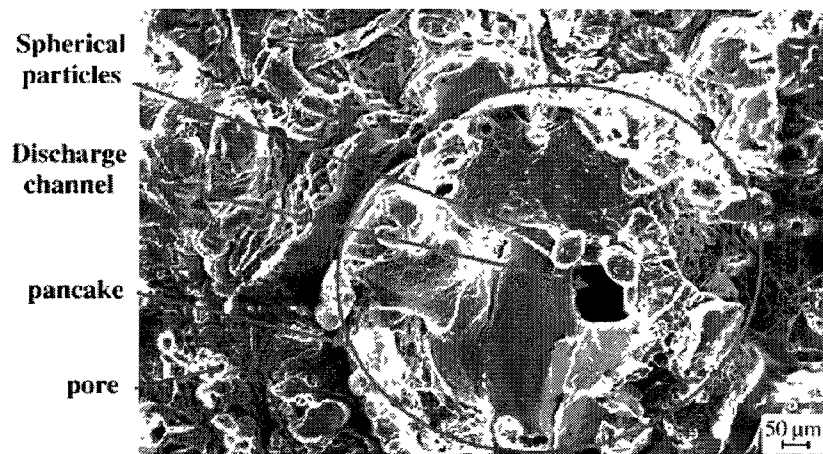
Figure 2.9 SEM micrograph of the top surface after a 140 min PEO treatment [59].

Most of the PEO experiments indicate that the coating thickness increases linearly with coating time and this in turn implies a constant volume rate of coating deposition since coating area is a constant.

The pancake diameter and thickness (of the order of channel diameter) increases with increasing coating time [69]. Since the coating is formed with pancakes as the basic building unit, it should be obvious that the surface roughness of the coating should be of the order of channel diameter as well. Thus, the linear increase in coating roughness is

directly related to the fact that the discharge channel diameter also increases linearly with coating time. The rapid solidification of aluminum promotes the formation of meta-stable γ-Al_2O_3 phase [54]. Since the surface layers of the PEO coatings are always in contact with the surrounding low temperature electrolyte medium, the surface layers contain γ-Al_2O_3 phase. According to this explanation, the phase contents of the surface layers should comprise predominantly γ-phase irrespective of the coating thickness. The identical XRD patterns with predominantly γ-phase obtained for the coatings wherein the X-ray penetration is totally within the coating. However, the low thermal conductivity of aluminum, causes the underlying layers of the coatings to remain hotter (since the heat generated from the channel cannot be easily dissipated) and the temperature is sufficiently high to cause the transformation of originally formed γ to α-Al_2O_3 which is around 1050 °C to 950 °C [70]. Thus, it is expected that the proportion of α-Al_2O_3 will continuously increase towards the coating– substrate interface. Such a phase gradient is responsible for the observed microhardness variation across the coating thickness with peak (maximum) hardness close to the interface since α-Al_2O_3 is harder than γ-Al_2O_3. During the progress of PEO coating deposition, the new discharge channels that are formed heals the pores and cracks formed earlier resulting in the dense inner portion of the coatings free from cracks [71].

2.4.2 Growth regularity of ceramic coatings

Xue et al [14] presented an alternative model describing the growth mechanism of the ceramic coating layer. Figure 2.10 shows a schematic drawing of the sample geometrical dimension change after PEO. Parts a and b refer to the partial coatings growing towards the coating surface and Al substrate respectively. The dashed line in Figure 2.10 represents the position of the original surface of the sample before the treatment. The coating thicknesses with different oxidation durations were determined by Xue et al [14] using an eddy current thickness meter. Meanwhile, the dimensions of the aluminum alloy disc before and after oxidation were measured by a spiral micrometer, from which the a and b values at different oxidation durations were calculated. The variation of the coating thickness as a function of oxidation time is given in Figure 2.11.

It shows that the total thickness of coatings gradually increases with increasing oxidation time (curve h). A linear section appears during the first few hours, but after 5 h, the growth rate decreases rapidly, and finally it becomes zero. Xue et al [14] reported that a coating with a thickness of 230 mm was obtained.
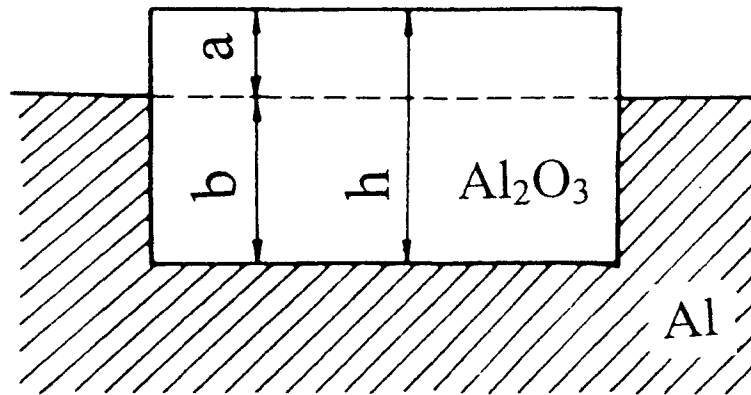
Figure 2.10 Schematic drawing of the change in sample dimension in the process of microarc oxidation. h and a are the coating thickness and the increase of the sample dimensions, respectively [14].

As shown in curves a and b of Figure 2.11, in the first 2 h of PEO, the ceramic coating grows mainly towards the surface. However, after 2 h, the change in curve a is smaller, namely, the sample dimension no longer increases and even decreases to some extent. The cause of the dimensional decrease is that the partial coating in the surface layer is dissolved into the aqueous solution while the Al substrate is oxidized. When the growth of coatings towards the surface is lower than the dissolution, the geometrical dimension of the coating would decrease. After oxidation of 2 h, curve b rapidly rises. The oxidizing rate towards the Al substrate determines the growth rate to a total coating thickness h. Furthermore, curve b appears to be linear after oxidation for 5 h.
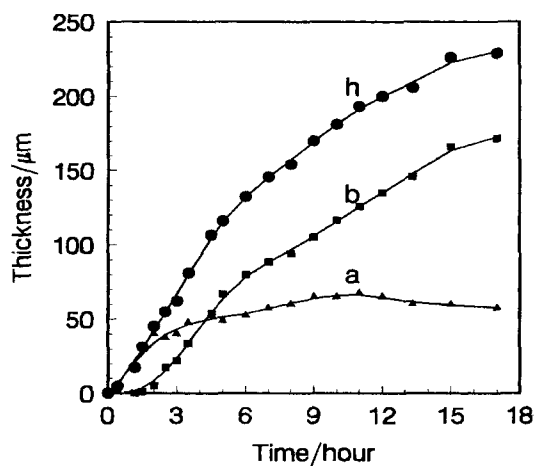
Figure 2.11 The growth curve of thickness h, a and b in the process of microarc oxidation of AL 2024 alloy [14].

2.4.3 Growth of compact layer at metal-oxide interface by diffusion or transport of oxygen

As described previously, countless sparks moving rapidly on the surface of the sample can be observed when the anodic potential is increased up to several hundred volts. In fact, the instantaneous temperature in the spark or microarc zone is high enough to cause Al_2O_3 and Al to melt. The surface of a PEO coating is porous as shown in Figure 2.9 and bubbles at the bottom of holes are preferentially broken down to discharge, forming discharge channels in the coating. The partial molten alumina is erupted into solution along many small discharge channels and a surface loose layer with high porosity is formed.

As shown in the schematic diagram of Figure 2.12, during anodic oxidation of aluminum, the aluminum cations transfer towards the coating surface while oxygen anions transfer towards the Al substrate. However, the transfer of oxygen anions is rather slow when an anodic oxide film grows up to a certain thickness. Nevertheless, for the PEO process, both thermal diffusion and electric transfer of ions have an important influence upon coating growth, which are different from anodic oxidation. The instantaneous high temperature and high pressure in the microarc zone greatly enhance inter diffusion between the oxygen anions and aluminum cations in the coating near the

discharge zones. Furthermore, while plasma discharges occur in the coating, oxygen can be directly delivered into the internal layer of the coating through these discharge channels. However, oxygen anions are enhanced to transfer towards the Al substrate due to a higher electric field intensity of 10^6 V/cm in the coating. Therefore, in the PEO process, after the loose layer with certain thickness has been formed, oxygen diffusion to the Al substrate plays a leading role in the coating growth, and the growth rate of the PEO process coating is controlled by the rate of transferring oxygen towards the Al substrate as shown in Figure 2.12.
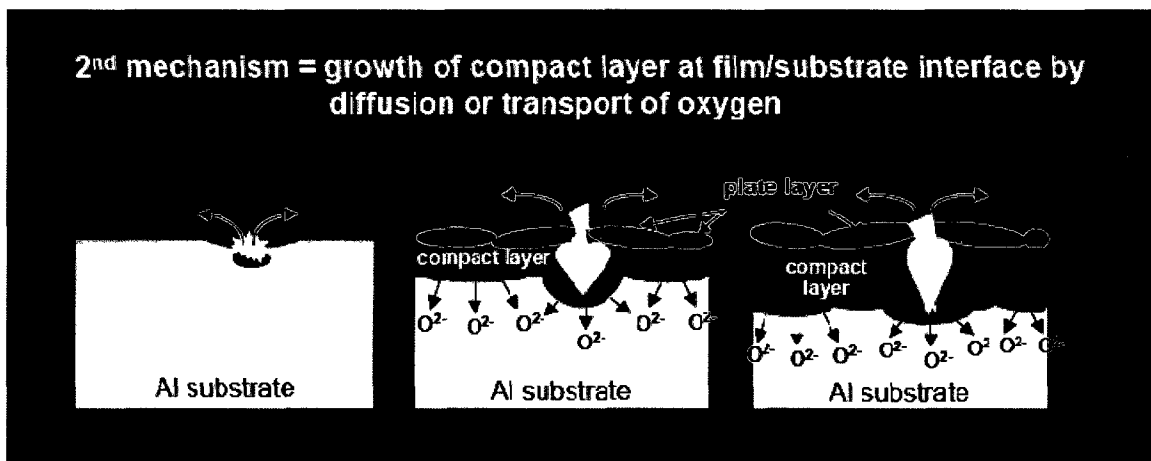
Figure 2.12 Compact layer growth mechanisms

According to Xue et al [14], SEM micrographs of cross-sections of the Al samples shows that the ceramic coating contains two layers: a loose layer and a compact layer, and the compact layer is about 3 time's thicker than the loose layer. This observation indicates that the interface between the compact layer and the loose layer was certainly located near the sample's original surface. Therefore, the part of the coating growing towards the external surface in relation to the sample's original surface is mainly a loose layer, but that growing towards the Al substrate is mainly a compact layer. Hence, for a thicker PEO ceramic coating formed on an aluminum alloy, if its loose surface layer is ground away, a wear-resistant compact layer is left, and the sample roughly maintains its original size before the oxidation.

With the aim of determining the influence of current frequency on the PEO surface layer, Tillous et al [72] investigated the oxidation of pure aluminum at two current frequencies (100 Hz and 950 Hz) but with the same treatment time (50 min). Figure 2.13(a and b) shows SEM micrographs of PEO surface layers obtained at 100 Hz and 950 Hz, respectively. SEM observation revealed that the PEO layer formed at 100 Hz is thicker (75 ± 5 µm) than the one obtained at 950 Hz (50 ± 5 µm). SEM micrographs of fracture cross-sections revealed high percentage of the so-called "dendrite" defects for the entire inner layer. This defect consists of a central channel, which is surrounded by fine piled-up platelets. The geometry of this defect indicated local fusion of alumina leading to standard dendrite solidification under discharge formation inside the coating. Many larger "dendrite" defects were formed in the coating at 100 Hz compared to 950 Hz. Consequently, it was concluded that the coating obtained at 100 Hz should be more porous than that obtained at 950 Hz.
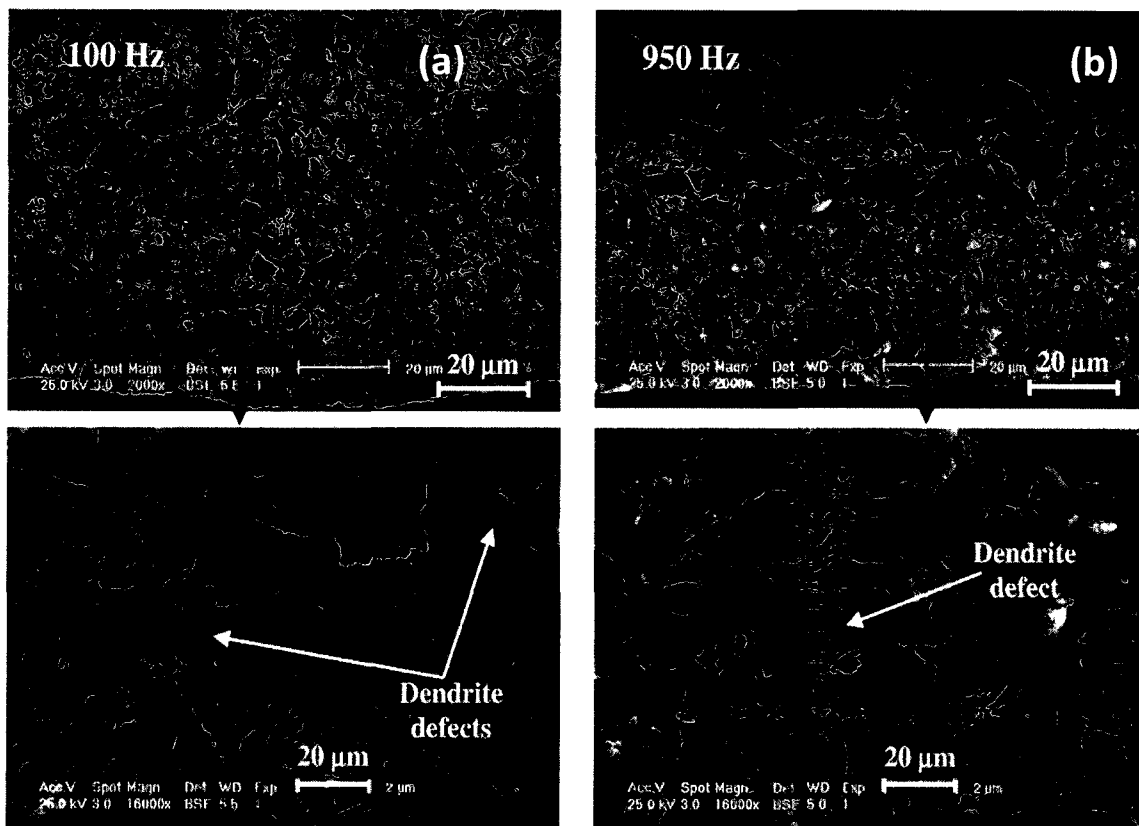
Figure 2.13 SEM micrograph fracture cross-sections of MAO layers formed on aluminum at (a) 100 Hz and (b) 950 Hz [72].

2.5 Growth mechanisms

Mécuson et al [23] investigated the PEO processing of aluminum alloys for different shapes of the applied current waveform. The variations of the average total layer thickness with the process time for two different R (positive to negative charge quantity ratio) are shown in Figure 2.14 It can be seen that for a short treatment time (40 min) the growth kinetics are the same for the two processes, exhibiting the linear kinetics commonly observed in PEO treatments [67,68].
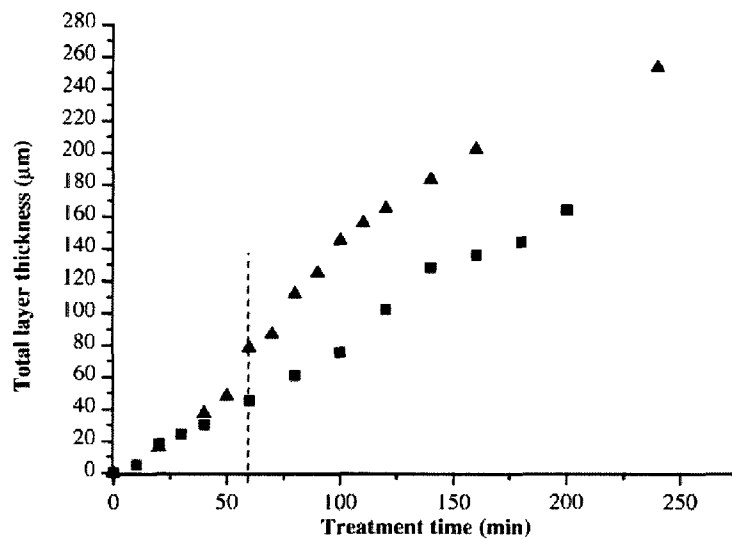
Figure 2.14 Dependence of the average total layer thickness on the PEO treatment time. R=1.57 (squares) and R=0.89 (triangles) [23].

The same slopes that were observed for short treatment times (40 min) can be explained by the same positive current density being used in the two processes. For treatment times higher than 40 min the layer thickness evolution depends on the positive to negative charge quantity ratio R. In the process with high R value (R=1.57), the growth kinetics exhibits the "regular" behavior that can still be described as linear. On the other hand, when the negative charge quantity is set greater than the positive one (R=0.89), the growth kinetics exhibits two different regimes as shown in Figure 2.14. The growth kinetics shows a linear to parabolic transition between 50 and 70 min. This kinetics transition is related to the switching from an arc to a soft regime (reduction of strong

discharges). As a matter of fact, arcs contribute to the growth of the layer as described earlier, but they also destroy the layer that is being formed. Therefore, the growth of the oxide layer results from a competition between these two phenomena.

2.6 Plasma spectroscopy

Plasma spectroscopy is considered as one of the best available diagnostic techniques, used in plasma processing to measure the electron number density, the ion and electron energy distribution functions (or kinetic temperature, if Maxwellian) and plasma compositions.

2.6.1 Visible and near ultraviolet (NUV) spectroscopy

In the same way that we use visible light to diagnose the world around us with our eyes and brains as detectors and analyzers, we can use light emitted from plasma as a tool to examine what is going on in the plasma. This is a vital step towards understanding and exploring the plasma and its interactions, a requirement for the continued development of the PEO process. If we are just observing the light emitted then it is a passive technique and our measurements will not disturb or alter the plasma conditions. Most spectrometry is done in the visible part of the spectrum (optical spectrometry), because of the experimental inconvenience and additional expense of working at infrared or ultraviolet wavelengths. Optical spectrometers are relatively inexpensive and widely available commercially. Analysis of observed spectra can therefore provide information on transitions and energy levels providing a useful tool to determine various quantities of the emitting source. With the addition of atomic and molecular physics concepts and models, parameters such as electron temperature and density can be determined making visible spectroscopy a sensitive diagnostic tool for plasmas.

Spectroscopy is an umbrella term covering the experimental observation, investigation and analysis of electromagnetic radiation spectra. By definition then, Visible and near ultraviolet (NUV) spectroscopy is concerned with the observation and analysis of the spectra of radiation with Visible and NUV wavelengths. Visible and NUV light is emitted from plasma due to transitions between energy levels in the atoms, ions

and molecules of the plasma. The wavelength of the radiation is equal to the energy change and hence characteristic of the levels and interactions involved. Optical emission spectroscopy (OES) is the analysis of light that is emitted from a medium in the absence of external optical excitation. Significant levels of such optical emission (OE) are present only in special circumstances. Optical emission is important during plasma-assisted processing, such as plasma-assisted etching and deposition, and sputter deposition processes, where gas-phase species are promoted to excited electronic states by collisions with energetic electrons. These excited states relax to lower states, which may be the ground electronic state, by spontaneous emission. This emitted radiation is then spectrally dispersed and detected. Optical emission from plasma is also called plasma-induced emission (PIE). The emission processes in OES are depicted in Figure 2.15. Figure 2.15 illustrates the emission process. Gaseous plasma species are elevated to excited states by collision with energetic electrons. As a species drops to a lower energy state, an electromagnetic wave is released. Since only excited species can release electromagnetic waves, the observed spectrum reveals density of particles in the excited states, which is only a small fraction of the total particles, on the order of 10^{-4}. Also the spectrum can contain emission from intermediates and products that may overlap with that from the intended diagnostic species. As a result, it is necessary to choose selectively from the spectrum for the wavelength in performing diagnostics. We need to choose the wavelengths that are correlated with the diagnostic parameters.

Neglecting contribution from other emissions, let us consider only the case that a plasma particle is excited from the ground state i to a state j by an electron collision, and then drops back to state i. The electromagnetic emission intensity can be written as [73],

$$I(\lambda_{ij}) = N P_{ij} A_{ij}(\lambda_{ij}) \qquad (2.1)$$

λ_{ij} is the transition wave-length between state i and state j, N is the excited state density, A_{ij} is the Einstein emission probability, and P is the electron impact excitation function which represents the probability of exciting the state j by electron impact, starting from the ground state. P is a complex function of electron temperature T_e, and is given by Lieberman and Lichtenberg [1] as:

$$P = \int_0^\infty 4\pi v_e^2 \, dv_e \sigma_\lambda(v_e) \, v_e f_e(v_e, T_e, n_e) \qquad (2.2)$$

Where v_e is the electron velocity, σ_λ is the cross section for emission of a photon of wave-length λ due to electron impact excitement, and f_e is the electron distribution function which depends on electron temperature and electron density.
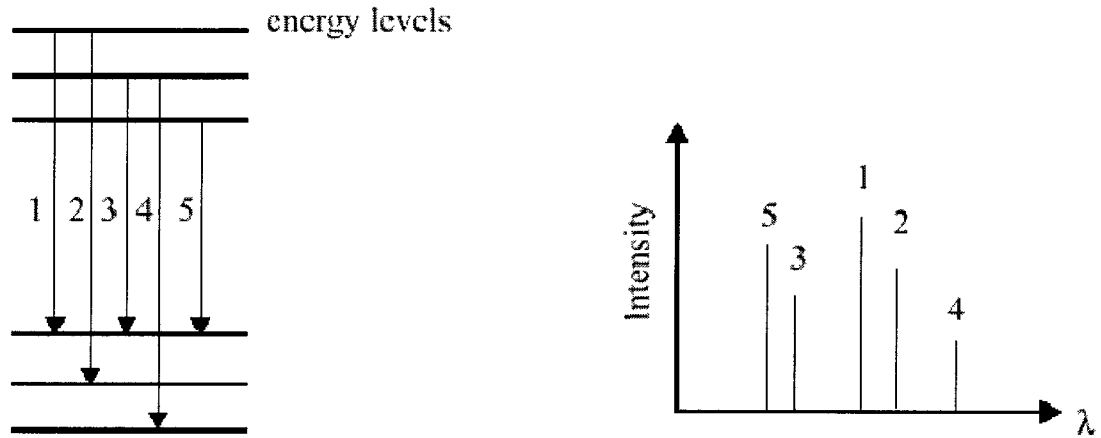
Figure 2.15 Energy levels involved in typical OES experiments.

Optical emission in the plasma chamber is collected by the lens, transmitted through an optical fiber, imaged onto the entrance slit, and dispersed by the diffraction grating system. Then a CCD camera detects the dispersed beam through the exit slit. The diffraction grating is usually a square. The grating equation is:

$$m\lambda = d \left(sin\theta_m - \theta_i\right) \qquad (2.3)$$

where m is the diffraction order, d is the groove separation distance, and θ_m and θ_i are the angles of incidence and diffraction respectively. The grooves are designed to maximize the first-order diffraction (m=1) at a particular wavelength. The wavelength resolution of dispersion can be computed as:

$$\Delta\lambda = \frac{w}{mvf} \, cos\theta_m \qquad (2.4)$$

24

where w is the exit slit width, f is the spectrometer focal length, which is the distance from the exit plane to the last focusing mirror, u is the groove density. The efficiency of a grating system for collecting light is wavelength-dependent, so the detected optical emission intensity by OES is:

$$I(\lambda_{ij}) = NP_{ij}A_{ij}(\lambda_{ij})Q(\lambda_{ij})k \quad (2.5)$$

where $Q(\lambda_{ij})$ is the correction factor accounting for the grating system's collection efficiency at wavelength λ_{ij}.

2.6.2 Atomic and molecular data

The interpretation and analysis of observed spectra requires knowledge of the underlying the atomic and molecular processes leading to the emission of light and of the structure of the emitting atoms, ions and molecules. Extensive measurements and cataloguing of spectral line wavelengths and transition probabilities of atomic ions can be found in many sources, including [74,75]. Although the complete solution for the population of any particular level is very complex, several models have been proposed. The most important models are partial and complete thermodynamic equilibrium model (LTE), the coronal model and collisional radiative model for the region between them [76].

Radiation emitted by plasmas can be divided into two main types (which are classified according to the initial and final states of the electrons). Firstly, there is continuous radiation. This causes a background or continuum in the observed spectrum and is due to bremsstrahlung radiation (arises due to electron-ion collisions with a loss of energy for the electron) with additional contributions from recombination. The second type of radiation emitted from plasma is the characteristic radiation or line radiation arising from the radiative decay of an excited state. This state can have been excited by electron impact or by interaction of the ion with the plasma electrons causing radiative or dielectronic recombination. The wavelengths of the lines are characteristic of the emitting ions providing a useful diagnostic tool.

Optical emission during plasma processing can come from neutral or ionized atoms, radicals, or molecules that have been electronically excited. This type of emission has been critically reviewed by Donnelly[77]. Selwyn [73] has described the practical application of OES for process monitoring during plasma processing, and has detailed the required instrumentation.

Initial observations of light emission during electrolysis of aqueous solutions were made by Sluginov [78], who discriminated between the first and the second order luminosity, termed later as galvanoluminescence and the anode effect, respectively. For Al anodizing, the discharge phenomena were first investigated by Gunterschultze and Betz [79], who pointed to the presence in the optical emission spectra of characteristic lines corresponding to both the metal electrode and the electrolyte species. These basic observations are consistent with the results of more recent studies of optical emission spectroscopy (OES) performed for Al in both acidic [80], and alkaline electrolytes [15,81], Mg [46], Zr and Ti alloys [82-83]. In summary, it has been found that the species from the metal electrode are present in the plasma in atomic or weakly ionised states and that the electrolyte species, both cationic and anionic, are usually decomposed into individual atoms that can also be ionised. The difference between the discharge spectra in acidic and alkaline solutions is mainly in the presence of OH^- radicals in alkaline solutions.

Based on OES data, Kharitonov et al [84], evaluated plasma temperatures in discharges during PEO processing of Al in sulphuric acid and came to the conclusion that the discharge consists of 2 micro-regions, the hot core with temperatures up to 8000 to 10000 K and a relatively cold (2000 K) bubble separating the core from the electrolyte. This temperature range is more than sufficient to directly convert aluminum oxide produced at the early anodizing stages into high-temperature crystalline phases, e.g. corundum, as confirmed by numerous studies of phase composition in PEO coatings [21,73]. Similar model concepts were adopted by Klapkiv et al [85], for interpretation of earlier spectroscopic studies of discharge in PEO of Al in alkaline solutions [22, 86]. Evaluations based on the spectroscopic data gave electron concentration and temperature to be of order of $N_e = (3.2$ to $7) \times 10^{22}$ m^{-3}, and $T_e = 6000$ to 8000 K respectively,

indicating only a partial local equilibrium plasma state in the discharge channel. Very similar plasma characteristics ($N_e = 3 \times 10^{22}$ m^{-3} and $T_e = 6000$ to 10000 K) were reported for the discharge in PEO of Zr in alkaline solutions, for which the intensity ratio of Zr lines appeared to be similar to those in a spark-type discharge [87-88]. Characteristics of individual discharge events were addressed in the recent study by Dunleavy et.al, [20] performed in a mini-cell arrangement. It was shown that the microdischarges tend to occur in cascades of short (10^{-5} to 10^{-4} s) avalanche-like events lasting in total 10^{-3} to 10^{-2} s. The spectroscopic studies confirmed the presence of two distinct regions of plasma; a lower density peripheral region at ~3500 K, and a higher density core at ~16,000±3500 K.

2.7 Some challenges for the production of PEO coatings

Due to superior coating performance, process cost-effectiveness and environmental friendliness, Plasma Electrolytic Oxidation (PEO) is attracting increasing attention for the surface treatment of lightweight metals, in particular Al, to enhance their hardness, wear and corrosion resistance. Thus far, a number of tests have been made using Al alloys to determine the optimal process parameters to give a high growth rate and low energy consumption in order to obtain a desirable combination of the coating morphology and properties. However, further work is required on the following aspects.

- Firstly, several studies have investigated the formation mechanisms and superior tribological properties of PEO coatings produced on different Al alloy substrates. However, further development work is required on process optimization, control and consistency. With increase in PEO processing time, both discharge size and color also change. However the effect of the entire discharge events occurring on the whole sample surface during the entire PEO process has not been yet studied. Investigation into the collective behavior of plasma discharges is therefore needed. In this regard, basic work is needed to better understand the nature of the discharge phenomena and their effect on the mechanisms of coating formation.
- Secondly, given the liquid environment, plasma spectroscopy methods are the best techniques available to characterize such plasmas in terms of electron

concentration, ionization temperature, and element-specific ion-to-atom composition, and their relationships with the layer formation mechanisms. However, despite abundant coating characterization and testing research, fundamental studies on the effects of process parameters on the characteristics of light emission from plasma discharge during PEO are still in their infancy. This is important for better understanding and exploring electrolytic plasmas, a necessary requirement for further development of PEO and associated processes.

- Finally, coating surface morphology and structure are affected by many parameters such as electrolyte compositions, substrate materials, and the electrical parameters mainly current mode and current density. With the aim of improving the characteristics of the ceramic coatings, many attempts have been attempted to improve the supplied current regimes, suggesting different form and durations of current pulses. Different current modes have been utilized in the PEO treatment including, DC, AC, unipolar and bipolar current modes. The properties of the plasma discharges themselves in the bipolar current mode differ from those of the discharges obtained in the unipolar current mode. From the plasma discharge point of view, significant reduction of strong discharges can reduce the detrimental effects associated with such discharge events

Chapter 3 Experimental Details and Analytical Techniques

In this chapter, the experimental procedures, material and testing procedures used in the study are described.

3.1 Experimental
3.1.1 Substrates

1100 aluminum alloy was chosen as the substrate material for coating deposition. Square coupons with dimensions of 25 mm × 25 mm × 5 mm were cut from sheet material. The coupons were manually ground and polished on 240, 400,600, and 1200 grit silicon carbide (SiC) waterproof abrasive papers to obtain a uniform surface roughness of 0.1 ± 0.02 μm. After cleaning with water, the samples were cleaned with acetone before the PEO treatment to ensure a similar initial surface condition for each sample.

3.1.2 PEO coating Process

The coatings were prepared in an alkaline electrolyte containing sodium silicates (Na_2SiO_3) and potassium hydroxide (KOH) added to balance the pH at 12. The temperature of the electrolytes was kept below 25 ^{o}C by a water cooling system. In order to obtain a good connection between the power supplies to the samples, a threaded hole was drilled on one side of each sample. Then the sample was screwed onto an Al rod (and insulated by Teflon tape from the electrolyte) which carried the current from the power supply. The Al samples (as the anode) and a stainless steel electrode (as the cathode) were connected to a power supply operating at different current modes including:

- A unipolar pulsed-DC mode i.e. under only positive polarization of the metal electrode, operating at different frequencies from a 0.2 kHz to 20KHz as well as variable duration

time of duty cycle D_t, where the duty cycle of a pulse train is defined by the relative duration of the pulse-on time,

$$D_t = \frac{t_{on}}{t_{on}+t_{off}} \tag{3.1}$$

- A bipolar current mode, comprising two component, i.e., the positive component and negative component. Process parameters, such as the frequency ($f=1/T$, where T is the pulse period), the duration of each pulse (T_{on}^+ and T_{on}^-, the period of positive and negative pulse respectively) and the resting gap (break) between the positive and negative pulses (T_{off}^+ and T_{off}^- respectively) were adjusted during this study. In each pulse, the pulsed current reached its maximum, after which it remains constant for T_{on} time. In this work T_{on}, it is given by T_{on}^+, whereas, T_{off} corresponded to

$$T_{off} = T_{off}^+ + T_{on}^- + T_{off}^- \tag{3.2}$$

Similar to the study by Me'cuson et al [23], the parameter charge ratio C_R is introduced to represent the ratio of positive to the negative charge quantity where:

$$C_R = \frac{q_+}{q_-} = \frac{\int_0^{T_{on}} I^+ dt}{\int_{T_{on}}^{T_{on}+T_{off}} I^- dt} \tag{3.3}$$

where I^+ and I^- represent the values of the positive and negative current respectively. The values of T^+, T^-, I^+ and I^- were adjusted to find the best available condition for the coating. Figure 3.1 is a schematic diagram of timing of a squared shape current wave form, showing the main controllable parameters of the pulses. Both pulse duration and current density were controlled in order to provide optimal conditions to attain desirable coating morphology and microstructure. Two different current generators (MPE Magna-power supply and MDX Magnetron Drive) were used, which deliver current to the substrate with an amplitude in the range of 0-5 A and 0-15 A respectively. These power supplies were specially designed to allow independent control over the main pulse parameters, such as pulse duration, amplitude and duty cycle, during both positive and negative biasing using a Spik 2000A controller.

The pulse unit SPIK2000A can be operated in many modes (Bipolar, Unipolar, DC- and DC+ modes) with pulse duration (the ON and OFF times) being freely adjustable from the 5µs per pulse unit range to the 32ms per pulse duration range (30Hz

to 50 KHz). The DC sources can be used in the voltage, the current or in the power controlled mode. Experiments were conducted using pulsed DC power supply (AE Magnetron MAX, the output voltage ranging from 0 to 1000V) with current control. The coating was grown at fixed 0.2, 2 and 20 KHz frequencies. The current density was maintained at (0.1 and 0.15 A/cm^2) during the coating process, the voltage was increased gradually with process time so as to maintain the preset current density as the coating thickness increased.

A constant current density was set for each set of experiments. Since the conductivity of the oxide film decreases with the increase of coating thickness, the input voltage between anode and cathode has to increase gradually to maintain the current density. Voltage increment verses treatment time was recorded for each sample.
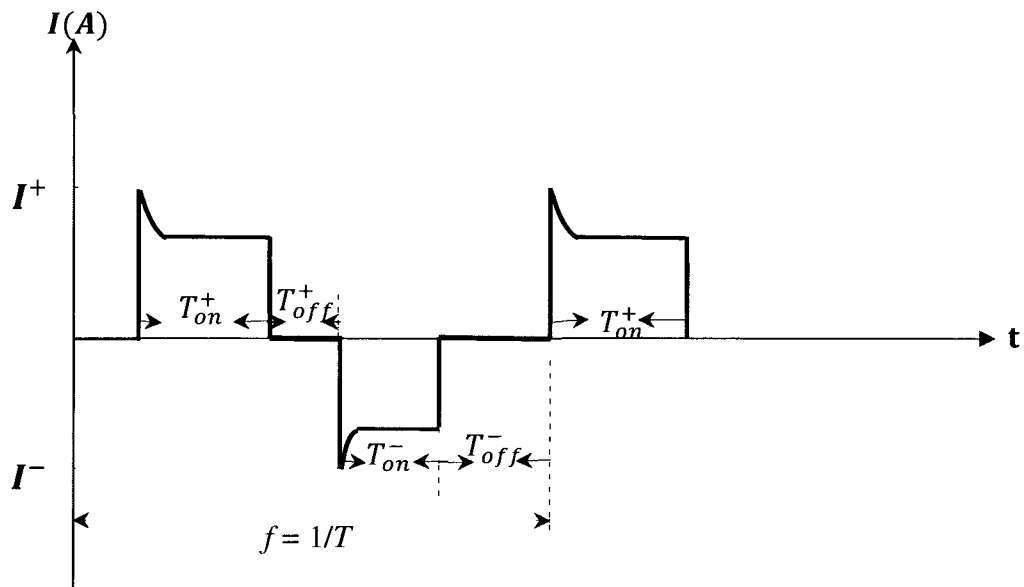
Figure 3.1 Schematic form of the current waveform, showing the main controllable parameters of the pulses.

3.1.3 Summary of PEO process parameters.

An alkali-silicate solution (Na$_2$SiO$_3$-KOH) was used as the electrolyte to produce PEO coating on Al 1100 substrates. Three different current densities 0.06, 0.1 and 0.15 A/cm^2 was used for the coating using Unipolar pulsed DC. Since the conductivity of the oxide

film decreases with the increase of coating thickness, the input voltage between anode and cathode has to increase gradually to maintain the current density. Voltage increment vs. time was recorded for each sample. Three groups of PEO coatings were produced with three different alkali-silicate solutions, 4 g/l Na_2SiO_3 + 1g/l KOH, 8 g/l Na_2SiO_3 + 1g/l KOH and 7 g/l Na_2SiO_3 + 1g/l KOH, listed in Table 3.1. All samples were taken out form the electrolyte, then flushed out by distilled water and dried for the following tests. The process utilizes DC, unipolar pulsed DC in the frequency range (0.2 KHz – 20 KHz) and bipolar current mode at 2 KHz.

Table 3.1 Process parameters for PEO treatment of Al 1100.

Exp. set	No. of Samples	Current density		Current mode	Pulse freq. (KHz)	Electrolyte concentration	Treat. time (min)
		J^+ (A/cm²)	J^- (A/cm²)				
First set	3	0.06 0.1 0.15		Unipolar	2	8 g/l Na_2SiO_3 + 1g/l KOH	60
Second set	16	0.15		Dc Unipolar	0.2 2 A 2 B 20	4 g/l Na_2SiO_3 + 1g/l KOH 8 g/l Na_2SiO_3 + 1g/l KOH	15 60
Third set	3	0.86 1.15	0.57 0.86	Unipolar Bipolar	2	7 g/l Na_2SiO_3 + 1g/l KOH	60 90

3.2 Characterization of substrates and coatings

3.2.1 Surface morphology and coating thickness

The morphologies of PEO coatings and its cross section were observed with a Buehler optical microscope with an image analysis system and scanning electron microscopy (SEM) type JEOL JSM-5800LV (Figure 3.2), equipped with energy

dispersive analysis X-ray EDX, (Kevex 5100C). The oxide coating was sputtered with the gold film in order to be conductive before the SEM analysis were performed to observe surface morphology, measure the thickness and detect the chemical elements. The coating thickness was determined by SEM observation of sample cross sections.. The SEM was operated at maximum accelerating voltage 15KV. Cross-sections of samples were mounted with resin and polished first with a SiC abrasive paper of gradually decreasing grit size, then with an alumina suspension for the final polishing.
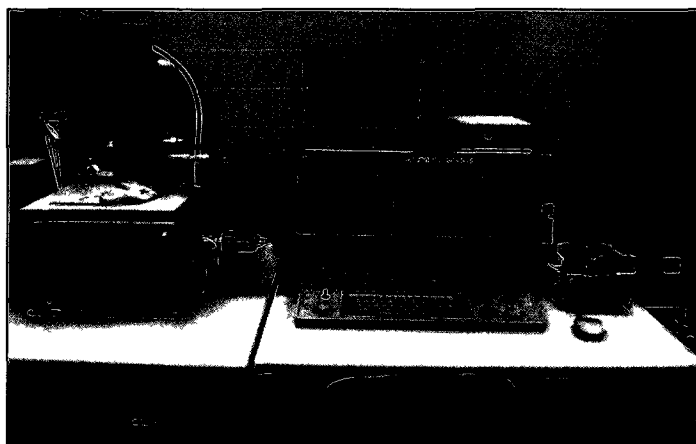
Figure 3.2 JEOL Scanning Electron Microscopes (SEM) with energy dispersive X-ray (EDX).

3.2.2 Surface roughness

The surface roughness (Ra) was measured using a stylus type surface profilometer (Mitutoya Surftest SJ-201P). Each roughness value given was an average of five test values. The accuracy of roughness tests is 0.01 μm.

3.3 Electrochemical testing

3.3.1. Test procedures

Cyclic potentiodynamic polarization tests were performed to study the general corrosion properties of the substrates and the as- fabricated coating at a temperature of about 25°C. A Solartron 1285 Potentiostat (with a Corrware Software) and a conventional three-electrode cell were employed for the corrosion tests. A specimen with

an exposed area of 1.0 cm^2 was the working electrode; a saturated calomel electrode (SCE) served as the reference electrode; a platinum rod was used as the counter electrode. The ratio of the volume of test solution to the sample contact area was 200 ml/cm^2. All potentials are given with respect to the SCE. Figures 3.3 and 3.4 show a schematic and actual view of the corrosion test system. A 3.5wt.% NaCl aqueous solution prepared with distilled water was used as the corrosion test solution.
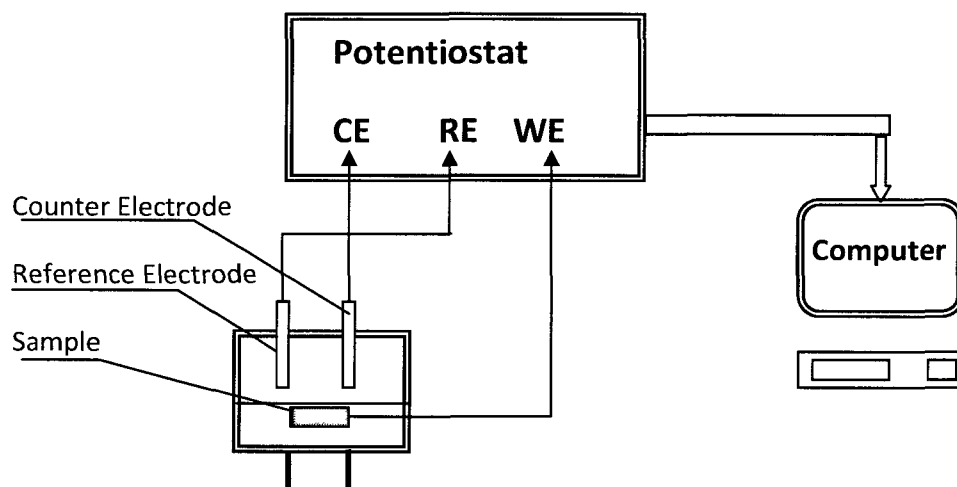
Figure 3.3 Schematic diagram of the electrochemical corrosion test system. CE: counter electrode, RE: reference electrode, WE: working electrode.

Before conducting the potentiodynamic polarization tests, the electrodes were placed in the test solutions under open circuit potential (OCP) for at least 20 mins. After the electrochemical testing system was stable (the OCP reached a stationary value). The measurements were carried out in the test solution at a scan rate of 1 mV/s for 1 cycle. The cycle polarization curves were recorded from a potential -1.0 V to +1.0 V, and back to -1.0 V (Vs. SCE).

Following the potentiodynamic polarization testing, the corrosion current densities were determined by linear extrapolation of the polarization curves, and the polarization resistance of the specimens was calculated for comparison.

Figure 3.4 The view of electrochemical corrosion test system

The corrosion current density (i_{corr}), and the corrosion potentials (E_{corr}, also referred as the open circuit potential OCP) are determined by extrapolation of linear parts of the polarization curves, as illustrated in Figure 3.5. The regions of linearity (with slopes β_a and β_c) are referred to as the Tafel regions. The intersection point between the extrapolated regions gives the values of i_{corr} and E_{corr}. Based on the approximately linear polarization at the corrosion potential (E_{corr}), the polarization resistance (R_p) was determined from the following equation [89].

$$R_p = \frac{\beta_a \, \beta_c}{2.3 \, i_{corr} \, (\beta_a + \beta_c)} \qquad (3.4)$$

According to Faraday's law, the corrosion current density is related to the corrosion rate (r) by the relationship [90]:

$$r = \frac{a.i_{corr}}{nF} \qquad (3.5)$$

where F is the Faraday's constant (96500 coulombs/equivalent), a is the atomic weight, and n is the number of electrons exchanged. From Equations (3.4) and (3.5), it can be seen that there is an inverse proportionality between the polarization resistance R_p and the corrosion rate r. Thus, the higher R_p, the lower is the corrosion rate.
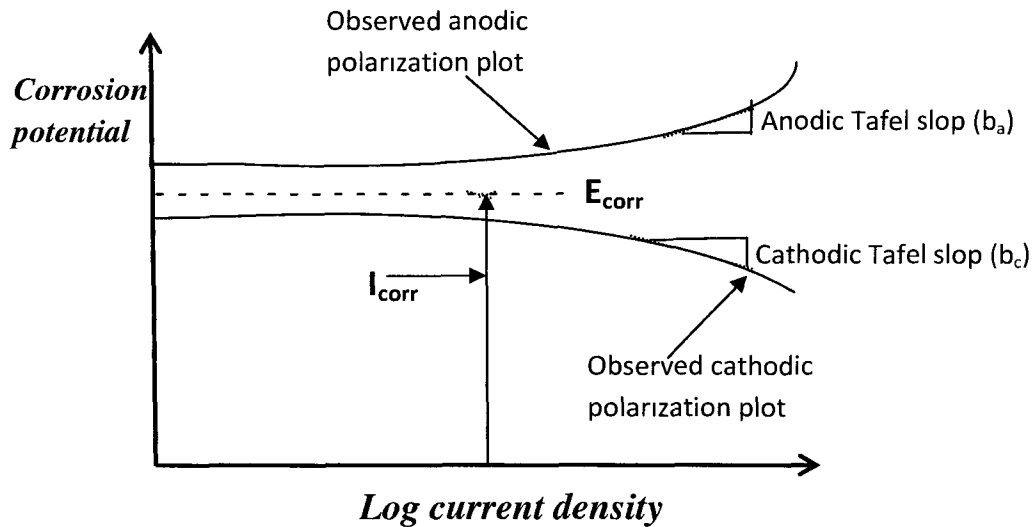
Figure 3.5 Determination of corrosion current density by extrapolation of linear parts of the polarization curve. I_{coor} is the corrosion current density, E_{corr} is the corrosion potential [90].

3.4 Optical Spectrometry

Since the discharges are occurring randomly (source is not emitting equally over the whole sample area) we therefore used an integrated signal that covers whole sample surface area, by focusing all signal emitted from the sample on the fiber optics that connect it to the spectrometer. In this study one spectrometer formed the main visible spectroscopy diagnostic arsenal. The Ocean Optics OES Sensor is PC2000-UV-VIS Fiber Optic Spectrometer with effective range of 200 nm~1100 nm. Its detector consists of a 2048-element linear CCD-array (a charge- coupled device array detector) with a grating of (600 lines/mm) Figure (3.6). The optical bench is compactly mounted on a PC plug-in 1 MHz ISA-bus A/D card, which fits into a slot in the PC. The entrance slit is fixed at 10 mm in width, 1000 mm in height. With no moving part, the optical bench is compactly mounted on a PC plug-in 1 MHz ISA-bus A/D card, which fits into a slot in the PC. A schematic diagram of the experimental setup is shown in Figure 3.7, where the spectrometer collects light transmitted from Ocean Optic P400-2-UV/VIS fiber, which is a 2-meter-long, 400-mm-patch fiber. The light emitted by the plasma was transmitted and

focused through a quartz window and 20mm UV-grade fused-silica lenses mounted on the tank on to the 74-UV collimating lens, 5 mm in diameter, 10 mm in length, and screws on the end of the 400μm diameter optical fiber leading to the entrance slit of the spectrometer.
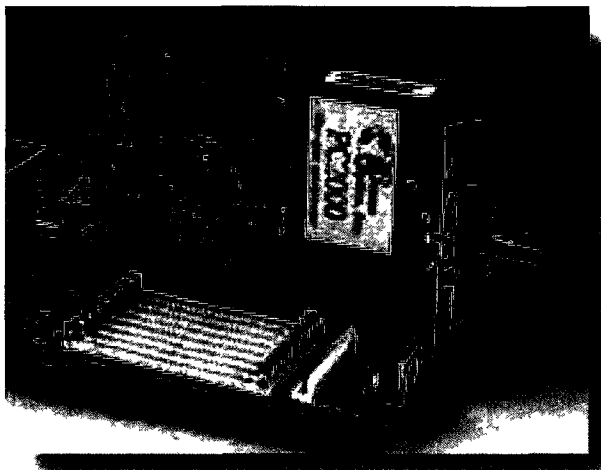
Figure 3.6 Ocean Optics PC2000-UV-VIS spectrometer is mounted on PC plug-in card.
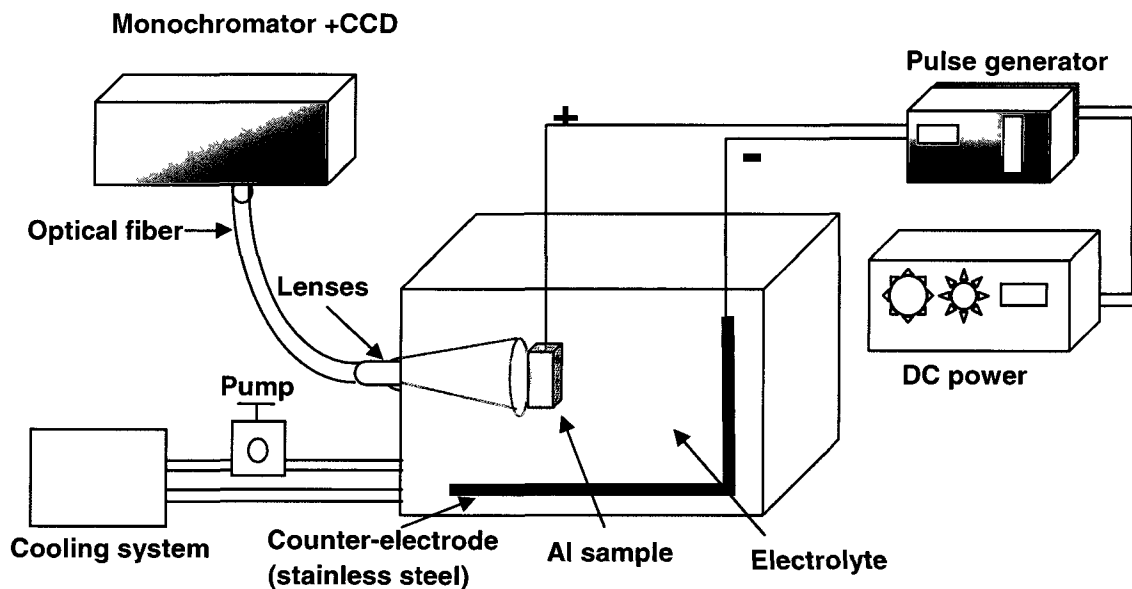
Figure 3.7 Schematic diagram of the experimental apparatus for OES.

Chapter 4 Experimental Results and Discussion I: OES Results

4.1 Determination of electron density and temperature

4.1.1 Determination of electron density from Stark broadening of spectral lines

Several methods were considered for the determination of electron number densities; Stark broadening of the Hβ line was chosen because it provides reasonable accuracy and precision with a relatively simple experimental setup and does not perturb the plasma or require an assumption of thermodynamic equilibrium. For Stark broadening to be a viable method, other sources of broadening need to be either insignificant or taken into account.

Spectral lines have two general attributes, namely their total intensities (which depend on the plasma conditions, in particular the density and temperature) and line profiles, which are effected by many processes, (e.g. Doppler and Stark broadening). Doppler broadening associated with random movement of the radiating atoms (ions), measuring the half width of the Doppler line can be used to determine the kinetic temperature of the plasma. Stark broadening which is caused by the fluctuating electric field produced by the ion and electrons. In dense plasmas, Stark broadening is often the dominant line broadening mechanism. When this is the case, and when the other broadening mechanisms are negligible or can be taken into account, the electron density can be determined from the line widths. In this thesis they will be always referred to as the full half-widths (FWHM = full width at half maximum intensity, for short). The method of calculating the electron density from the measured FWHM of a line is one of the standard plasma diagnostic methods [25].

The theory of Stark contours has been developed most extensively for the H-atom. The line profile of the hydrogen lines especially of the line Hβ have been calculated by a number of authors for temperature and densities. The theories describe the line profile by a function S(α), which is somewhat different in the different theories. The line profile is normalized to [25]

$$\int_{-\infty}^{\infty} s(\alpha) d\alpha = 1 \qquad (4.1)$$

And α is given by [25]

$$\alpha = \frac{\Delta\lambda}{F_o} \qquad (4.2)$$

where $\Delta\lambda$ is the distance from the line center of the unperturbed line in $(\mathring{A})$ and F_o is the Holtsmark electrical field strength and is given by [25]

$$F_o = 1.25 \times 10^{-9} N_e^{2/3} \qquad (4.3)$$

For most diagnostic applications the relationship between full half-widths and electron density is described. The former follows from the relation given above as [25]

$$\Delta\lambda_{1/2} = 2.5 \times 10^{-9} \alpha \ e \ N_e^{2/3} \qquad (4.4)$$

When expressed in wavelength, N_e is given by [25]

$$N_e = C(Ne, T) \Delta\lambda_{1/2}^{2/3} \qquad (4.5)$$

Extensive tables of the broadening parameters C (Ne, T), and S for light elements (Hydrogen through Cesium) have been prepared by Griem [25]. This data was used to determine the electron concentration from the measured half widths of the spectral hydrogen lines. The broadening parameter C (Ne, T) for line H is almost independent of temperature. The method of determining the electron concentration from the Stark broadening of the spectral lines does not require the presence of Maxwell's velocity distribution of the electrons.

The error of measuring the electron concentration is determined by varying the equation (4.5) [25]:

$$\frac{\delta N_e}{N_e} = \frac{3}{2} \left[\left(\frac{\delta\Delta\lambda}{\Delta\lambda} \right)_{ran} + \left(\frac{\delta\Delta\lambda}{\Delta\lambda} \right)_{sys} \right] \qquad (4.6)$$

Setting ($\delta\Delta\lambda/\ \Delta\lambda$)$_{ran}$ $\approx$ 5% , $(\delta\Delta\lambda/\Delta\lambda)\,sys \approx$ 5%   we have $(\delta N_e\ /\ N_e$) $\approx$ 15 %. Determination of the electron concentration from the Stark half width of hydrogen lines is one of the most convenient and accurate methods. The hydrogen lines are wide so that they are easy to record and process.

4.1.2 Determination of electron temperature from relative intensities of spectral lines of the same atomic or ionic species

This method is one of the classical methods of plasma physics, and it is covered in detail in [25]. It is often used since it requires only measurements of relative line intensities, where under line intensity the total line emissivity, integrated over the whole line profile, is meant. Spectral lines must belong to the same atomic or ionic species. That means, they must be emitted by atoms of one element in the same ionization stage. Once relative line intensities are known, one uses the relation [25]

$$\frac{I(1)}{I(2)} = \frac{A_{mn}(1)g_m(1)\lambda_0(2)}{A_{mn}(2)g_m(2)\lambda_0(1)} \exp - \left\{ \frac{E_{m(2)} - E_{m(1)}}{KT} \right\} \qquad (4.7)$$

Which is valid if the level populations of the lines in question are populated according to the Boltzmann law; in other words, at least LTE must exist for these levels. I(1) and I(2) are relative line intensities of lines in question, A_{mn}(i) are corresponding transition probabilities, where m designates the upper and n the lower level of the respective line, g_m(i) is the statistical weight of the upper levels, λ_0 (i) are wavelengths of the line centers in vacuum, E_m(i) are energies of the upper levels of lines, and KT is the thermal energy. All quantities appear in ratios, so it suffices to use the same units for quantities corresponding to two lines in question. In particular, it is convenient to express energies of upper levels and thermal energy in electron volts.

The beauty of this method lies in its simplicity, as only relative line intensities have to be measured, a task that is usually much easier than absolute measurements of the same quantities. Also, the calculated temperature does not depend on plasma parameters which are also of great help. On the other hand, the accuracy of the results is usually

poor, because the ratio of line intensities is fairly insensitive to the temperature at high temperatures. By differentiating Eq. (4.7) one readily finds that

$$\frac{\Delta T}{T} = \frac{KT}{\Delta E}\frac{\Delta R}{R} \qquad (4.8)$$

$$\Delta E = E_{m(1)} - E_{m(2)} \qquad (4.9)$$

$$R = \frac{I(1)}{I(2)} \qquad (4.10)$$

If $KT/\Delta E$ becomes comparable or larger than 1, the errors in the relative line intensities are magnified, resulting in a large inaccuracies of the temperature.

4.2. Coating Optical Emission

Optical emission spectroscopy has been used, for the *in-situ* monitoring of the light emission in order to understand the role of plasma in coating formation. Figure 4.1 shows typical emitted spectra in the NUV and visible regions of the plasma discharge, and show that the PEO plasma contains aluminum (from substrate), silicon, oxygen, sodium, potassium, hydrogen α and β Balmer lines and OH (from the electrolyte). Signals from the wavelength region below 285 nm can not be recorded in our experiments, probably due to self absorption by the electrolyte. Intensive emission spectra are evident. Cleary extended lines indicate atomic origin. Atomic spectra database were used in order to assign each line to the characteristic atomic transition [74,75]. The results are listed in Table 4.1. The emission intensity of the active species can be used to indicate whether the plasma is producing the operation conditions required for a certain coating process. Spectroscopy with the OES spectrometer was utilized to examine the spectral lines (Table 4.1) [74] at 288.1 nm (Si I), 309.2 nm (Al I), 396.1 nm (Al I), 466.3 nm (Al II), 486.1 nm (H_β), 589.5 nm (Na I), and 777 nm (OI). The Al I refers to a neutral aluminum atom, while the notation Al II means the singly ionized atom. The experimental data shown in Figure 4.1 demonstrate two main features:

i- Several strong emission lines are seen above a strong continuum, which generally extends toward the infrared, as shown in Figure 4.1(a).

ii- The spectra consist of pure line emissions from many species without any contribution from the continuous radiation as shown in Figure 4.2(b).

In some instances where the strong discharge appeared for a short time, the intensity on the continuum radiation was large enough to dominate the line emissions. For this study, only the line spectrum was used for calculations. Emission line intensity results indicate that most of the species in the plasma had similar trends over the treatment time, for current densities 0.06, 0.1 and 0.15 A/cm^2, although their intensities varied as shown in Figures 4.2, 4.3 and 4.4. The oxygen (O) intensity signal generally increased with the treatment time; this is likely due to the increased amount of oxygen evolution as the process proceeded, as previously observed by Snizhko et al [13].

Table 4.1. Spectral lines observed in this experiment with the wavelength (λ), transition, statistical weight of the upper and lower state g_k and g_i (respectively), energy difference and the transition probabilities (A_{ki}) [74].

Line	λ nm	Transition	g_k	g_i	Energy eV	A_{ki} 10^8 S^{-1}
Si I	288.1	$3s^23p4s\ ^1P \rightarrow 3s^23p^2\ ^1D$	3	5	4.3	1.89
Al I	309.2	$3s^23d\ ^2D \rightarrow 3s^23p\ ^2P$	6	4	4.0	0.738
Al I	396.1	$3s^24s\ ^2S \rightarrow 3s^23p\ ^2P$	2	4	3.13	0.982
Al II	466.3	$3s4p\ ^1P \rightarrow 3p^2\ ^1D$	3	5	2.66	0.53
H$_\beta$	486.1	$4d\ ^2D \rightarrow 2p\ ^2P$	4	2	2.55	0.172
Na I	589.5	$3p\ ^2P \rightarrow 3s\ ^2S$	3	3	1.36	0.614
O I	777.2	$2s^22p^3\ 3p\ ^5P \rightarrow 2s^22p^3\ 3s\ ^5S$	3	5	1.59	0.369
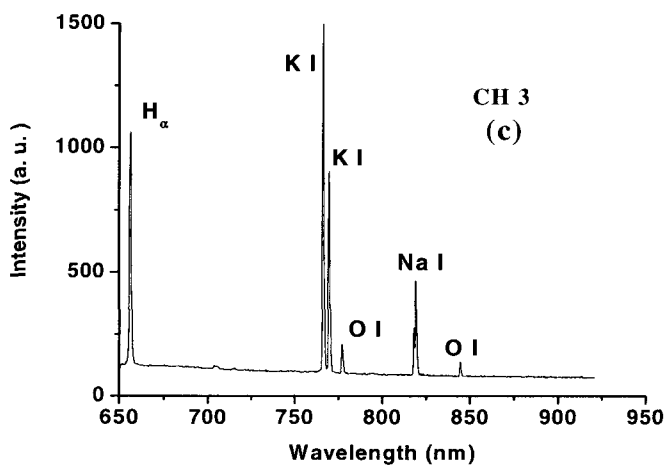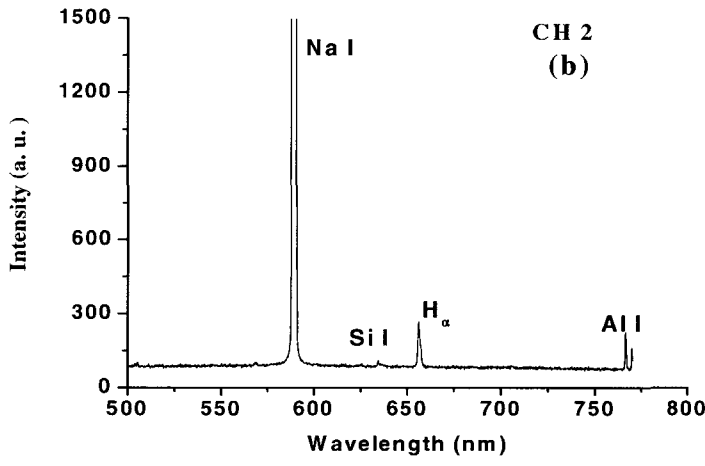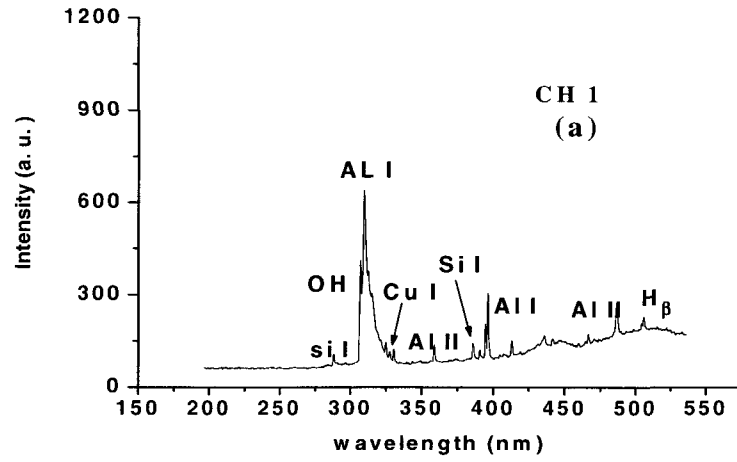
Figure 4.1 Typical emission spectrum using three channels of the spectrometer at J = 0.15 A/cm^2.
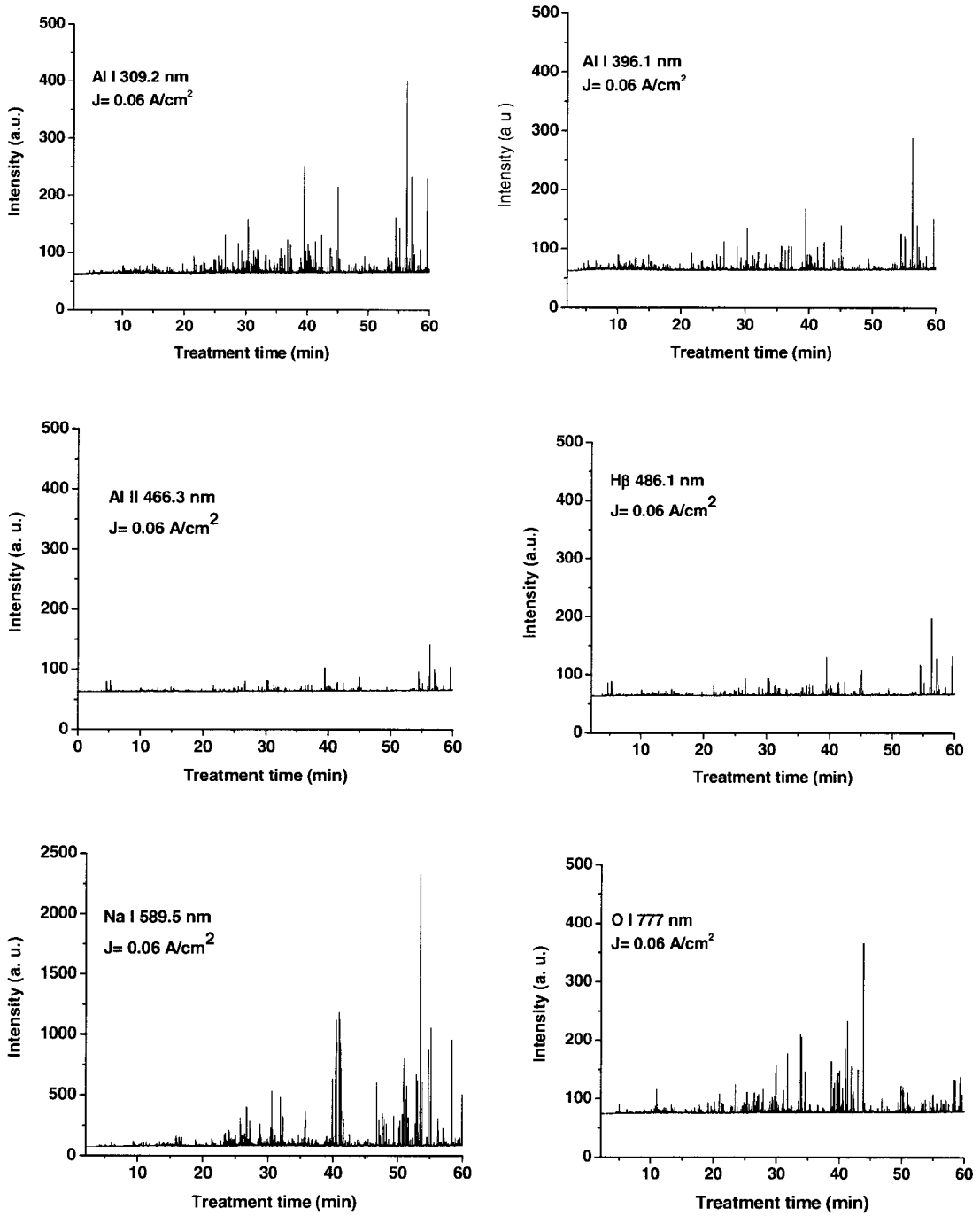
Figure 4.2 Typical time variation of the emission line intensity during the PEO process at a current density of 0.06 A/cm^2.
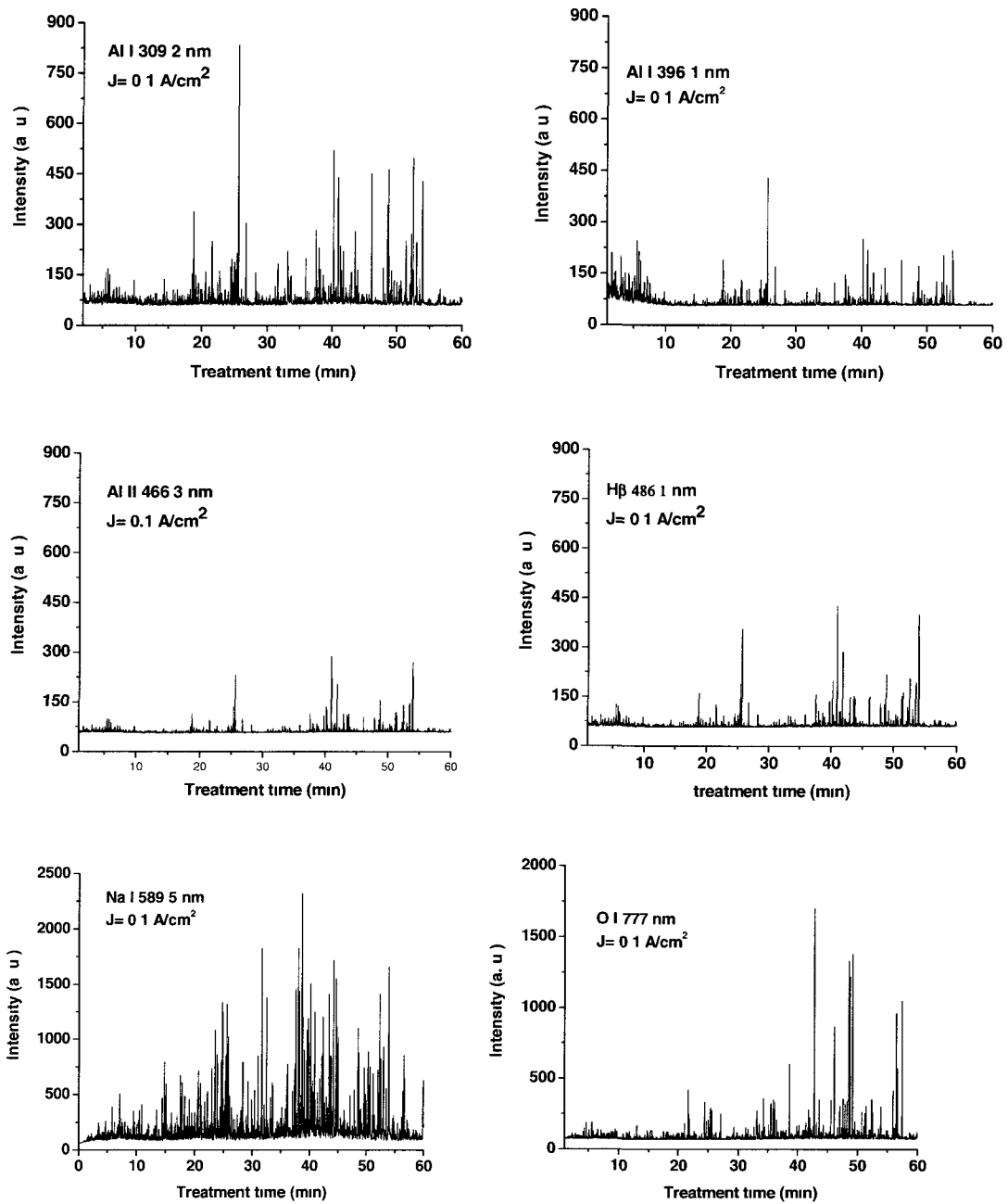
Figure 4.3 Typical time variation of the emission line intensity during the PEO process at a current density of 0.1 A/cm^2.
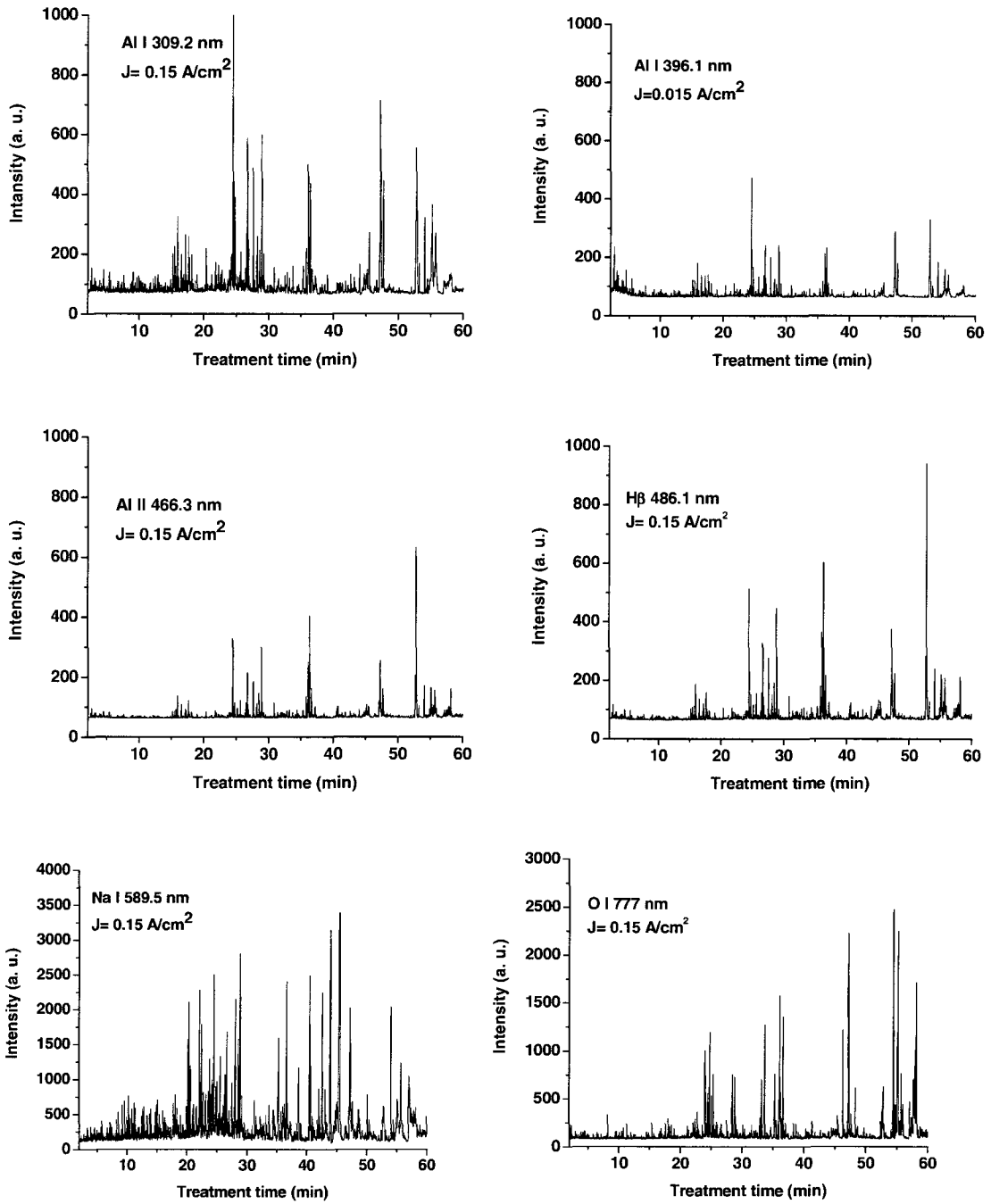
Figure 4.4 Typical time variation of the emission line intensity during the PEO process at a current density of 0.15 A/cm².

4.3 Experimental Results of Plasma Electron temperature and density

4.3.1 Electron concentration.

Based on interpolation from theoretical tables [25] that take plasma temperature into account, plasma electron density as a function of the FWHM of H_β is shown in Figure 4.5(a), since usually they are only weak functions of temperature, quite large deviations of actual plasma temperature from this value produce only small errors in determined plasma parameters. Examples of typical results of a Lorentz profile to experimental data of H_β at specific time is shown in Figure 4.5(b). The H_β peak width (FWHM) for the PEO process at 0.15 A/cm^2 was measured to be 1.3 to 1.8 nm, This half-width corresponds to an electron number density of approximately $(1.5 \pm 0.23) \times 10^{22}$ m^{-3} to $(2.4 \pm 0.36) \times 10^{22}$ m^{-3} which are in good agreement with the plasma electron concentration results of Klapkiv et al [22]. Natural broadening is on the order of hundredths of picometers (pm) and a 0.05 pm broadening would produce only a 0.04% error in this estimate [91], so this contribution can be neglected. Pressure broadening in inductively coupled plasmas (ICP), which are comparable to PEO plasmas in terms of temperature and pressure, is only a few picometers [92]. A 5.0 pm contribution from pressure broadening would produce a 4% error [92], which was judged to be acceptable and, ultimately, was several times smaller than the experimental uncertainty. The electron concentration measurement error (δN_e /N_e) was estimated to be ≈ 15 %, which is a reasonable value in such experiments.
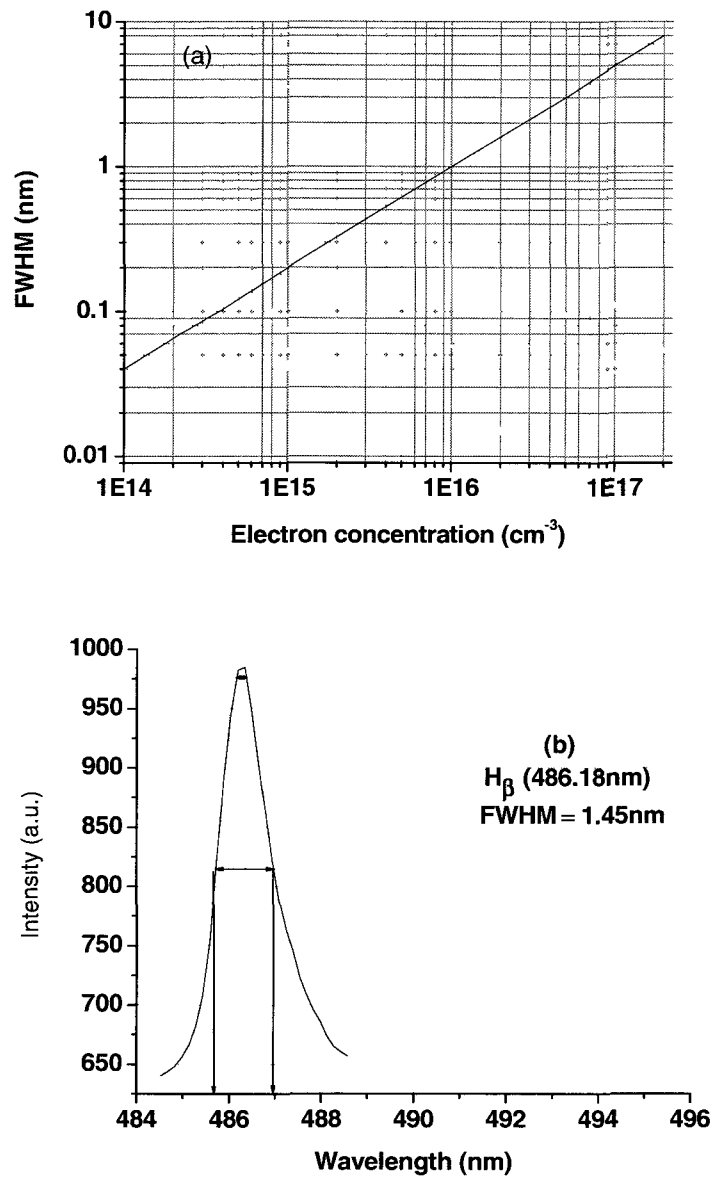
Figure 4.5 Plasma electron density as a function of the FWHM of H_β (a), and typical results of a Lorentz profile to experimental data of H_β (b)

4.3.2 Electron temperature

By combining the Saha and Boltzmann equations [25] the ionization temperature can be calculated, were the intensity ratio of 396.2 nm (Al I) to 309.1 nm (Al I) (from the same ionization stage) was used to measure the plasma electron temperature (T_e), as shown in Figure 4.6. For instance, at a current density of 0.15 A/cm^2, the temperature was

determined to be 4500 ± 450 K to 10000 ± 1000 K, these results are in good agreement with the electron temperature results of Klapkiv et al [22]. The low temperature range (~4500 K) corresponds to the early stage discharges (stage II). After that, the average temperatures (base line temperature) for all three current densities are close to each other (4800 K to 5200 K), which is believed to correspond to the small discharges. The strong peaks (high temperature ~10000 K) shown in Figure 4.6 correspond to strong discharges. Therefore the T_e profile depends strongly on the type of discharge. The T_e does not depend on the number of discharges of each type, because the effect of discharge population density on the temperature is cancelled out by the intensity ratio, since both of I_1 and I_2 (Eq. 3) change with the changes of the number of discharges.

According to the criterion given by Griem [25], the minimum electron concentration required for a plasma to be in local thermodynamic equilibrium LTE for Al, is that $N_e > 2\times10^{23}$ m^{-3} and for H plasma $N_e > 7\times10^{22}$ m^{-3} [20] which are higher than the N_e values of this work. Therefore partial LTE should be considered where the concentration yield is given by [25]:

$$N_e \geq 7.0 \times 10^{24} \; \frac{z^7}{n^{17/2}} \left(\frac{KT}{z^2 E_H}\right)^{1/2} \qquad \text{m}^{-3} \qquad (4.11)$$

where KT is the electron temperature in (eV), E_H (eV) is the ionization potential for the corresponding element , z is the ionization stage and n is the principle quantum number of the lowest quantum level included in the local LTE (for the H, z =1 and n=2). The minimum plasma concentration for partial LTE is $N_e > 4\times10^{15}$ cm^{-3} which is less than the plasma concentration we obtained in this work $(1.5 \pm 0.23) \times10^{22}$ m^{-3} to (2.4 ± 0.36) $\times10^{22}$ m^{-3}. A Local LTE exists; therefore the above estimate of the temperature is valid.
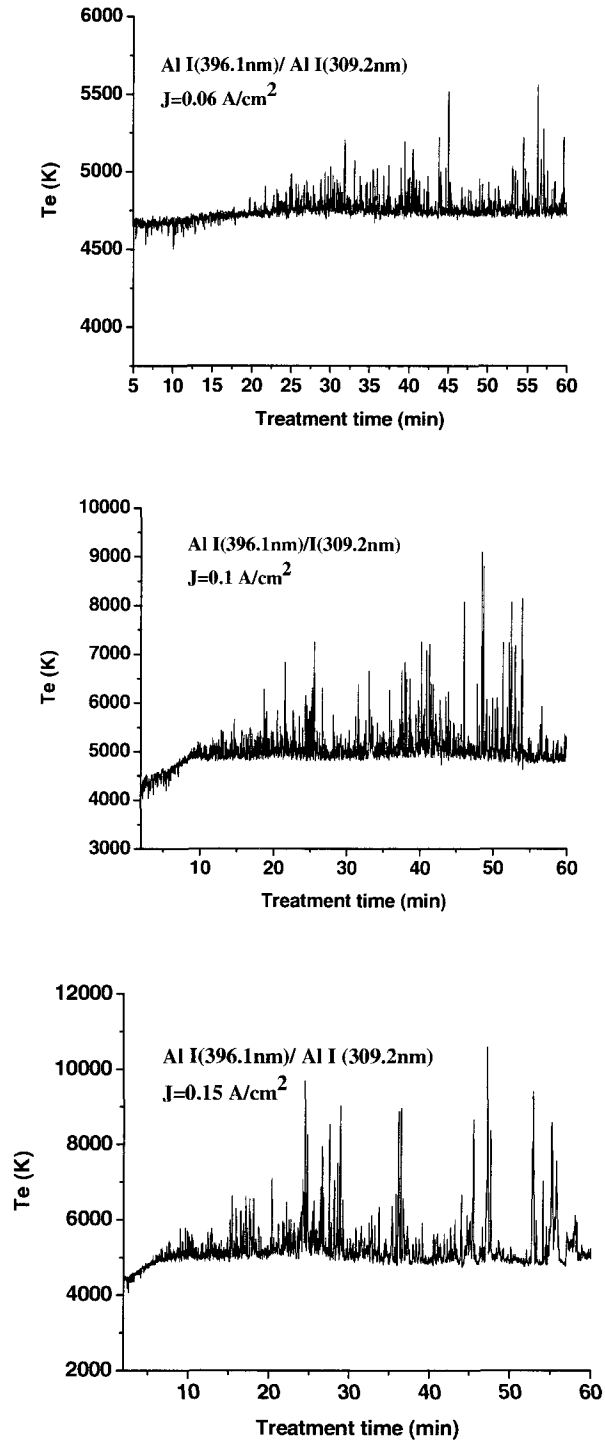
Figure 4.6. Plasma temperature as a function of treatment time (min) determined from the intensity ratio of Al (396.1 nm)/Al (309.2 nm), at a current density of (a) 0.06, (b) 0.1, and (c) 0.15 A/cm^2.

Chapter 5 Experimental Results and Discussion II: Discharge model

An understanding of the discharge processes is very helpful in clarifying the mechanisms of the PEO process. It is worth mentioning that the high intensity peaks shown in Figures 4.2-4.4 and 4.6, indicates a number of strong discharges which take place in the duration time of the peak. However the peak width corresponds to the time period of the strong discharge. As the peak width increased, the sintering time of the ceramic coating becomes longer; therefore the coating structure likely appears better solidified.

5.1 Voltage behavior

Figure 5.1 shows a typical output voltage change during the PEO treatment for different current densities J=0.15, 0.1 and 0.06 A/cm^2 respectively. Taking these output voltage results in combination with our analysis of the emission intensities and temperatures, shown in Figures 4.2-4.4,4.6, one can readily distinguish four stages in the PEO process.

Stage I: In the early stage of the process which mainly involves the rapid electrochemical formation of an initial insulating oxide film, a sharp increase in the voltage was seen. The voltage reached 415 V in 45 sec for J = 0.15 A/cm^2, and 406 V in 60 sec for J = 0.1 A/cm^2, while it took almost 5 minutes to reach 406 V for J = 0.06 A/cm^2.

Stage II: The rate of the voltage change decreases in this stage, which is continued for almost 5 minutes for J = 0.15 A/cm^2 case and 8 minutes for J = 0.1 A/cm^2. A relatively thin oxide layer will be produced by the oxidation process.

Stage III: In this stage the rate of voltage increase becomes slow with average rates of about 1.64 V/min for J = 0.15 A/cm^2 and 1 V/min for J = 0.1 A/cm^2.

Stage IV: In this stage the rate of voltage variation is even slower than that in stage III and it is less than 1 volt/min for all the experiments at the three different current densities.
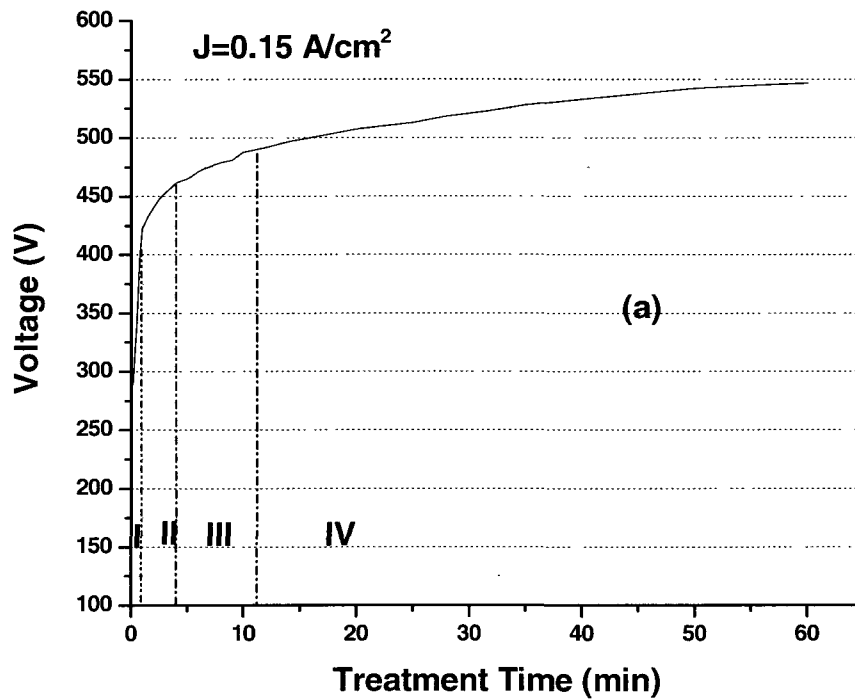
Figure 5.1 Plots of voltage vs. treatment time during the PEO process at (a) J=0.15 A/cm^2, (b) J=0.1 A/cm^2 and (c) J=0.06 A/cm^2. The figure also shows the starting voltage (V) and the time for the four stages.
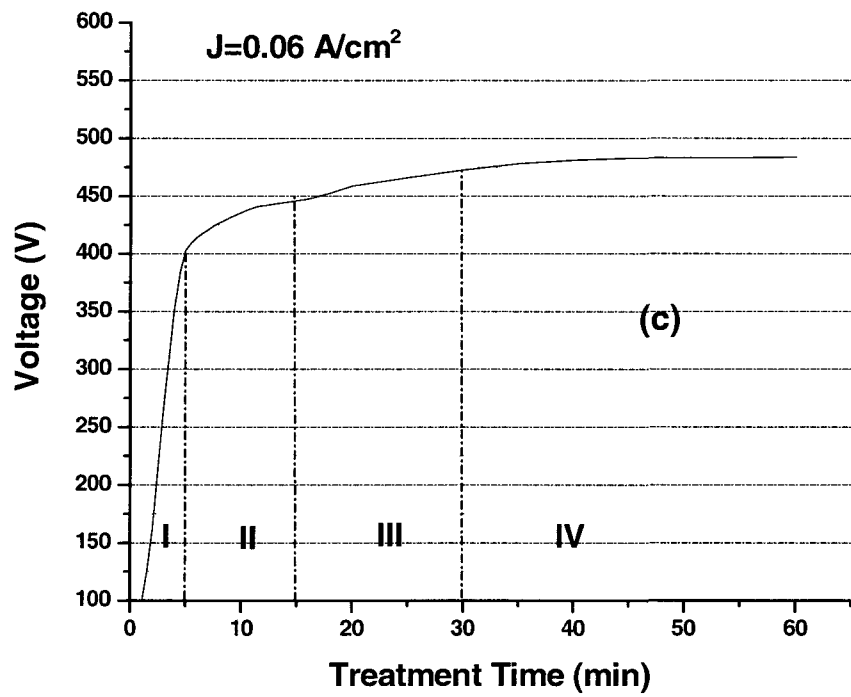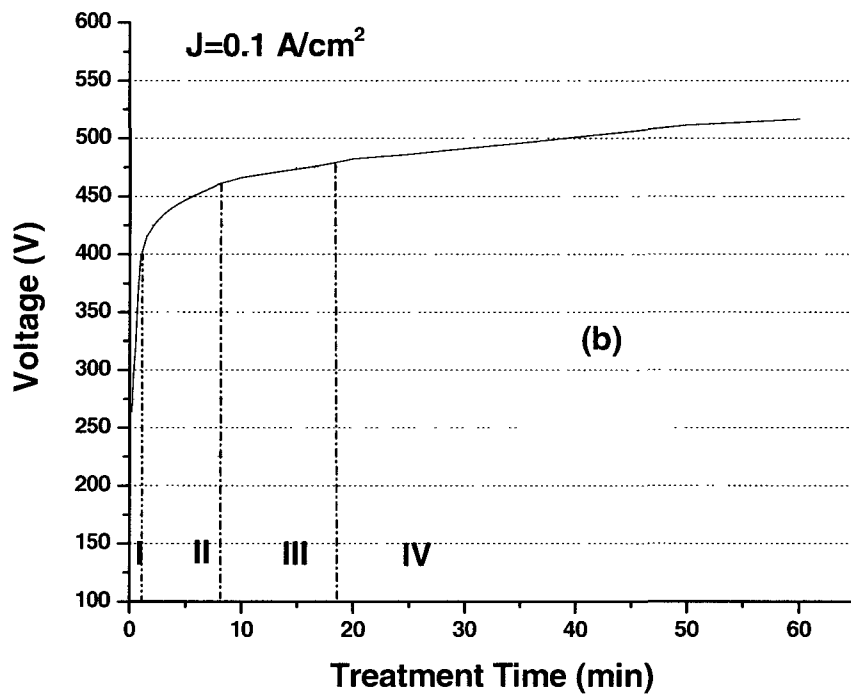
Figure 5.1 Plots of voltage vs. treatment time during the PEO process (continued)

5.2 Plasma discharging appearance

As the plasma coating process proceeds, the discharge appearance changes and the plasma emission intensities varied as shown in Figures 4.2-4.4. These results can be summarized for the previously mentioned four stages as:

Stage I: In this stage where the breakdown voltage is not yet reached, no OES signal of the species (Si, Al, H_β, Na, OH and O) could be detected.

Stage II: This stage is characterized by numerous sparks moving rapidly over the whole sample surface area. There is a significant increase in the intensity of the 396.1 nm (Al I) line at the beginning of stage II. It then reaches a maximum before gradually decreasing. This indicates a start of the breakdown of the oxide layer, an increase in temperature and therefore, melting of the substrate metal, as can be seen from the electron temperature results in Figure 4.6. The higher temperature will be sufficient to excite the aluminum atoms and hence the de-excitation radiation signal can be detected. It is easy to distinguish this stage from the OES results especially from the Al I (396.1 nm) line at J=0.15 and 0.1 A/cm^2. For the J=0.06 A/cm^2 case, the presence of small signals indicate the beginning of the spark (without seeing any noticeable increase in the intensity at the beginning of this stage) probably due to low current density which is not sufficient to excite a large number of aluminum atoms. The transition between stage II and III is characterized by a low variation in the intensity signal as shown in Figures 4.2-4.4.

Stage III: This stage was characterized by a larger but slower moving discharge. As the oxide layer grows, its electrical resistance increases, therefore the nature of the plasma changed as was seen from the intensity signals. This stage showed sharp variations in the intensities in terms of being strong but closely appearing group of peaks, indicating strong discharges. One of the main points of interest in these signals is their consistency with the signal from the species (Si, Al, H_β and O) in terms of general shape and timing as shown in Figures 4.2-4.4. These signals may be interpreted as follows: at these concentrated local discharges, the local plasma temperature is high enough to excite all the species that exist in those locations at that particular time. The low intensity variation which appeared at the end of stage III was followed up by the appearance of strong but largely separated signals. That indicates the beginning of stage IV of the process.

Stage IV: At this stage, concentrated discharges appear as relatively large and long lasting sparks. Large separations were also seen between these strong groups of signals. The strong signals resulted from the long-lasting strong discharges which create more than sufficient energy to cause such intensive ionization processes. However the occurrence of the strong discharges is less frequent than that in stage III due to the thicker coating causing more difficulty in initiation of such discharges. For some cases, such strong discharges may cause irreversible damage to the coatings in stage IV [27]. Figure 4.4 for Al II at $J=0.15$ A/cm^2, shows sharp and strong intensity signals which is an indication of ionization of neutral aluminum to the first ionization stage. These features are in consistent with the temperature measurements shown in Figure 4.6 where at this stage the plasma temperatures are higher and more fluctuating than in the stage III.

5.3 Characterization of surface morphology and composition

Figure 5.2(a) is a typical SEM micrograph of a coated Al sample surface. The treatment on the sample was performed at $J= 0.15$ A/cm^2 for 16 minutes. EDX analyses results are presented in Figures 5.2(b), (c) and (d) at three different positions (A, B and C) which have very different surface morphologies. The coated sample was not polished, and thus the sample surface looks rough. The unpolished coating sample can provide useful information of the coating process and show the interaction between the solution (electrolyte), the substrate and the coating. This information can be linked with the discharge interpretation described in section 5.2.
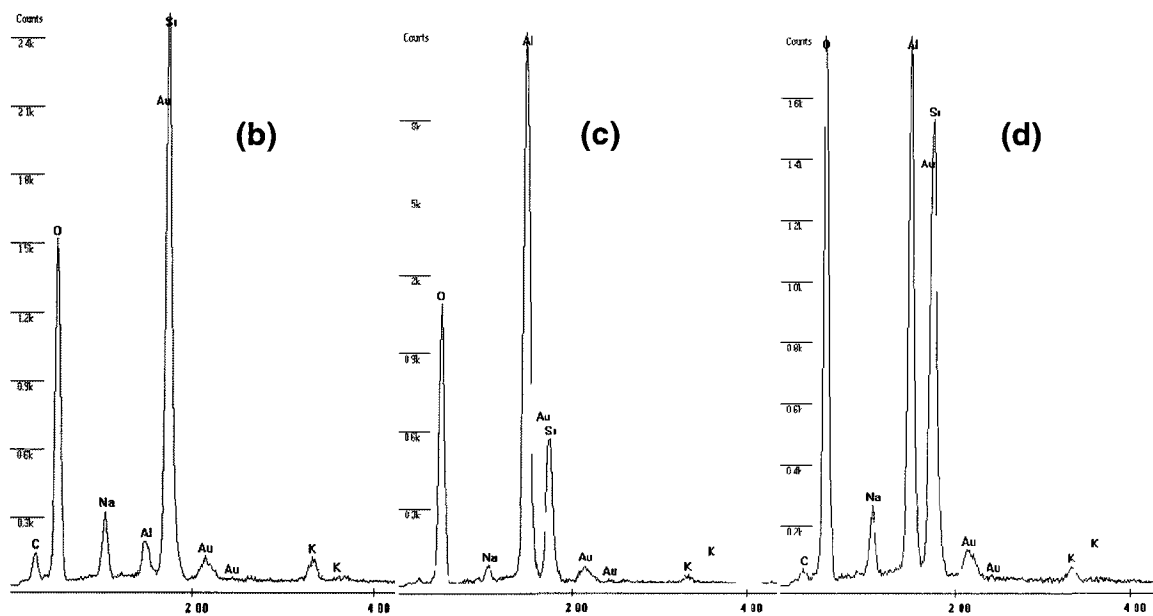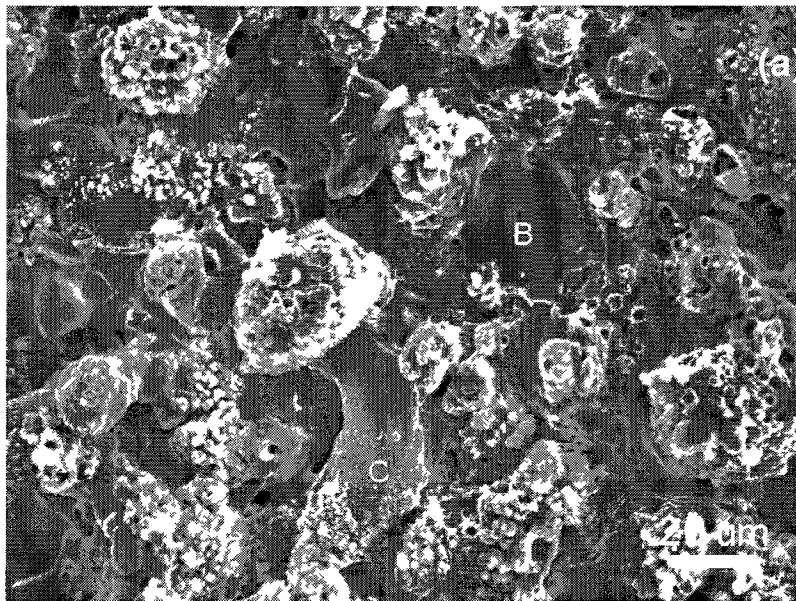
Figure 5.2 (a) SEM micrograph of surface morphology of the coated Al sample; (b), (c), and (d) EDX analysis from regions A, B, and C, respectively.

Table 5.1 summarizes the EDX intensity ratios of Al/Si and (Al + Si)/O. The (Al/Si) peak intensity ratio has a maximum value at position B, then C, and a minimum at position A. Comparing the much higher (Al + Si)/O ratios at position B with those at positions A and C, one can deduce that the Al substrate is more involved in the

discharging in position B than in the position A and C. That means the discharges at positions such as B started from deep at the bottom of the coating, and the discharges at positions A and C more likely occur on the upper and top layers. The elements present in the electrolyte can be more readily integrated into the coating through the surface discharging process.

Table 5.1 EDX results within Figure 5.2(a) at three different locations.

Region	(Al/Si) ratio	(Al + Si)/O ratio
B	3.742	2.26
C	1.185	1.844
A	0.086	1.80

5.4 Interpretation of the discharge appearances

In earlier work [21], three individual models of discharge formation in the PEO process were suggested. The first model [63] defined the microdischarge's appearance as a result of oxide film dielectric breakdown in a strong electric field, the second one [64] considered each discharge as a gas discharge occurring in a micropore of the oxide film (believed to be induced by an initial dielectric breakdown of a barrier layer in the bottom of the micropore [21]), and the third model [66] assumed the possibility of free electron generation and glow discharge ignition in the gaseous media at the oxide-electrolyte interface, which leads to heating, melting and quenching the underlying oxide layer.

The emission intensity data shown in Figures 4.2-4.4, the temperature variation curves of Figure 4.6 and the SEM/EDX results shown in Figure 5.2 indicate that the first two individual models can be distinguished in this study, which allows us to propose a discharge model based on the locations of discharge initiation.

The proposed model provides a better understanding of the origin of the metal signal (aluminum in this work) shown in the Al lines intensity results. These signals may be from two possible sources: the metal surface (metal-oxide interface) and the oxide layer (oxide-electrolyte interface), or from both of the interfaces.

According to the proposed model Figure 5.3, the first possibility would be the production of signals which are due to the dielectric breakdown in a strong electric field

occurring through the oxide layer: shown as B type in Figure 5.3. During the PEO process, when the electric field strength in the oxide layer reaches a critical value beyond which the film breaks down, a localized melt channel is formed, and plasma reactions take place in these channels. Then there is a consistency of the signals from all species existing in the plasma. The radiation intensities of the species are related to excitation caused by electron impact under a high electric field imposed in the discharge channel. The electric field in the discharge channel then decreases with a relaxation time close to the electron life time (10^{-6} -10^{-4} s [20] (i.e. the radiation intensity decreases due to a decrease in the mean energy of the electrons). Because of the high temperature and the strong electric field, molten aluminum is ejected from the coating/substrate interface into the coating surface where it is rapidly solidified by the electrolyte [12]. Therefore strong signals of the Al II, ion which required a higher energy to be created than the Al I, were detected in this work.

For the case of the second possibility, the emission line signals are due to gas discharge occurring in micropores of the oxide film providing that (relatively weak) dielectric breakdown of a barrier layer in the bottom of the micropore is initiated [21]: type A for discharges in relatively small holes near the surface, and type C for discharges in the micropores under the relatively deep surface. During these discharges the temperature increased significantly to a sufficient level to excite the species (e.g. Al I and II) that existed in the discharges. However, the intensity of Al II was much less than for first case, indicating that weaker plasma discharging occurred at positions A and C.

The fluctuations in signal intensities and temperature during stages III and IV (i.e. weak and strong signals) can be considered as a reflection of the different locations of discharge initiation. The strong signals are due to the dielectric breakdown through the oxide layer, whereas the medium and small signals are due to the discharge in the outermost layer (in the deep and surface holes, respectively). In stage IV the strong intensity signal spikes shown in Figures 4.3-4.4 correspond to the preponderance of B type of discharges at that period of time

The EDX intensity ratios of Al/Si and (Al + Si)/O shown in Table 5.1 supports the proposed model (Figure 5.3) where position B corresponds to the breakdown process through the oxide layer down to the Al substrate; hence, the Al concentration will be

higher than the positions A and C. Therefore, the main source of Al at position B will be from the substrate surface. At position C the ratio of (Al/Si) is about 1.2. According to the model shown in Figure 5.3, position C corresponds to discharges which occurred inside the relatively deep surface holes or cracks in the oxide layer. These holes are filled with the electrolyte and therefore when the discharge takes place at these kinds of positions; it will be less intense than those corresponding to B. Both the electrolyte and the substrate will contribute to the composition at these locations. However, at position A the (Al/Si) ratio is low (~0.1), hence, the Si composition, which arises from the electrolyte, is very high and corresponds to discharges that occurred at the interface of the oxide layer and the electrolyte, or in the gases attached to this interface close to the very small holes in the oxide layer. The temperature trends and profiles (including the peaks) in Figure 4.6, the discharge model in Figure 5.3 and the surface morphology in Figure 5.2, are inter-related. While the higher temperature (Figure 4.6) is attributed to the strongest discharge (Figure 5.3, B), the morphology (Figure 8, B) is a result of such a discharge. Type A and C discharges (Figure 5.3) are responsible for the base line and relatively small fluctuations of temperature (Figure 4.6) and the resultant A and C morphologies (Figure 5.2).

Although the SEM and EDX results labeled as A, B and C (Figure 5.2) showed the localized plasma interaction between the electrolyte and coating surface, it is important to note that the discharges shown in Figure 5.3 do not represent individual discharges but collective events. The type A discharge represents all the surface type discharges that occurred at a certain moment, even though the discharges are individual events. The type B discharge also represents a group of intense micro-discharges. Whenever the strong B discharges occurred, high peak spikes would certainly appear on the electron temperature curve, which however, does not exclude the probability of A and C occurrences at the same time. On the other hand, the number of A and C sparks would be significantly reduced due to B discharges which offer a large current "leakage" in the discharge channels. Thus, the high T_e peaks are mainly attributed to the B type discharges.
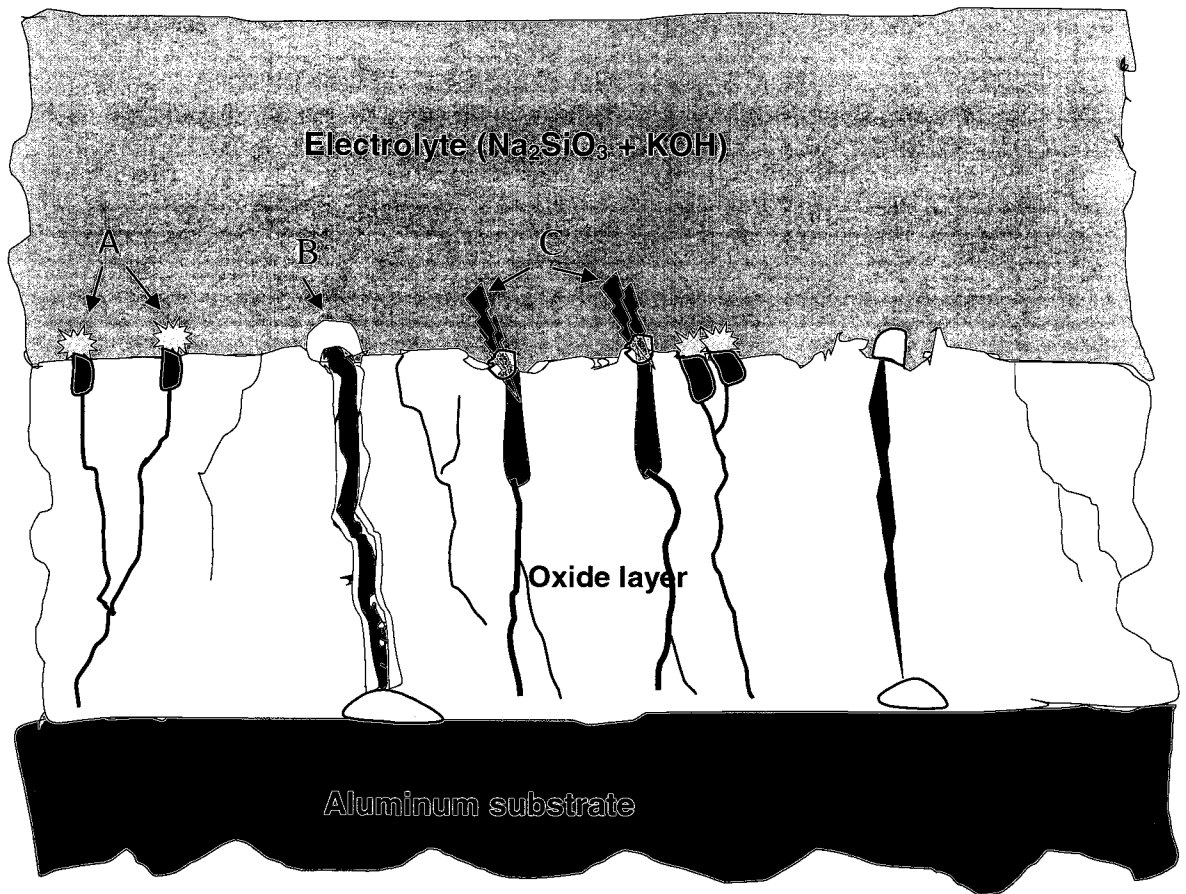
Figure 5.3 Schematic diagram of the discharge models for the PEO process for an Al sample.

Unlike the previous work [20, 59] which monitored the plasma on a relatively small surface area, one of the advantages from this collective OES method is the capability to observe the spectra emitted by small, mild or strong discharges which occurred over the whole sample surface and to study the frequency of occurrence of the different discharges at the different process stages. During the PEO processes the A, B, and C types of discharge (Figure 5.3) can play different roles at different times. At stage II, the mild B type of discharges is dominant since the coating thickness is small; the discharge initiated from the substrate/coating interface is not very strong. Thus the temperature is not high enough to ionize the Al to Al II, although Al I is seen due to the ejection of metal caused by discharges of the B type. The probability of A and C type

discharges are higher than that of the type B discharge in stages III and IV, although the intensity of the B type discharge is higher. At the late stage of stage IV, the strong B type of discharge appears even less frequently but is much stronger. However, the B type of discharges can be influenced by controlling the process parameters (e.g. treatment time, current density, electrolyte type, etc).

It should be noted that the silicate-base electrolyte used in this work was chosen on the following considerations: to study the interactions between the electrolyte and the coating surface during the plasma discharge and to use the elements from solution to trace such interactions. However, all three discharge modes may not necessarily occur for different PEO operating conditions.

It is also worth mentioning that the Na signal can be easily detected and can thus be used as a process monitoring parameter. Based on the Na I 589.5 nm intensity signals shown in Figures 4.3-4.4, the four discharge stages can be identified from the intensity peaks and their separation times. Stage II has a relatively low Na intensity signal but they appear more frequently. The discharge intensities in stage III are larger and the peaks are very close, whereas stage IV exhibits widely separated but intense spikes due to strong discharges. However, at the late stage of stage IV, the Na I signal intensity starts to drop due to a decrease in the number of discharge events. Figure 4.2 (for the case of the lowest current density) shows the same trend but the drop in intensities is not seen yet; it may appear at a longer treatment time.

Chapter 6 Experimental Results and Discussion III: Effect of process parameters on properties of the coatings

6.1 Current frequency effects

Aluminum oxide was deposited on an Al-alloy substrate. The process utilizes DC, unipolar pulsed DC in the frequency range (0.2 KHz – 20 KHz) and bipolar current mode at 2 KHz. The Al samples (as the anode) and a stainless steel electrode (as the cathode) were connected to a DC power supply operating at different modes and different frequencies. During the coating process, the current density was maintained at 0.15 A/cm^2 and the voltage was increased gradually with process time as the coating thickness increased. An alkali-silicate solution with two different concentrations (4g/l and 8 g/l Na$_2$SiO$_3$) was used as the electrolyte with an addition of KOH to adjust the pH to 12. The treatment time was selected to be 60 min to give a coating thickness of approximately 100 μm. Two different current regimes were employed; constant DC current supply and a unipolar pulsed DC current supply (UPDC), with frequencies varied in the 0.2 to 20 KHz range. The power supply was specially designed to allow dependent control over the pulse duration and duty cycle. A key issue in the development of UPDC-PEO process is to determine the optimal frequency range that ensures the best combination of coating growth and surface morphology. The processing parameters for the coated Al samples are listed in Table 6.1.

6.1.1 Voltage variation during PEO processes

The dependency of the anode voltage (V) on the PEO treatment time (t) at DC and unipolar current modes at different frequencies and electrolyte concentrations for the Al 100 alloy are shown in Figure 6.1(a and b). For the 8g/l electrolyte, the applied voltage to the electrodes ranged up to 550 V for the DC mode and up to 600 V for the 2 KHz A case. Thus in the same electrolyte, as we change from DC to UPDC current mode the voltage will higher regardless the frequencies. As can seen form Figure 6.1(a and b) for the 2 KHz A case, the voltage required for the dielectric breakdown is higher than all

other cases, which may be attributed to the longer off time of the current pulses. Similar trends were observed for the process in the 4g/l electrolyte except that at the same conditions, the rate of voltage increase in the 4 g/l electrolyte is much higher than the 8g/l electrolyte for the first stage and slower for the next three stages. As mentioned in chapter 5, the rapidly rise of the voltage corresponding to a conventional aluminum anodizing process. When the voltage was further increased and was over a critical value (above the dielectric strength of the oxides ~ 104 V/mm [12]), the anodic film underwent dielectric breakdown, and small sparks were generated which facilitated the continued growth of the oxide film. These results provide further evidence that a higher concentration electrolyte give rise to a higher rate of voltage increase.

Table 6.1 Coating thickness, growth rate and surface roughness for different current-modes

Current mode	Coating thickness (μm)	Growth rate (μm/min)	Roughness (μ m)
DC	91.5±5.0	1.25	12.26
UPDC at 0.2 KHz	108.0±5.5	1.8	8.55
UPDC at 2.0 KHz A	56.0±2.8	0.93	4.26
UPDC at 2.0 KHz B	55.5±2.8	0.92	5.60
UPDC at 20 KHz	50.0±2.5	0.83	4.55

6.1.2 Optical emission characterization

Relatively strong emission lines were seen in the PEO plasma from aluminum (from substrate), silicon, oxygen, sodium, potassium, hydrogen α and β Balmer lines and OH (from the electrolyte). Spectroscopy with the OES spectrometer was utilized to examine the spectral lines at 309.2 nm (Al I), 396.1 nm (Al I), 466.8 nm (Al II) 486.1 nm (H_β), and 777 nm (OI). Emission line intensity results for the Al emission spectra, Fig. 6.2-6.6, indicate that most of the species in the plasma had similar trends over the treatment time, although their intensities varied.
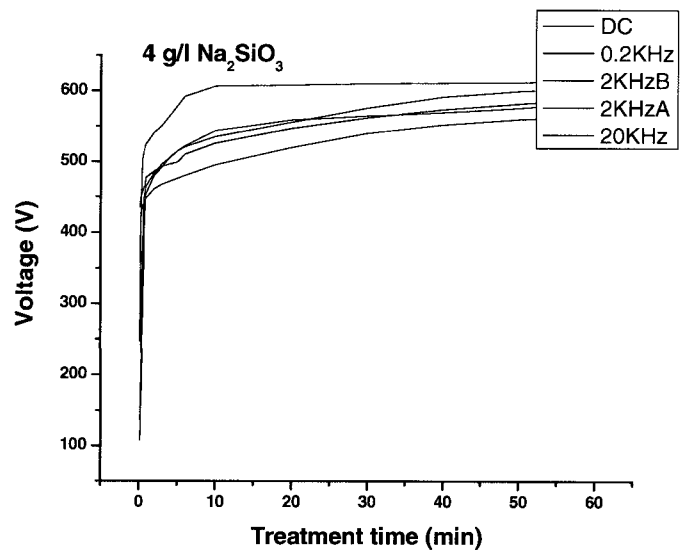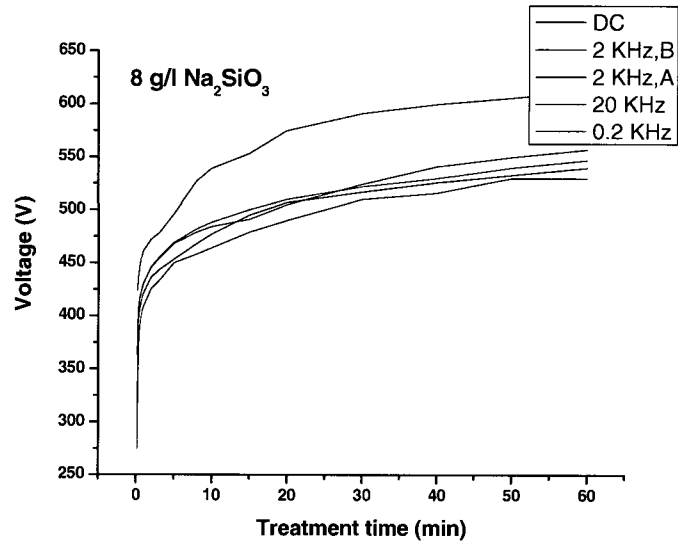
Figure 6.1 Plots of Voltage (V) vs. treatment time (t) during different current modes at (a) 8 g/l and (b) 4 g/l Na₂SiO₃ electrolytes
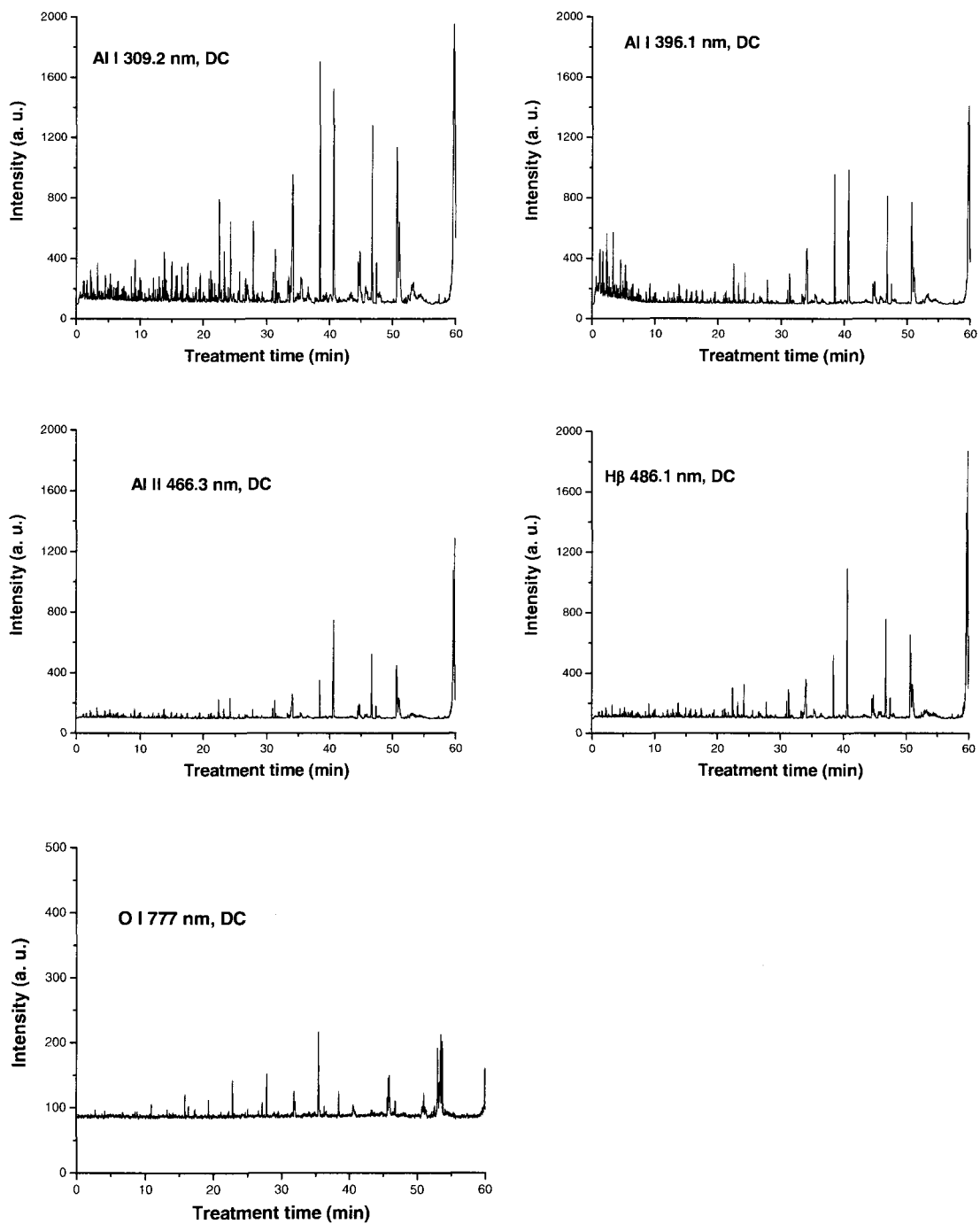
Figure 6.2 Typical time variation of the emission line intensity during the PEO process at (DC) current mode for 8 g/l Na_2SiO_3 at a current density of 0.15 A/cm^2.
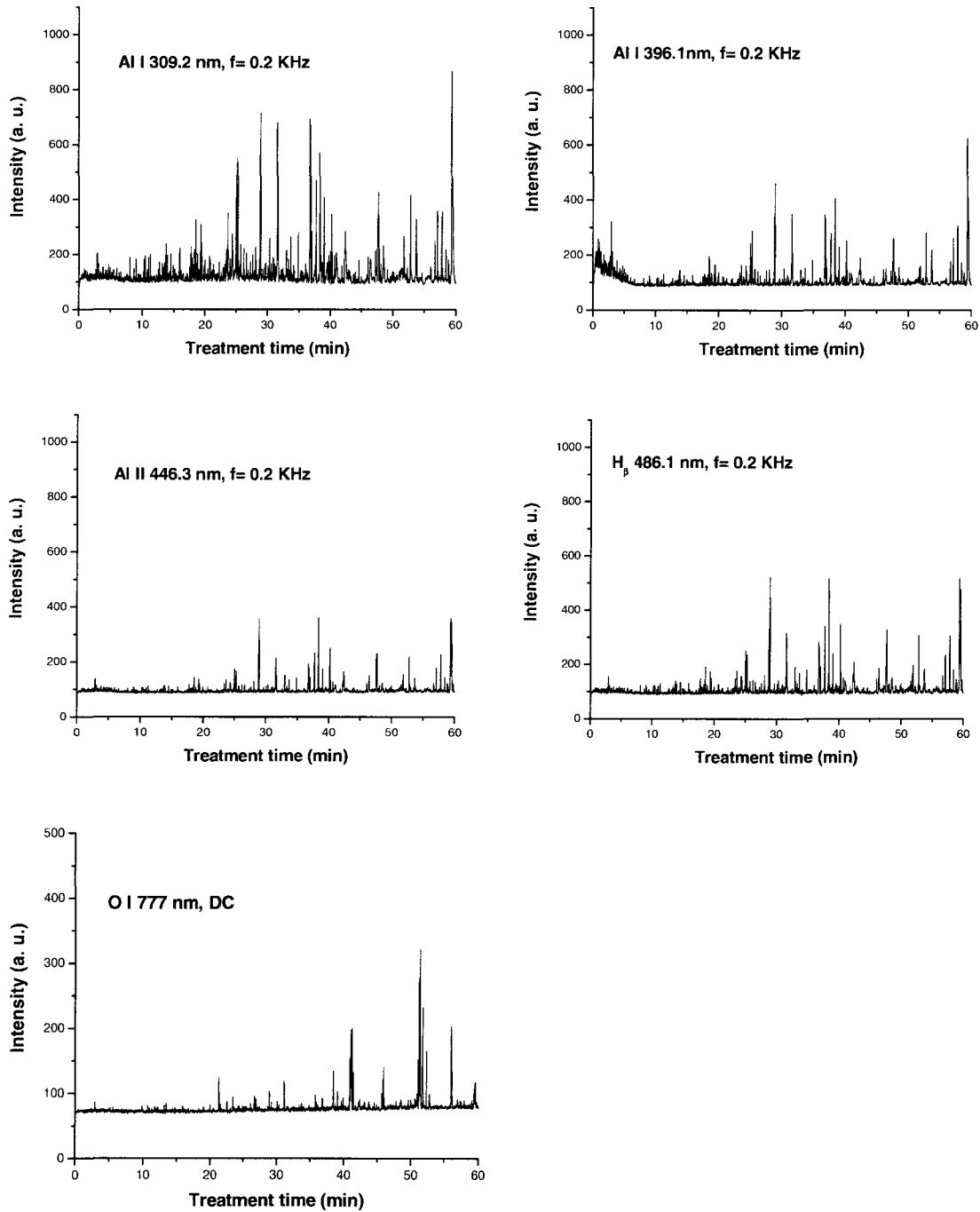
Figure 6.3 Typical time variation of the emission line intensity during the PEO process at (0.2 KHz) current mode for 8 g/l Na_2SiO_3 at a current density of 0.15 A/cm^2.
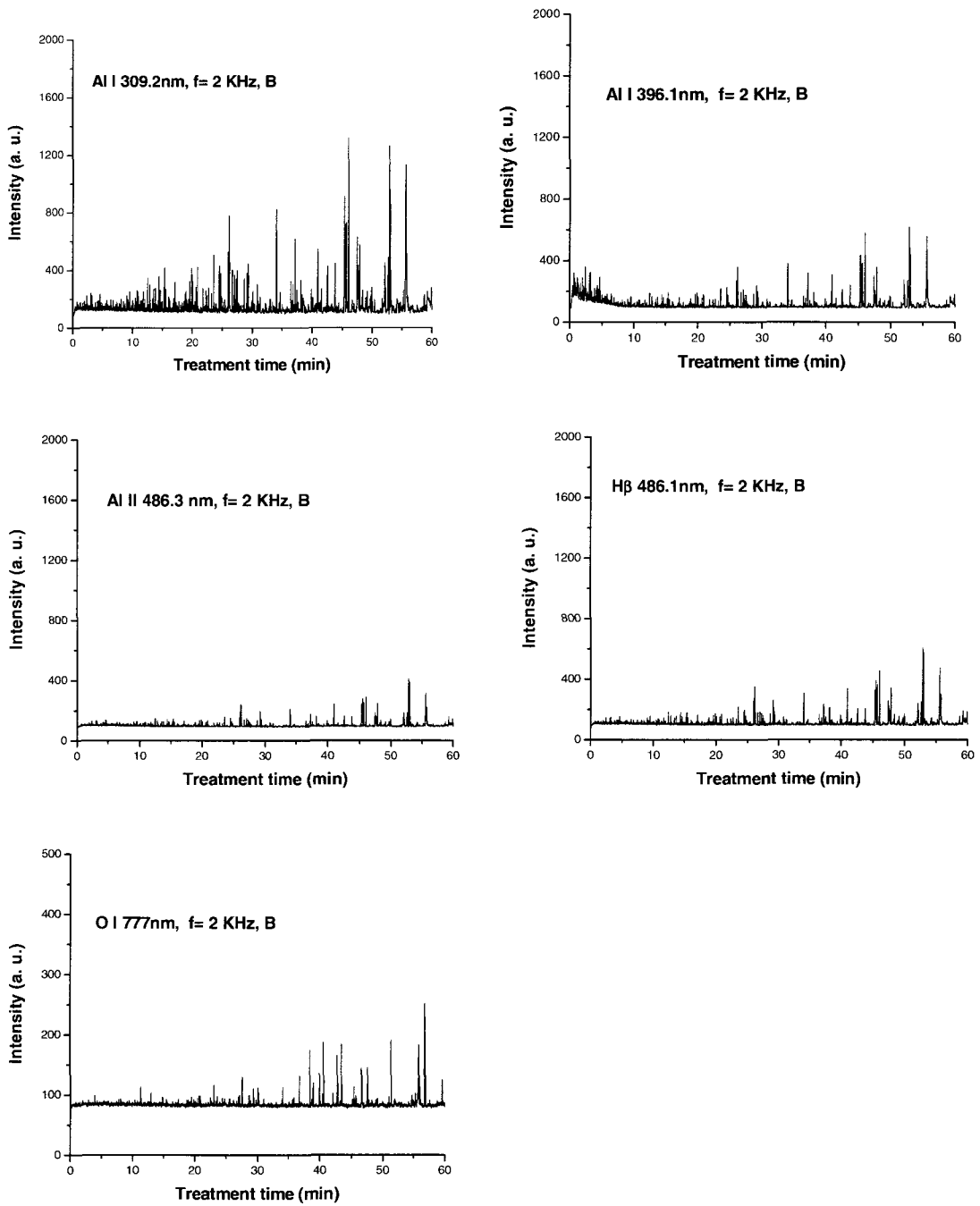
Figure 6.4 Typical time variation of the emission line intensity during the PEO process at (2 KHz B) current mode for 8 g/l Na_2SiO_3 at a current density of 0.15 A/cm^2.
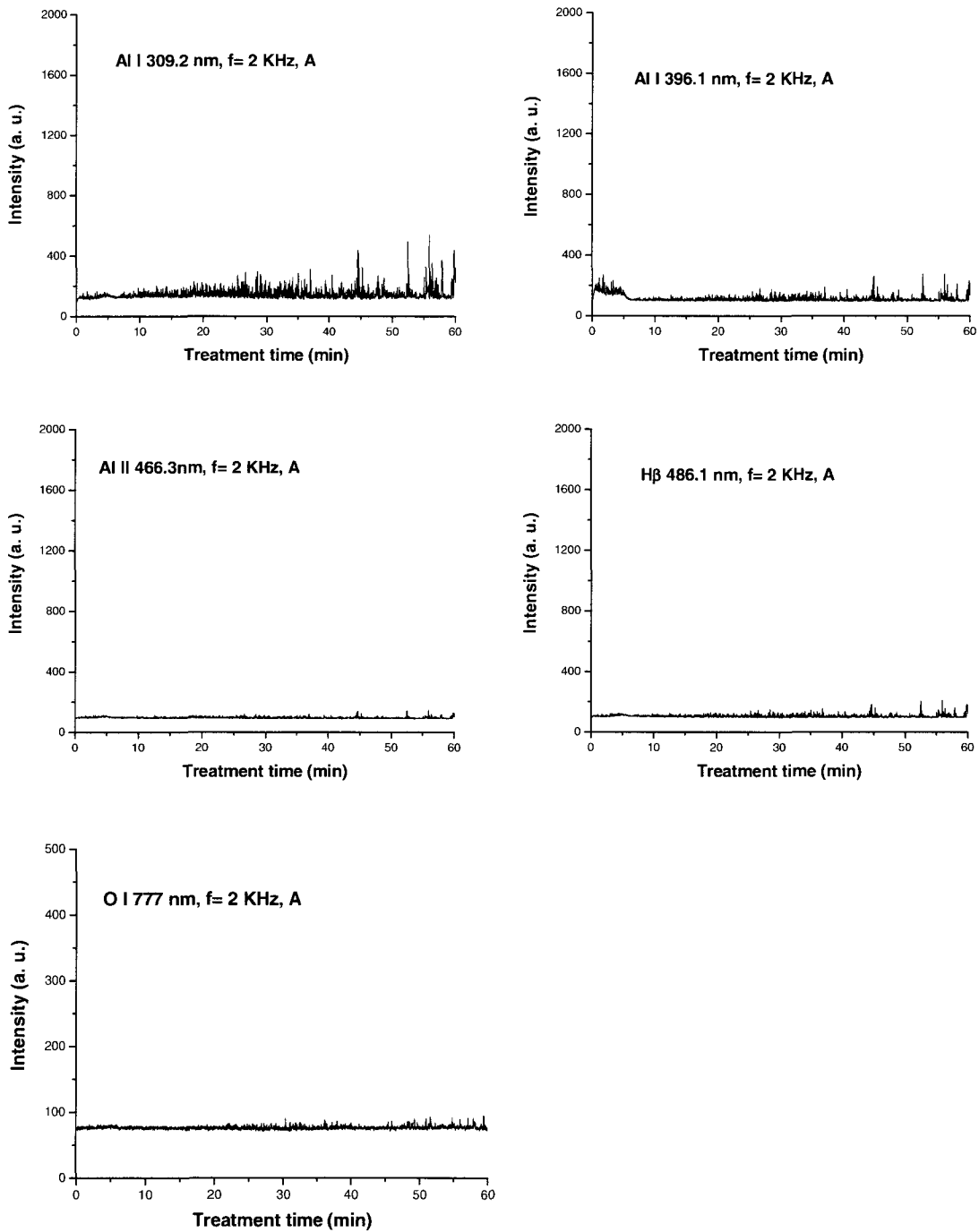
Figure 6.5 Typical time variation of the emission line intensity during the PEO process at (2 KHz A) current mode for 8 g/l Na_2SiO_3 at a current density of 0.15 A/cm^2.
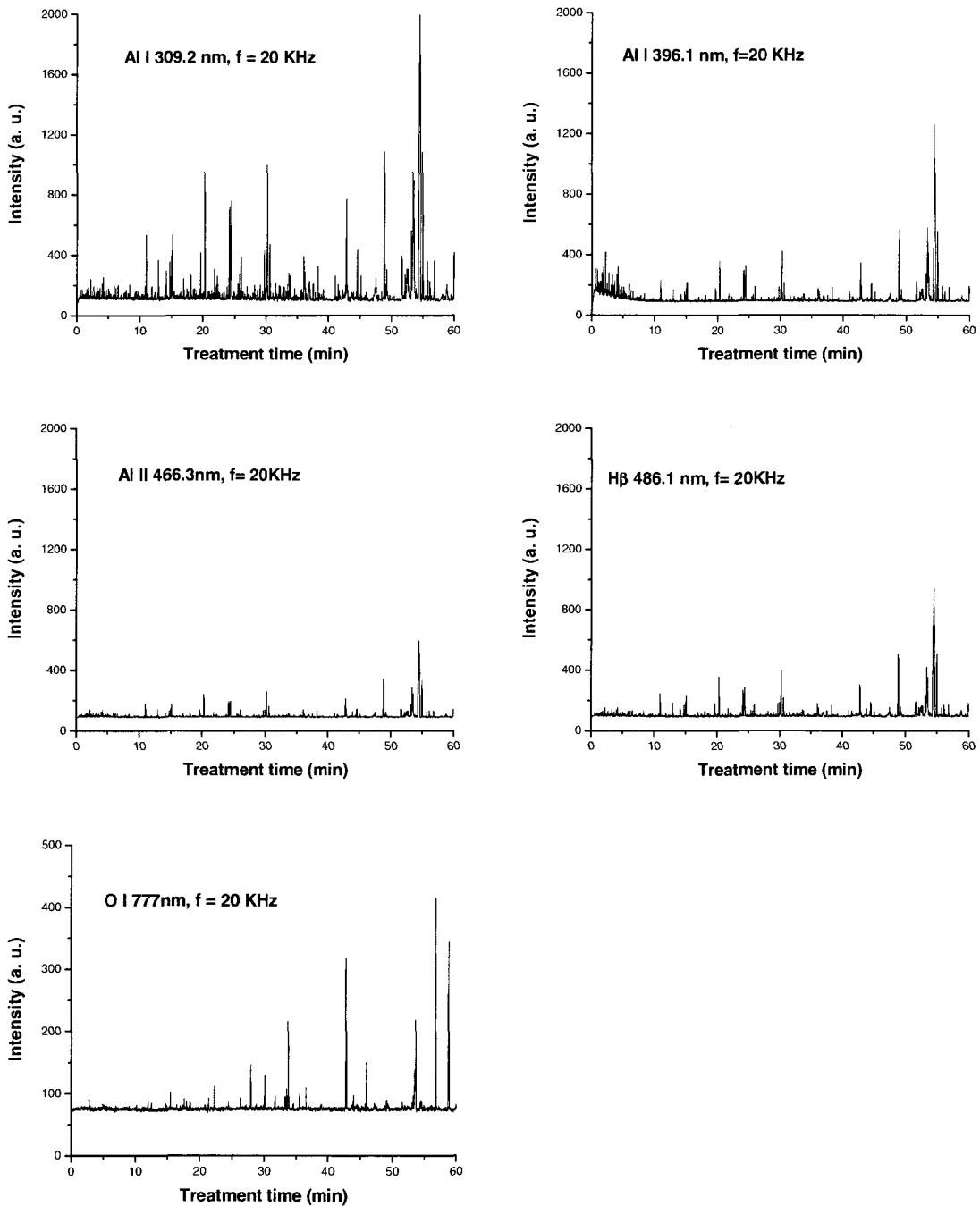
Figure 6.6 Typical time variation of the emission line intensity during the PEO process at (20 KHz A) current mode for 8 g/l Na_2SiO_3 at a current density of 0.15 A/cm^2.

6.1.3 Plasma temperature measurement

The intensity ratio of 396.2 nm (Al I) to 309.1 nm (Al I) (from the same ionization stage) was used to measure the plasma electron temperature (T_e), as shown in Fig. 6.7. The temperature was determined to be in the range of 4500 ± 450 K to 10000 ± 1000 K, for all the cases in this study. These results are in good agreement with the electron temperature results of Klapkiv et al [22]. The low temperature range (~4500 K) corresponds to the early stage discharges. After that, the average temperatures (base line temperature) for all frequencies are in the range of (4900 K to 5400 K), which is believed to correspond to the small discharges. The strong peaks (high temperature ~6000-10000 K) correspond to relatively strong discharges. Therefore the T_e profile depends strongly on the type of discharge.

Figure 6.7(a) shows plasma temperature profile for the DC current mode, where the temperature increase from 4100 K to around 5100 K within 8 min, then the curve start to show many spikes ranging from 5000-8500 K. These spikes corresponding to strong discharges initiated from the sample surface-coating interface. The peak width of the temperature spikes under DC mode is larger than that under pulse modes, due to the long discharge duration time of the sparks (micro-arc). For the case of 0.2 KHz, the temperature increased to around 5000 K within 7 min after the start of the process, and then the average base temperature stayed around 5000 K as can be seen from Figure 6.7(b). The spikes on this curve are shorter than the DC case and the temperature barely exceeds the 7000 K range. This result is comparable with the 2 KHz B results shown in Figure 6.7(d), where the spike temperatures range from 5100 K up to 8000 K. The spike height decreases dramatically for the case of 2 KHz A, Figure 6.7(c), indicating that the strong discharges were eliminated, although intermediate discharges still occur. The average base temperature for the 2 KHz A case is around 5500 K which is higher than the DC and 0.2 KHz cases. Figure 6.7(e) shows much higher spikes with temperatures

reaching 9000 K, which means there is large number of strong discharges produced at this frequency. However, its peaks were sharper than those of other cases.

Figure 6.7   Plasma temperature as a function of treatment time (min) determined from the intensity ratio of Al (396.1 nm)/Al (309.2 nm), for 8g/l Na_2SiO_3 (J= 0.15 A/cm^2).

By changing the electrolyte concentration to 4g/l Na_2SiO_3 plasma electron temperature results shown in fig 6.8 indicates that the spikes appear more frequently and reach a slightly higher temperature. The temperature was determined to be in the range of 5200 ± 520 K to 10500 ± 1050 K, for all the cases in this study. Since the strong peaks (strong discharges) are more frequent in the 4g/l case compare to the 8g/l concentration, therefore the higher concentration electrolyte was used in this study.

6.1.4 Discharge behavior.

According to the model described in Ch. 5 of this thesis, B-type discharge dominates the Al signals for the DC, 0.2 and 20 KHz cases; while the C and A discharge types have a significant role beside the B-type discharge for the 2 KHz B case, although the B- type are still relatively strong but weaker than the other three cases. A weaker B-type discharge, together with C and A type discharges are the dominant discharge types for the 2 KHz A case.

Figures 6.2-6.6 shows OES signal for Al atom at 309.2 nm and 396.1 nm for the unipolar current mode at frequencies 0.2, 2, and 20 KHz as well as at DC mode. The high frequency 20 KHz (short pulse) causing highly ionized plasma, by increasing the impact ionization [21], therefore the plasma temperature is increased as shown in Figures 6.7. The high frequency pulse DC current triggers ignition of short and intense plasma microdischarges at the sample/coating interface, creating more B type discharges. A DC and low frequency (0.2 KHz) DC mode produces long-lived, large micro discharges initiated by thermal ionization, which clearly appear in the OES Al intensity signal, thus the intensity pulse width and the temperature results indicate some enlarged (widening) of the signal and the temperature compared with the high or intermediate frequencies (2 and 20 KHz). Figures 6.2-6.6 show large peaks corresponding to B-type discharge for both the DC and 0.2 KHz cases. Since the morphology mainly depends on when the B-type discharge occurs, by controlling the B type discharge, the quality of the coating can be controlled.
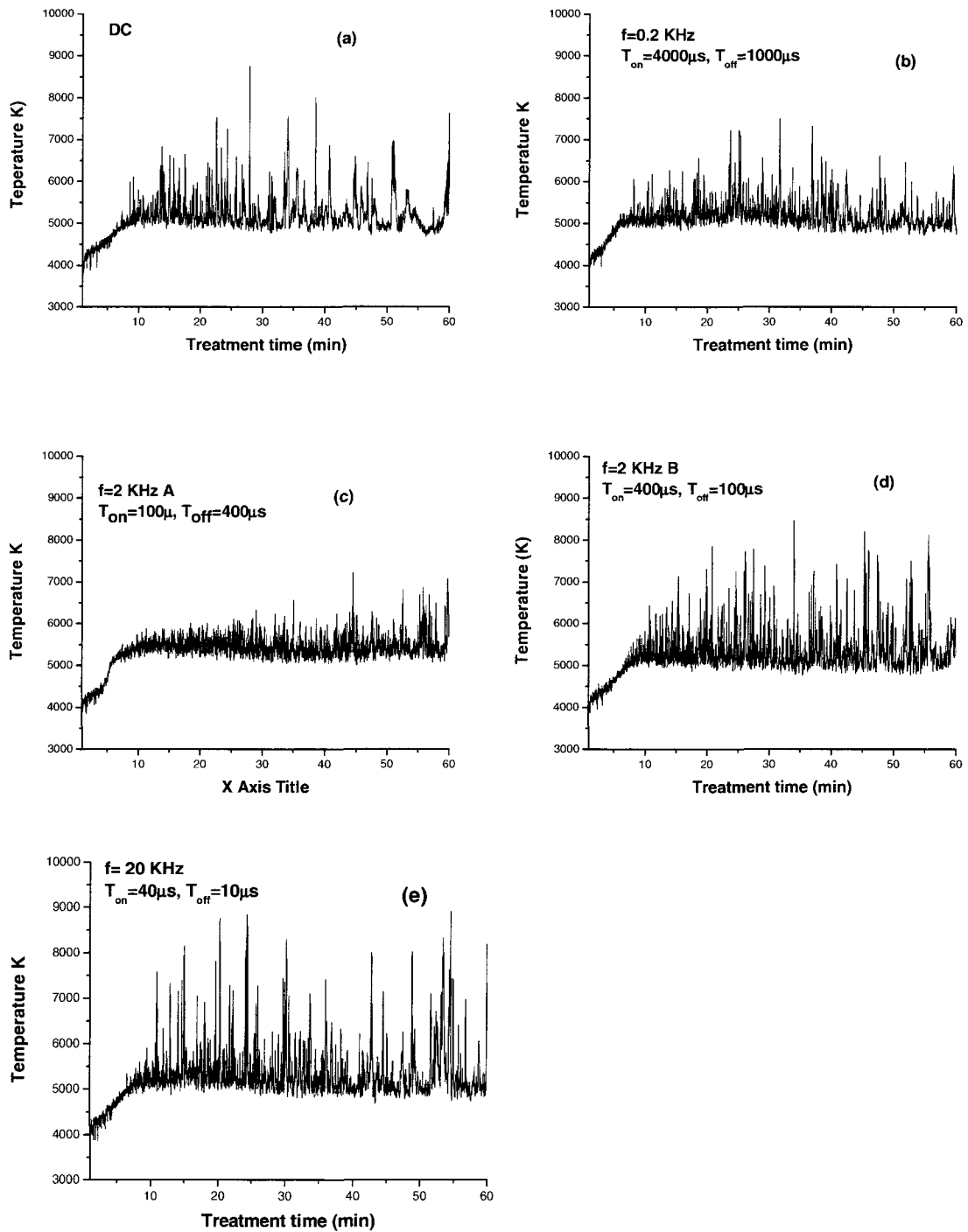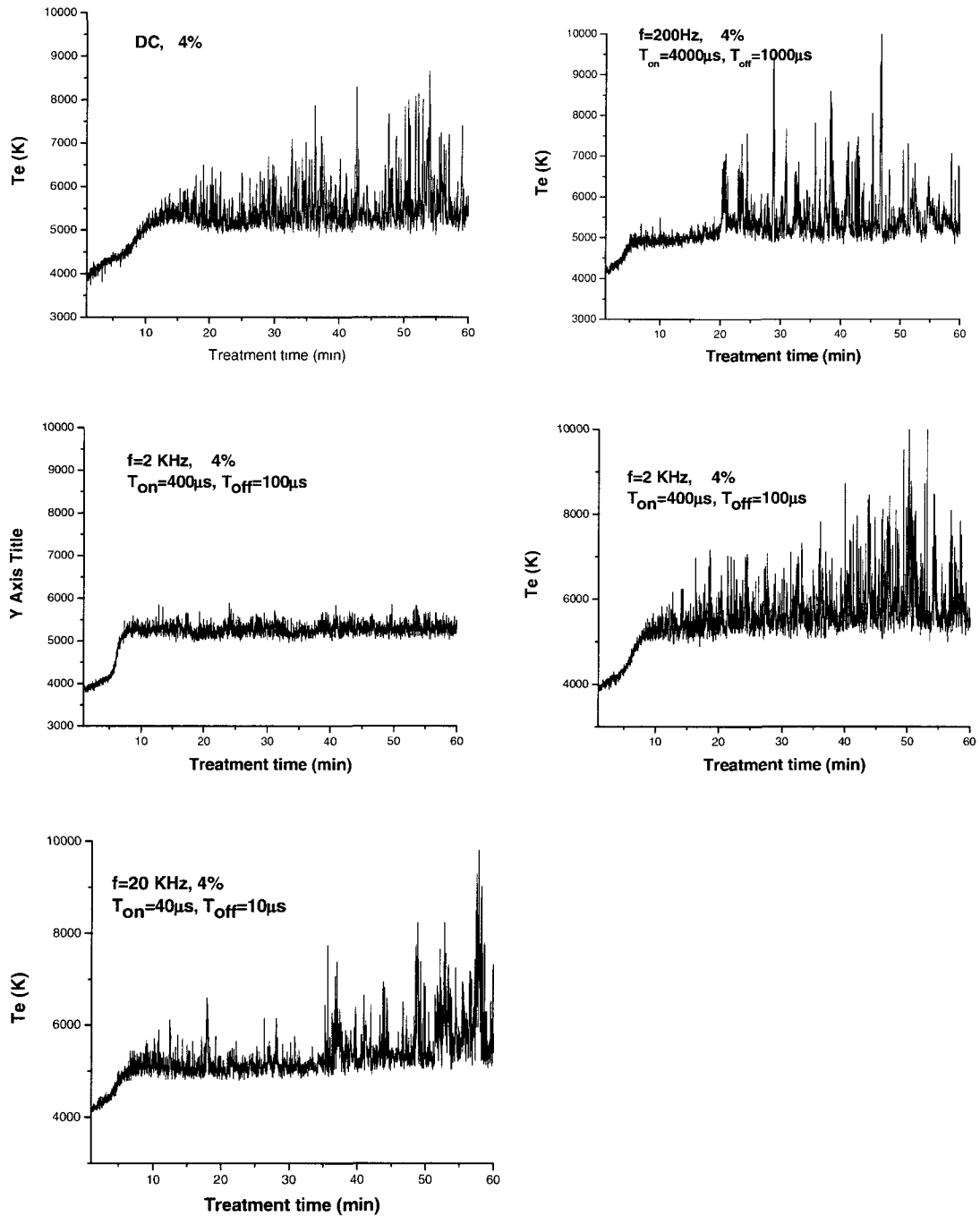
Figure 6.8   Plasma temperature as a function of treatment time (min) determined from the intensity ratio of Al (396.1 nm)/Al (309.2 nm), for 4g/l Na₂SiO₃ at a current density of 0.15 A/cm².

For 2 KHz, A and B cases Figure 6.7 (c and d) where A is for the case of $T_{on} = 100$ μs, $T_{off} = 400$ μs and B for $T_{on} = 400$ μs, $T_{off} = 100$ μs. It is clear that applying longer T_{off} time than T_{on} time of the current pulse to the substrate greatly eliminate the B-type discharge which would significantly change the morphology of the coating surface and cross section.

6.1.5 Surface morphology

Figure 6.9 shows the surface features of PEO treated Al1100 for different coating operation conditions. All the samples show a "pancake" structure wherein the center of each pancake was a discharge channel through which the molten aluminum flowed out of the channel and rapidly solidified leaving distinct boundaries that define each pancake.

Figure 6.9(a) is a SEM micrograph of the coating prepared with the DC mode and shows a number of pancake-like features and pores in the coating. The pancake structures are due to strong discharges of the B-type. The deep holes suggest that the discharges penetrate through the entire thickness of the coating. Therefore the number of pancakes reflects the number of spikes appearing on the temperature results of Figure 6.7(a). The small pores reflect surface discharges, designated as A and C. The diameter and features of the pancakes and pores provide some indication of the strength of individual discharge and whether they were from the coating surface or from the interface. The DC mode results in Figure 6.9(a) clearly indicate the presence of molten regions that rapidly solidified and covered the discharge channels, leading to better sintering due to the long sintering time.

In the 0.2 KHz process more pores and cracks remain on the surface of coating, Figure 6.9(b), and the density of pancakes is less than that for the DC case, which is in consistent with the temperature results. The high number of gas discharges on the upper layer regions of the coating surface causes a high density of small holes. Comparing Figure 6.9(c) to Figure 6.9(d) for the 2 KHz A and B respectively, it is clear that there are less pancake structures, and they have a smaller diameter, for the case 2 KHz A, where the spikes in Figure 6.7(c) are very small, indicating less strong discharges. Due to the

presence of strong discharges for the 2 KHz B case, the pancake structure is larger and denser than that of 2 KHz A case as shown in Figure 6.9(d), however the solidification of such structure is less intensified than that for the DC and 0.2 KHz cases. The flower-like shapes and small holes shown on Figures 6.9(c and d) reflects a higher average base temperature, Figure 6.7(d), due to the presence of many A and C type discharges. For the case of 20 KHz PEO treatment, the discharge channels appear as deep circular/elliptical spots distributed over the surface of the coatings. The existence of such a large number of holes (pancake structure, Figure 6.9(e)) reflects the large number of strong discharges associated with the very high frequency 20 KHz mode as indicated in Figure 6.7(e). The high spike temperature generated by strong discharges likely melts the oxide and then traps gas into the melt pool, resulting in some porosity at the interface. By eliminating the high temperature spike, a denser interface layer and homogenous coating morphology is produced.

6.1.6   Cross-sectional structures of the coatings

The cross-sections of PEO coatings on Al substrates examined by SEM are presented in Figure 6.10(a-e) for treatment times of 60 min. The oxide layers have thicknesses ranging 50 μm to 108 μm: see Table 6.1. The coatings exhibit two distinct regions, namely thick, dense inner region and thin granular outer region.

Figure 6.10(a) shows a cross-section of the ceramic coating for the DC current mode. The coating shows a high level of sintering, but some porosity and holes still exist within the coating and near the oxide-metal interface. For the low frequency 0.2 KHz results shown in Figure 6.10(b), the thickness of the oxide layer is larger than that for the DC case, but it has a higher porosity. For the 2 KHz A, the coating appears to be well bonded with the substrate; nevertheless the coating exhibits some porosity with less sintering appearance, Figure 6.10(c). The coating with 2 KHz B seems to have more sintering effect than that for the case 2 KHz A; however the interface still shows some porosity; both cases of 2 KHz have a similar coating thickness. On the other hand, the coating layer for the 20 KHz case is relatively thin, with some porosity, and has an irregular coating interface.
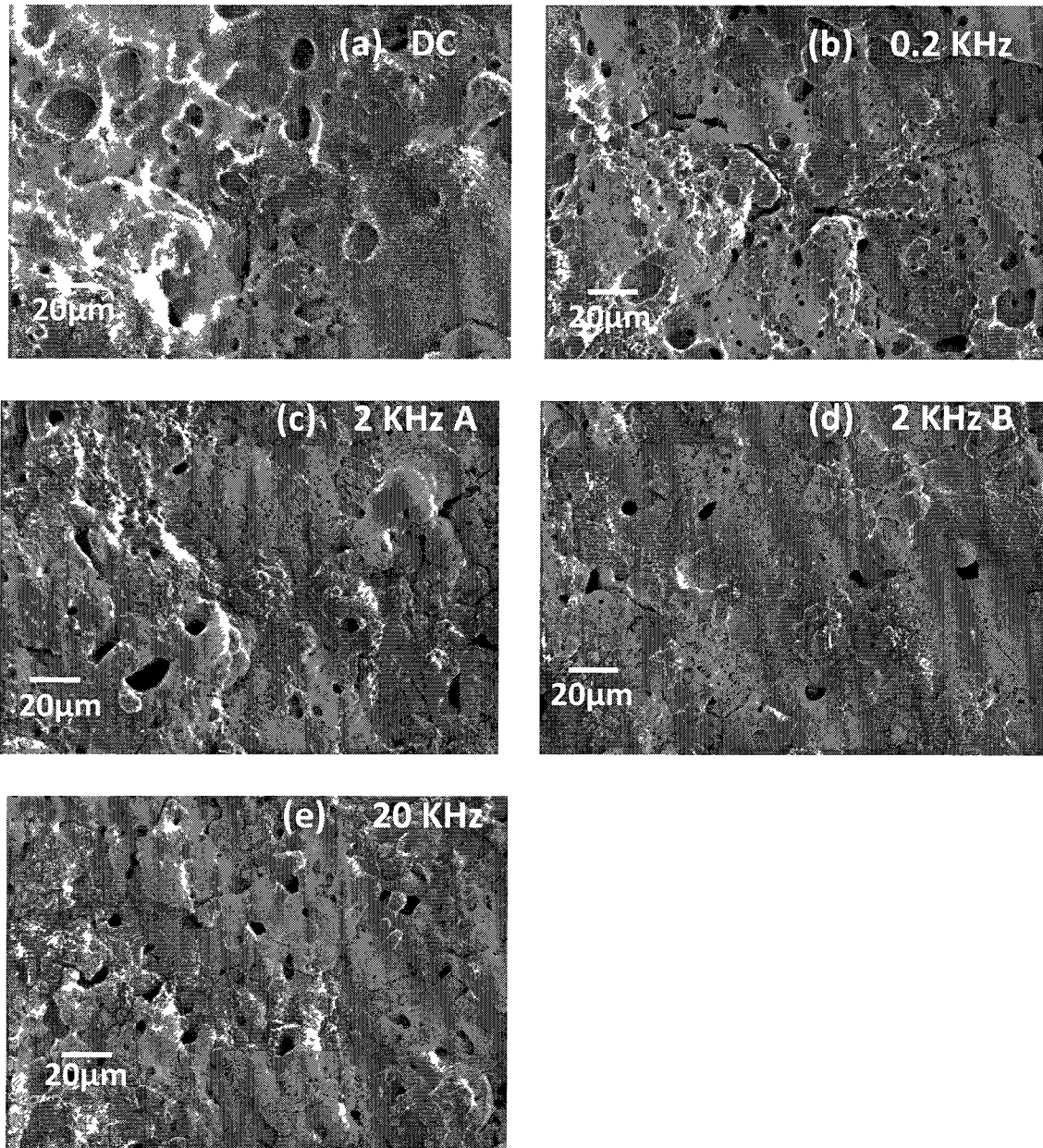
Figure 6.9 SEM micrographs of surface morphology of the coated Al sample, for a 60 min treatment time and different current modes at a current density of 0.15 A/cm^2.

6.1.7 The effect of treatment time on the cross section

Figure 6.11 shows the cross-sections of PEO coatings on Al substrates for treatment times of 15 min. The oxide layers have thicknesses ranging 15 μm to 40 μm. The coating shows some porosity and holes are exist within the coating and near the oxide-metal interface for the DC current mode Figure 6.10(a), the thickness of the oxide layer is

larger than all other cases. For the low frequency 0.2 KHz results shown in Figure 6.10(b), the porosity is high, the thickness of the oxide layer is less than that for the DC case. The 2 KHz A, and B cases have similar coating thickness as well as similar tends. However, the coating layer for the 20 KHz case is relatively thin, with some porosity, and has an irregular coating interface.
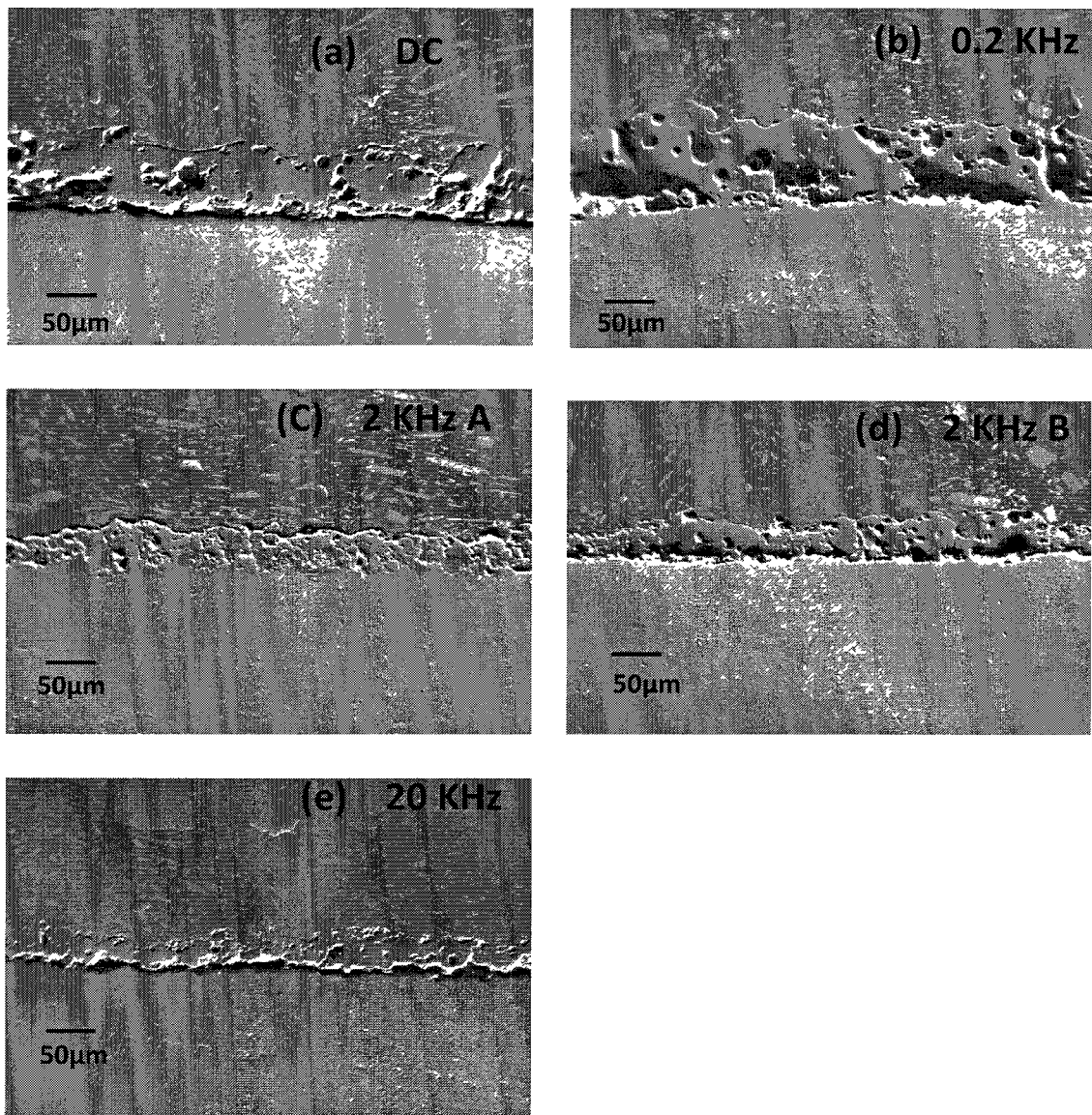
Figure 6.10 Cross-section micrographs of the oxide ceramic surface layers for 60 min treatment time at different current modes at a current density of 0.15 A/cm^2.
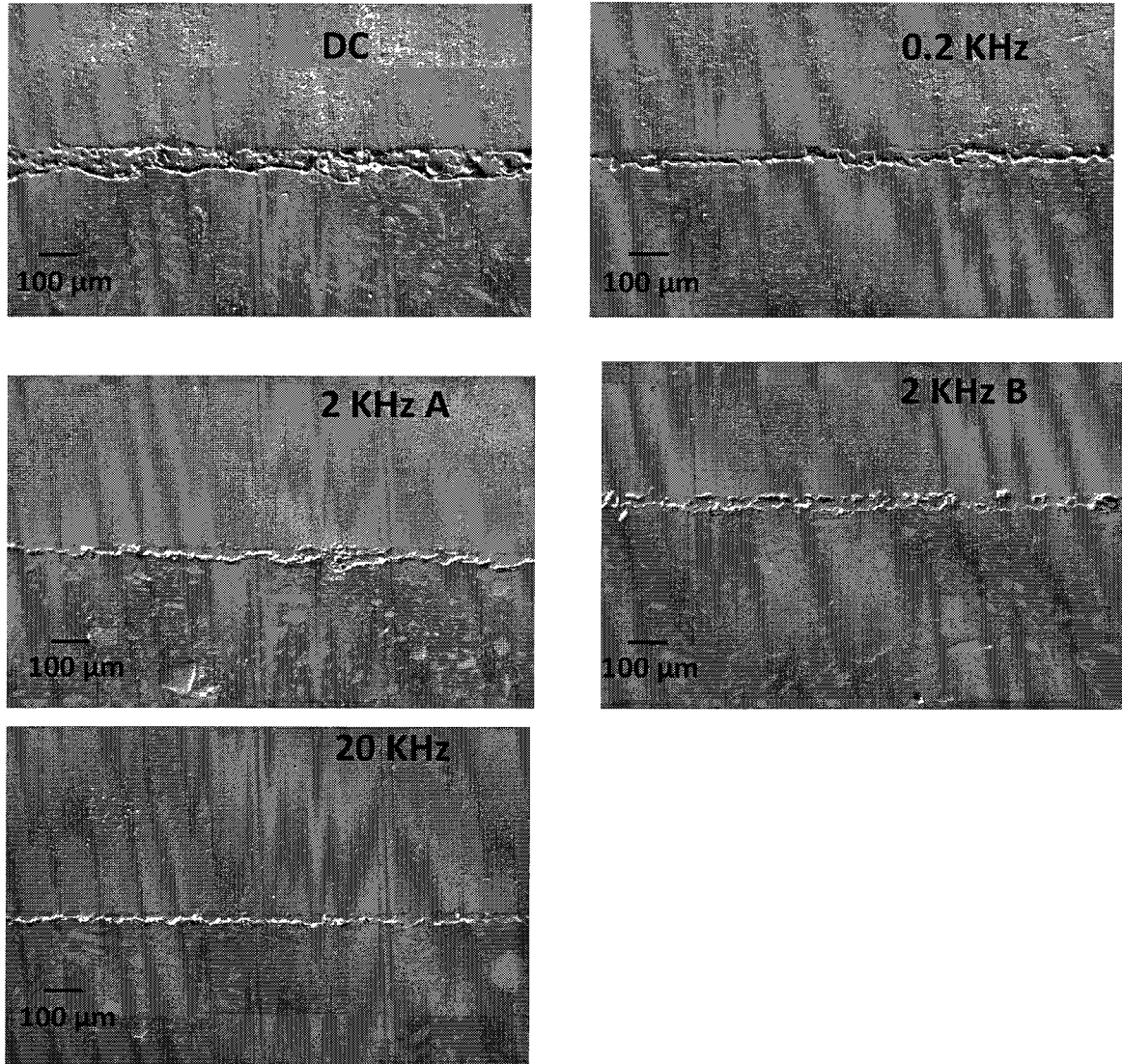
Figure 6.11 Cross-section micrographs of the oxide ceramic surface layers form for 60 min treatment time at different current modes at a current density of 0.15 A/cm^2.

6.2 Effect of plasma discharge behavior on coatings.

The coating surface morphology and cross-sectional microstructure can be linked to the plasma discharging behaviors. As it was mentioned earlier, one of our main concerns is the substrate/coating interface, where the B-type discharge is initiated, since usually the smoother this interface, the better the coating. The porosity (dark color) near this

interface results from the trapped gas and solidification shrinkage between the substrate and the oxide layer. During the strong discharges, gases which are mainly due to decomposition of the previously formed Al oxide, may re-react with Al and escape from, or be trapped in, the interface area. For simplified cases, where the possibility of gas escape or trapping in the interface zone is considered, a longer strong discharging (a wider Te peak in Figure 6.7) would cause a better sintering and thus a denser coating. Therefore for the coating produced with DC current, which has a longer sintering time due to its longer period (width) of B-type discharge profile (Figure 6.7(a), oxygen may have a better chance to be removed by re-reaction or escape, and as a result, the porous region in the interface area is relatively thin, Figure 6.10(a). The coating thickness for this case is large which is expected, due to the continuous power provided to the sample. However large porous areas and large discharge channels through the coating were present, due to the high current density $0.15A/cm^2$ for the 80% T_{on} time cases which causes strong B-type discharge. Those electrical parameters were chosen in this work to exaggerate the effect of B- type discharge on the coating morphology. It should be noted that the defects shown near the interfacial areas are due to the porosity (less density) and over-polishing artificial effects, and the coatings are not separated from the substrates. By reducing the current density, better and denser interfaces can be produced. However, previous work [46,50] also observed some porous areas near the interface of MgO and Al_2O_3 coatings on Mg and Al substrates using transmission electron microscopy (TEM) [50,93]. The Al_2O_3 coating was however demonstrated to have superior mechanical and wear properties [93]. For the low frequency of 0.2 KHz, the cross-section results showed a large number of discharge channels, a thick coating, and a porous area near the surface/coating interface. These features could be associated with the low frequency mode as in Figure 6.10(b), where strong discharging initiated at the interface but also where it was difficult for the oxygen gas to escape from the interface regions, due to a shorter sintering time available as indicated by the width of B-type discharge peaks in Figure 6.7(b) of the plasma temperature profile. The coating produced by UPDC at 2 KHz A exhibits a more homogeneous morphology than that formed at the DC and 0.2 KHz, Figure 6.10(c) where the effect of B type discharge is at its minimum compared with the other cases. The coating cross-section in Figure 6.10(c) illustrates that the

surface/coating interface is smooth and exhibits less porosity. For the 2 KHz B the coating becomes thinner as is clearly shown in Figure 6.10(d), where the coating thickness is smaller than the case of low frequency but higher than the high frequency case. Similar trends were also seen for the porosity. Figure 6.10(e) indicates that 20 KHz would significantly reduce the coating thickness, which is in consistent with earlier results reported by Yerokhin et al [21]. Although the temperature of B type discharge is high for this case, the duration time of all discharges is short, resulting in a low rate of the coating growth. Therefore, the coating thickness is thin compared to the other cases. The cross-section result shows a porous area as well as some discharge channels, again due to the strong B-type discharging with a short sintering time.

Therefore, the discharge behavior influences the microstructure and the morphology of the oxide coating. Since the B-type discharge is the strongest, it has the strongest effect on the surface morphology. This work also suggests that the strong B-type discharging can be controlled by adjusting T_{on}/T_{off} ratio but not by increasing the pulse frequency up to 20 KHz. On the other hand, a bipolar pulse DC mode can also be used to reduce the B type discharging as can be seen in the following sections.

6.3 Influence of Bipolar current mode on electrolytic plasma discharging behavior and aluminum oxide coating microstructure

In order to obtain better coatinggs and an enhance process efficiency, the bipolar (BPDC) current mode were used. In this section, a plasma electrolytic oxidation process (PEO) was used to produce oxide coatings on commercially pure aluminum (Al 1100) at two different current modes, pulsed unipolar and bipolar modes. The coatings were prepared in an alkaline electrolyte containing sodium silicates (7 g/l Na_2SiO_3) and potassium hydroxide (1 g/l KOH) added to balance the pH at 12. The processing parameters for the coated Al samples are listed in Table 6.2. It was found that the plasma discharge behavior significantly influenced the microstructure and the morphology of the oxide coatings. The main effect came from the strongest discharges which were initiated at the interface between the substrate and the coating. Through manipulation of process parameters to control or reduce the strongest discharge, the density and quality of the coating layers could be modified. By adjusting the ratio of the positive to negative pulse

currents as well as their timing in order to eliminate the strongest discharges, the quality of the coatings could be considerably improved.

Sample	Current mode	Time (min)	I^+ (A)	I^- (A)	T_{on}^+ (μs)	T_{off}^+ (μs)	T_{on}^- (μs)	T_{off}^- (μs)	C_R
S1	Unipolar	60	1.5		400	100			
S2	bipolar	60	2.0	1.0	400	100	500	100	1.14
S3	bipolar	60	2.0	1.5	400	100	400	100	0.89
S4	bipolar	90	2.0	1.5	400	100	600	100	0.66

Table 6.2 PEO Process parameters for coating depositions on Al.

Contrary to a unipolar current operating mode, the application of bipolar current pulse regimes usually offer better control over plasma chemical processes at both coating/metal interface and coating/electrolyte interface as well as improve the coating growth rate [21]. In the recently published work on PEO coatings, the pulsed bipolar current mode has been widely used [48,94-95]. However, an attempt has been made to better understand the effect of current modes on the plasma parameters and the coating properties. The optical emission spectra were recorded and plasma temperature profile versus processing time was constructed. The discharge behavior in the PEO process was studied with an emphasis on its impact on formation of coating surface layers.

6.3.1 Plasma electron temperatures

The temperature results of experiments carried out at various pulse duration time, with different currents passed through the sample surface during positive and negative biasing, are presented in Figure 6.12. It can be seen that the temperatures measured are in the range of 4000 - 7000 K for the unipolar case and in the range 4000 - 5500 K for bipolar case. The low temperature range (~4000 K) corresponds to the early stage discharges. After that, for the bipolar cases, Figure 6.11(b, c and d), average temperatures (base line temperature) for all cases increased reaching a maximum value in the range of

81

5100 K to 5400 K in less than 20 min, which is believed to correspond to the small discharges, A and C.

Figure 6.12(a) shows the plasma temperature profile for the unipolar current mode (S1), where the temperature increased from 4000 K to around 5500 K within 12 min, then the curve started to show many peak spikes ranging from 5000-7000 K. These spikes corresponded to B-type discharges, whereas the base line average is at ~5500 K. Therefore, the T_e profile depends strongly on the type of discharge. For the case of S2, the temperature increased to around 5500 K within 15 min after the start of the process, and then the average base temperature decreased to about 4800 K as can be seen from Figure 6.12(b). The spikes on this curve were smaller than those for the unipolar and the temperature barely exceeded the 5800 K range, which was believed due to the reduction of the strong B-type discharges. This result is comparable with S3 results shown in Figure 6.12(c), where the spike temperatures are reduced significantly; the maximum temperature was also reduced to 5200 K, which may be attributed to the negative current phase as well as the timing of the off time of the pulses. Figure 6.12(d) shows the temperature result for S4 case, where the sample was treated for 90 min at C_R=0.66. The average base temperature for this case remained around 4900 K after reaching a maximum of 5300 K. However, a spike fluctuation started to appear at 50 min of the treatment time, which may be attributed to the fact that discharge size increased with process time. However, these peaks were shorter and fewer than that of the S1 sample of the unipolar current mode. Therefore, by using a bipolar current mode and reducing the C_R ratio, the average temperature was slightly reduced and strong temperature spikes (fluctuations) could be suppressed or start to appear at later times.

Since the B-type discharge was the strongest, it would have the highest effect on the plasma temperature and hence on the surface morphology and coating microstructure. The competition between the current phases (positive and negative phases) from one side and the pulse timing from the other side can have a significant influence on the discharging procedure of the PEO process.
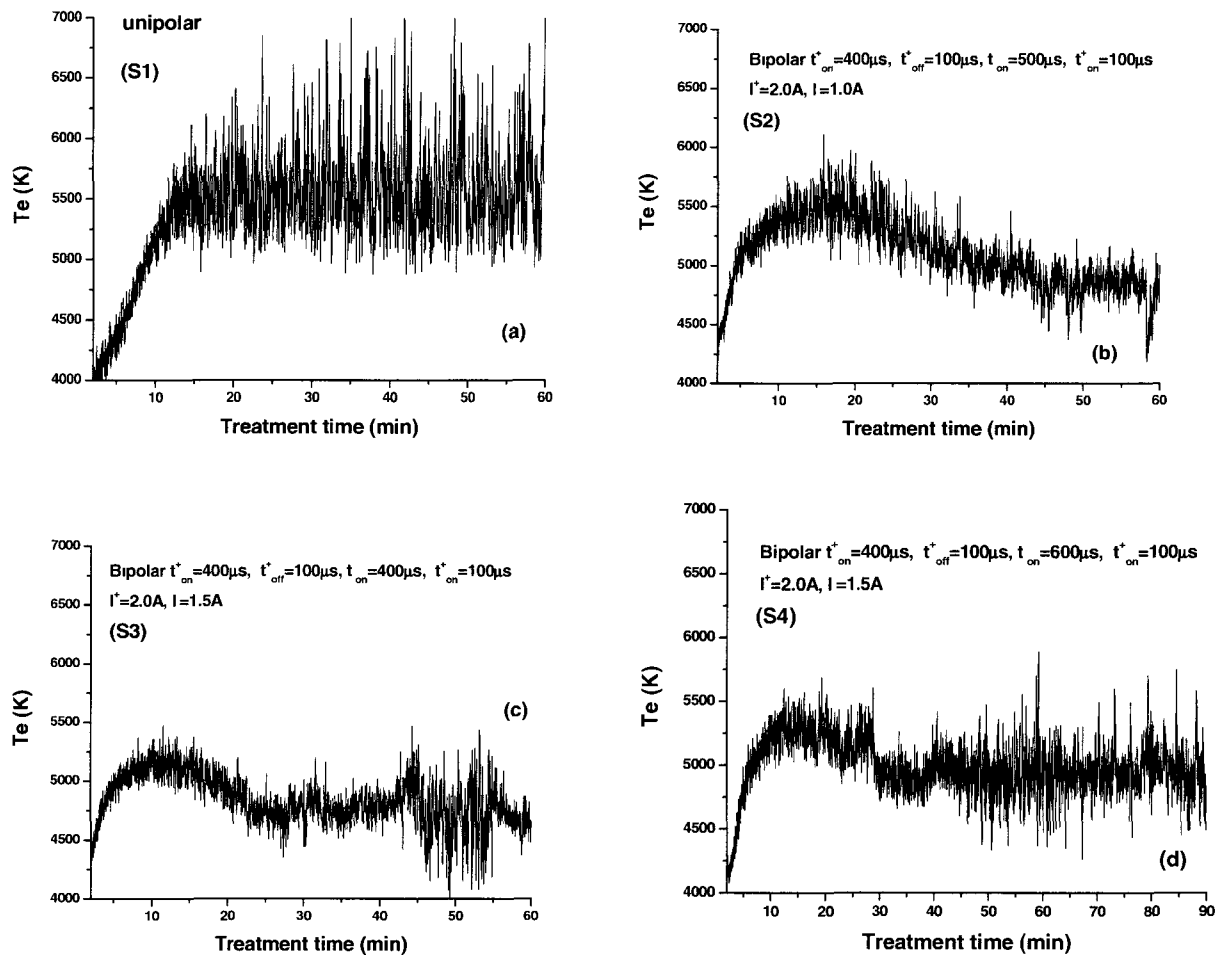
Figure 6.12 Plasma temperature as a function of treatment time (min) determined from the intensity ratio of Al (396.1 nm)/Al(309.2 nm), for the samples S1 (at unipolar current mode), and S2-S4 for the bipolar current mode.

6.3.2 Surface morphology

The surface morphologies of the Al 1100 specimens treated by the PEO process are shown in Figure 6.13. All samples showed a large number of 'pancake' like features and discharge pores were randomly arranged on the coating surface, which is a common characteristic of PEO coatings. At the center of each pancake was a discharge channel through which the molten aluminum surged out of the channel and quickly solidified

leaving distinct boundaries that define each pancake. The molten oxides around the pores indicate that the instantaneous temperature in the micro discharge zone might reach several thousand degrees [20]. Figure 6.13(a) is a SEM micrograph of the coated sample S1 prepared with the unipolar current mode and showed a number of pancake features and pores in the coating. Pores of different size ranges (10-30 μm) are evident on the surface. The relatively large holes in the center of the pancake suggested that there were strong discharges (B- type) and such holes might penetrate deeply in the coating thickness. Some micro cracks appeared on the coating surface, which could result from the thermal stress during the fast solidification of the molten oxide product in the strong discharge channel [96].

In specimens S2-S4 processed using a bipolar current mode, Figure 6.13 (c-h), the pore population was reduced and the size of the pores was smaller being in the range of 10 μm. Such morphology was expected since the number and strength of the strong B-type discharges were reduced by using the bipolar current mode, mainly due to the negative part as well as the off time of the pulses. Compared to sample S2, by raising the negative current density (Table 6.2), sample S3 showed an increase of the volcano-like eruptions which added more irregularity to the surface morphology. But at the same time the coating thickness of these samples is larger than that of sample S2 by about 20 μm. The coating produced using a bipolar current mode was more compact and less porous meanwhile; the coating obtained at unipolar current mode S1 had a higher degree of porosity. To study the effects of the longer treatment time, sample S4 shows the surface morphology of the oxide coating treated for 90 min at C_R=0.66. Figure 6.13(g) and (h) shows some holes formed due to volcano-like eruptions which would likely occur at the late stage of the long process time. Therefore the current phases and values together with the pulses timing can have significant influence on the coating morphology.
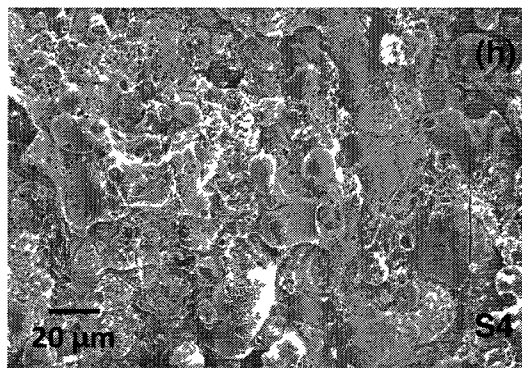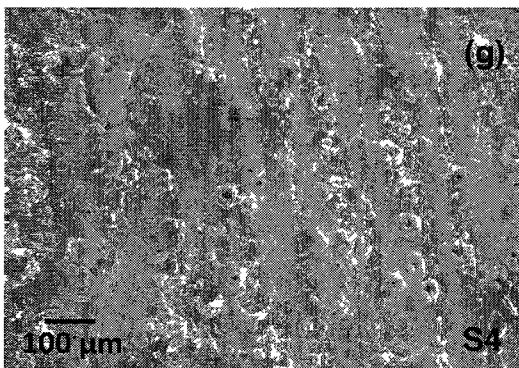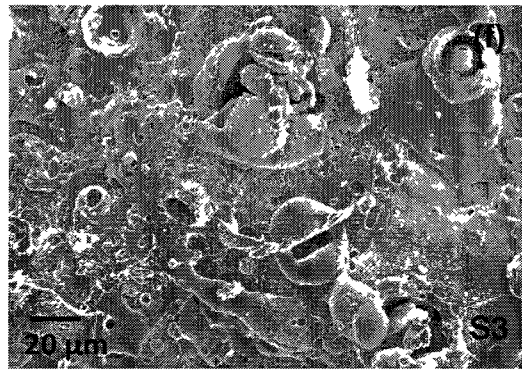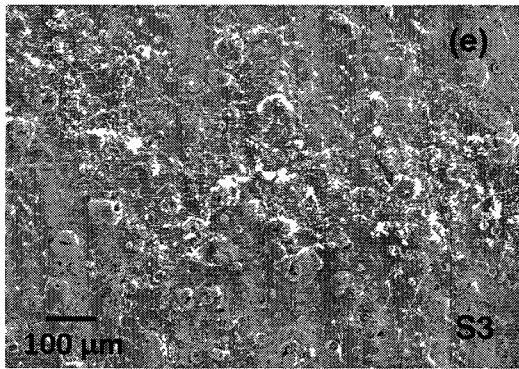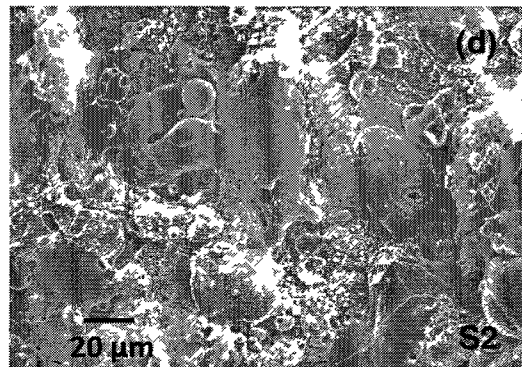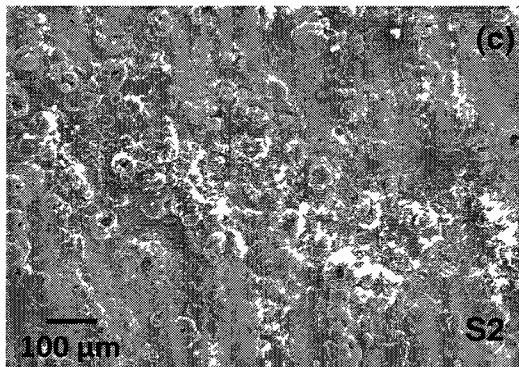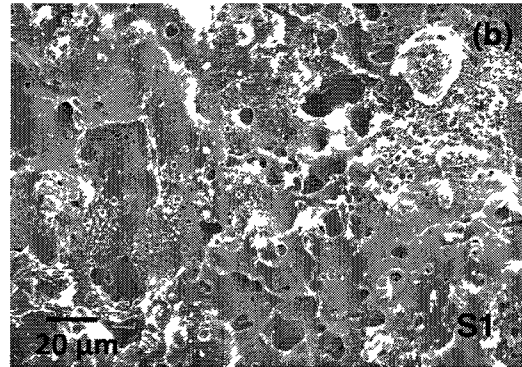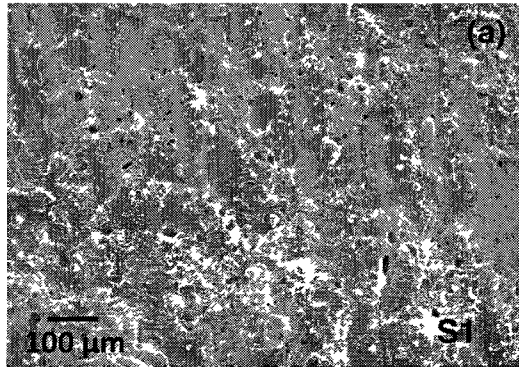
Figure 6.13 SEM micrographs showing surface morphology of oxide coating on Al for: (a) S1 at unipolar and (b) S2-S4 bipolar current modes.

6.3.3 Cross-sectional structure of the coatings

SEM observations were conducted on polished cross-sections of the Al samples, mounted in Bakelite resin. Scanning electron micrographs showing the cross-sections of the PEO coated Al samples for two different current modes are presented in Figure 6.14. The SEM cross-section images indicate that the coating is composed of three distinct layers. There is an outer loose region where pores and defects caused by the most recent discharges are the dominant features of this layer. The inner layer (γ-Al_2O_3 and α-Al_2O_3) [53] may be subdivided into porous inner layer and dense inner layer. The third layer is the diffusion layer that is located at the coating/substrate interface as is readily seen on samples S3 and S4. Figure 6.14(a) and (b) shows the cross section of the ceramic coating S1 at the unipolar current mode. The coating appeared to have a significant amount of connected porosity, holes and other structure defects within the coating and near the coating/substrate interface. The coating thickness after the 60 min treatment time, range from 60-90 μm at different locations of the cross section, and the loose layer comprised 40-50% or so of the total thickness. Such defects and porosity were likely caused by the strong B- type discharges. The high temperature generated by strong discharges melted the oxide and then some gases likely were trapped in the interface layer between the substrate and the coating. As previously reported [47], during PEO coating formation, the porosity was formed as a result of localized oxygen trap in molten aluminum in the vicinity of electric discharges at such area.

One of major concerns is the substrate/coating interface, where the very strong B-type discharge is initiated, The main effect of the bipolar current mode is a discharge disturbance, which averts the development of long lived, very large microdischarges. By using the bipolar current mode there will be a balance of the discharge effect. The T_{off} duration should be long enough for the local molten oxide to be cool down before another pulse were initiated, while the T_{on} provided time long enough for sintering and therefore thick and hard coating with minimum pores will be produced. The coating cross-section of samples S2-S4 in Figure 6.14(c-h) obtained at the pulsed bipolar current mode (Table

6.2) illustrated that the surface/coating interface was smooth and almost free from porosity and defects. Figure 6.14(c) and (d)) shows the oxide coating on sample S2 having thickness about 65-75 μm with very thin loose layer. Although the upper inner layer showed some disconnected pores as well as tiny micro cracks, the lower inner layer appeared to be smooth with minimum porosities.
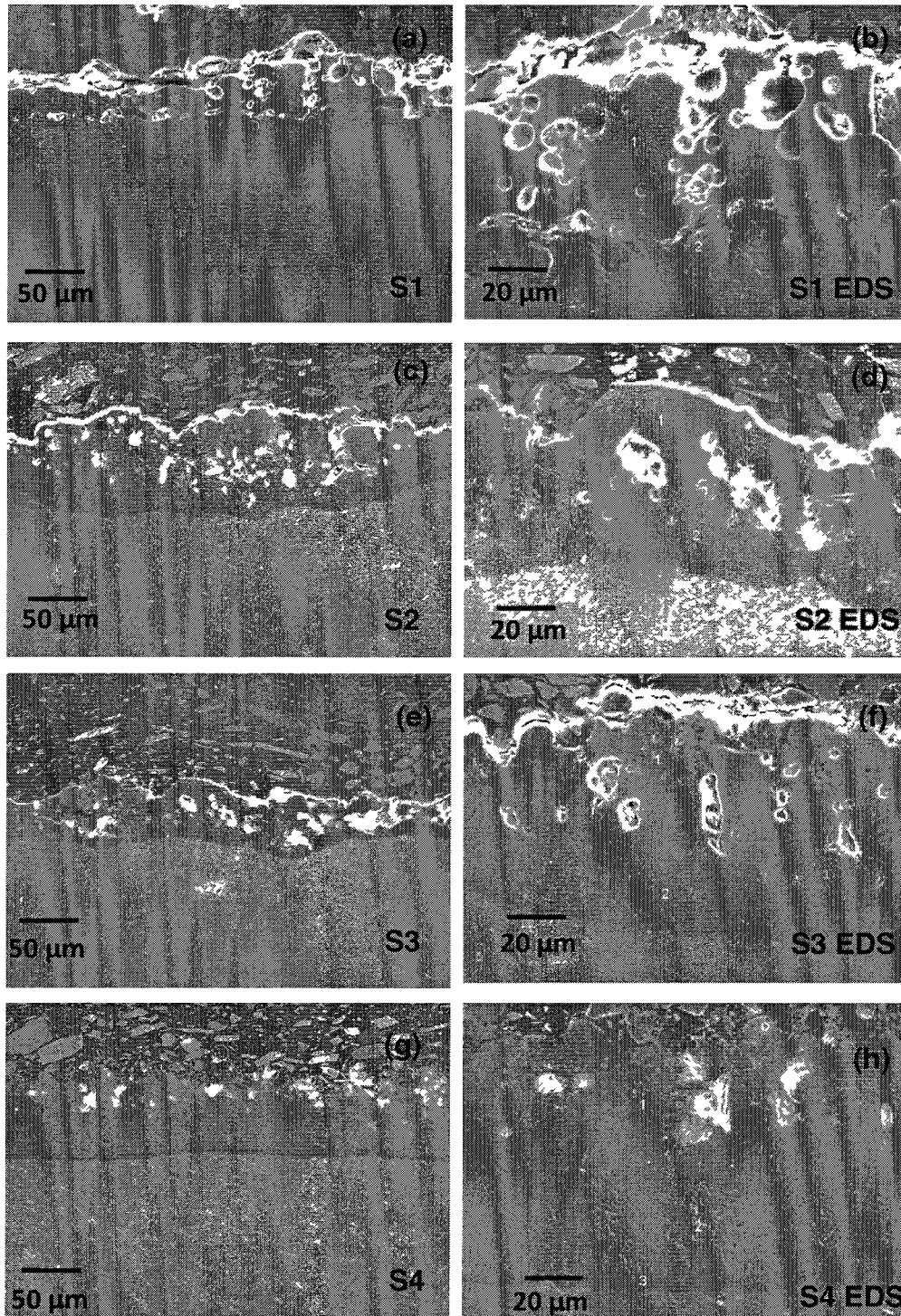
Figure 6.14 SEM micrographs of cross-sections of coatings on Al using: (a) S1 at unipolar and (b) S2-S4 bipolar current modes.

Compared to the sample S2, the sample S3 showed a thicker coating with relatively less porosity in the inner layer, Figure 6.14(e) and (f). The thickness of the oxide layer was in the range of 80-105 μm, and the ratio of outer loose layer thickness over the total coating thickness was less than that of S2 sample. As mentioned previously, the sample S4 was prepared with 90 min treatment to study the effect of longer treatment time on both the surface morphology and the coating growth rate. Figure 6.14(g) and (h) show a cross-section of the ceramic coating S4 with coating thickness about 120-130 μm. The outer loose layer was actually thinner compared to that of other samples. The upper part of the inner layer showed some isolated pores. Curran et al [47] point out that the micro pore initiation through the coating may facilitate the formation of relatively thick coating, by allowing electrolyte to penetrate deep into the growing layer during the process. Alternatively, the pores may become gas filled. This would again provide a lower resistance path. The thickness of the diffusion layer shown by the dark layer in Figure 6.14(h) seems to be about 7 μm and the layer showed a good adherence to the substrate surface.

Figure 6.15 shows the EDS results of the coatings at different positions 1 and 2. It is common that in the outer region, the silicon content is much higher than that in the inner region. That may be attributed to voids and pores in the coatings which can trap the silicate electrolyte and allow silica to be formed after the plasma discharging. By comparing the Si peaks in Figures 6.15(a) and (b) for the unipolar current mode (S1) with those of the bipolar current modes (S2-S4) in Figure 6.15(c-d), it was noted that higher Si contents existed in coating S1 in the outer region compared to coatings S2-S4, due to higher porosity and defect levels in S1. The inner layer barely contains any elements from the electrolyte. The source of the Au signal in the EDS was from the sputtered thin film deposited before SEM observations. Aluminum and oxygen are the two major constituents of the inner layer of the coatings.
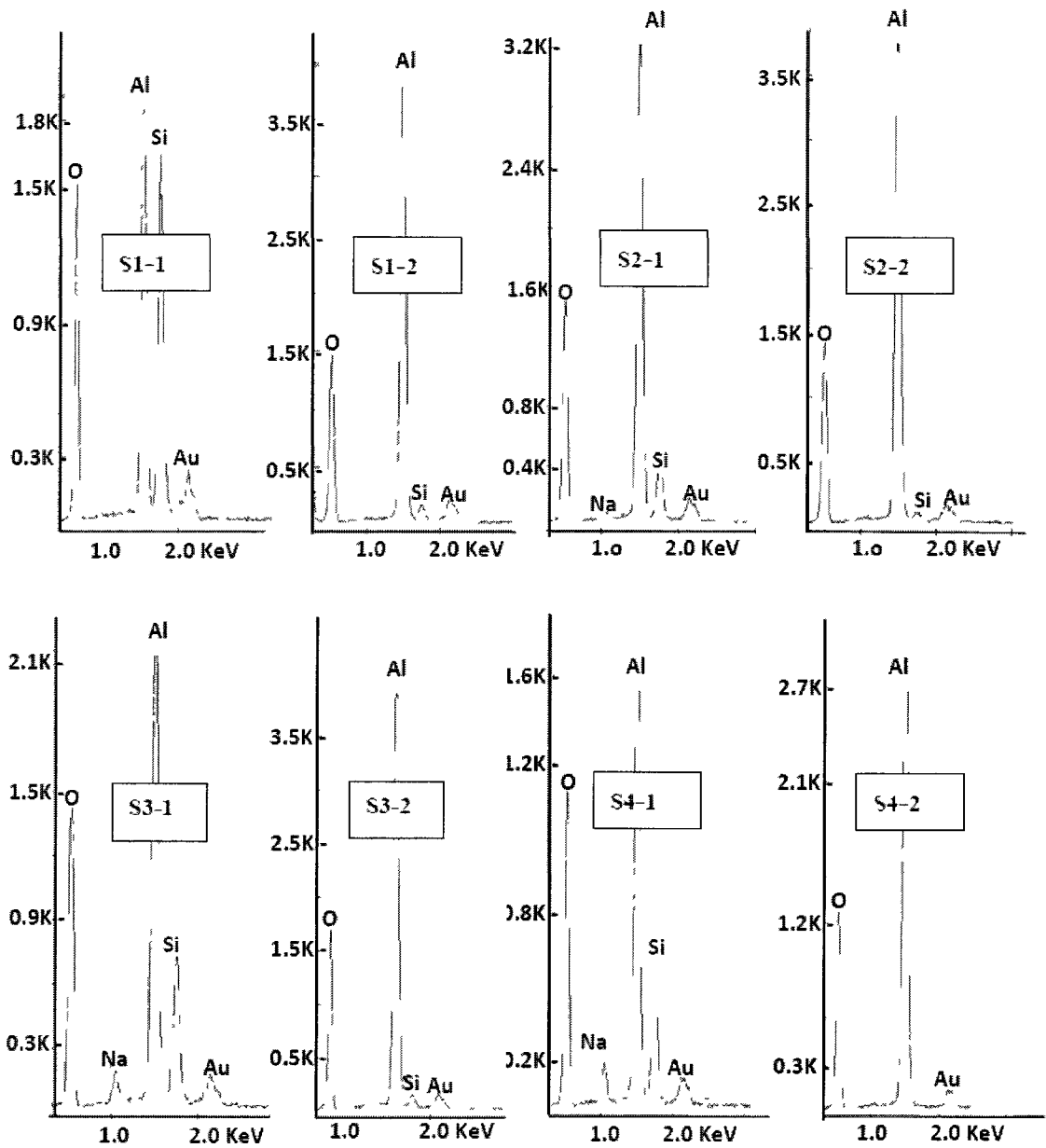
Figure 6.15 EDX analysis from different regions of the coated Al samples using: (a) S1 at unipolar and (b) S2-S4 bipolar current modes.

6.3.4 Corrosion properties of the Coatings

The potentiodynamic polarization curves of the uncoated AL100 Al alloy (curve 1) and the PEO coated specimens using either unipolar or bipolar current modes (curves 2 and 3 respectively) are shown in Fig. 6.16. The corrosion potentials, corrosion current density, and anodic/cathodic Tafel slopes β_a and β_c were derived from the test data. Based on the approximately linear polarization at the corrosion potential (E_{corr}), the polarization resistance (R_p) was determined from [3.].

A summary of the results of the potentiodynamic corrosion test in a 3.5% NaCl solution is given in Table 6.3. The data clearly show the enhanced corrosion resistance afforded by the coatings.

In contrast to the uncoated aluminum alloy Al100, the samples with PEO coatings all had lower corrosion current densities and almost similar corrosion potentials. By changing the current mode from unipolar to bipolar mode, the corrosion current density for the coated samples decreased from 2.55 $\mu A/cm^2$ to 0.11 $\mu A/cm^2$.

Table 6.3 Potentiodynamic polarization corrosion test results in3.5%wt NaCl solution

Samples	E_{corr} mV	I_{corr} $\mu A/cm^2$	β_a V/decade	β_c V/decade	R_p Ω/cm^2
Uncoated Al (S1)	-667.8	7.63	54.9	230.8	$2.53 \times 10^{+6}$
Unipolar coated (S2)	-666.5	2.55	118.2	420.0	$15.73 \times 10^{+6}$
Bipolar coated (S3)	-665.3	0.11	68.0	254.7	$212.14 \times 10^{+6}$

Since the bipolar current mode produce a thicker and hard coating, sample S3 shows a higher polarization resistance of $212.1 \times 10^{+6}$ Ω and lower corrosion current density than sample S2 coated by unipolar current mode, with a polarization resistance of $15.7 \times 10^{+06}$ Ω and higher corrosion current density.
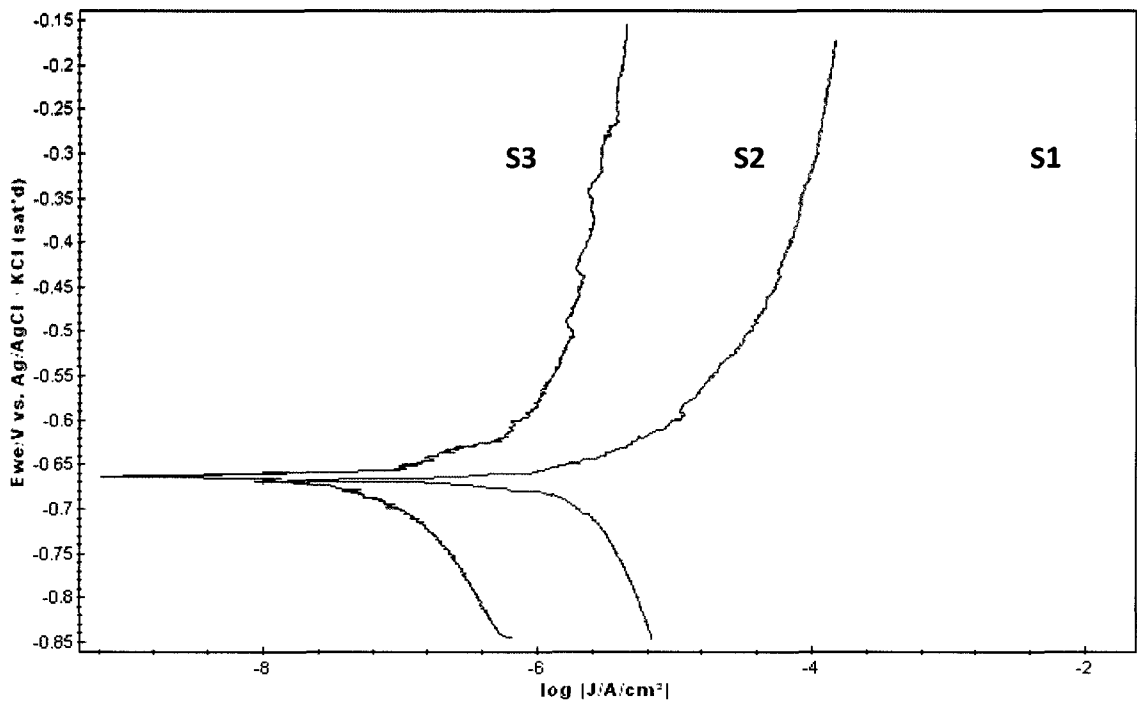
Figure 6.16 Potentiodynamic polarization curves of the uncoated (curve S1) and coated samples using unipolar (curve S2) and bipolar (curve S3) current modes.

Since the corrosion resistance of the uncoated 1100 Al alloy is high $(2.53 \times 10^{+06} \ \Omega)$, therefore the naturally formed protective aluminum hydroxide film on the Al substrate surface can not be easily dissolved during the corrosion process.

It may be expected that the thicker coating gives rise to better resistance to localized damage, however as the defect level in the unipolar sample coating was quite significant, the sample S2 has registered a lower breakdown potential compared to sample S3. The corrosion resistance of the coated samples was improved by using a bipolar current mode since a less porous and more compact structure was formed. The properties of the plasma discharges themselves in the bipolar current mode differ from those of the unipolar one. An increase of the A and C discharge types and decrease of strong discharges moving over the surface being oxidized, have a significant effect on the coating properties, where a dense coating morphology could be achieved by adjusting positive to negative current

ratio and their timing to eliminate or reduce the strongest plasma discharges and thus the high temperature spikes.

6.4 Discussion

The coating surface morphology and cross-sectional microstructure can be linked to the plasma discharging behavior. Figure 6.17 shows a schematic diagram of the discharge models for the PEO process for an Al sample and the influence of such discharges on the T_e profile as well as on the coating microstructure. As it was mentioned in previous sections, the high temperature spikes corresponded to the strongest discharges (B-type discharge) and they significantly affected the microstructure and morphology of the coating. The strongest discharges would make the coating more porous. The strongest discharges can be reduced or eliminated by appropriately adjusting the bipolar current and the on and off time interval of the pulses. By elimination of very strong B-type discharges, the high temperature spikes were reduced and the plasma average temperature was also decreased to some extent. Such B-type discharge elimination facilitated the coating inner layer to have denser microstructures with less porosity. Prepared at the bipolar current mode, the ceramic coating could have a thick dense inner layer and a thin outer porous layer as can be seen in Figure 6.14. Therefore the values of the current phases together with the pulses timing can have a significant influence on the morphology of surface and cross-sections and density of the coatings. Through manipulation of process parameters to control or reduce the strongest B-type discharge in the PEO process, the density and quality of the coating layers could be modified.
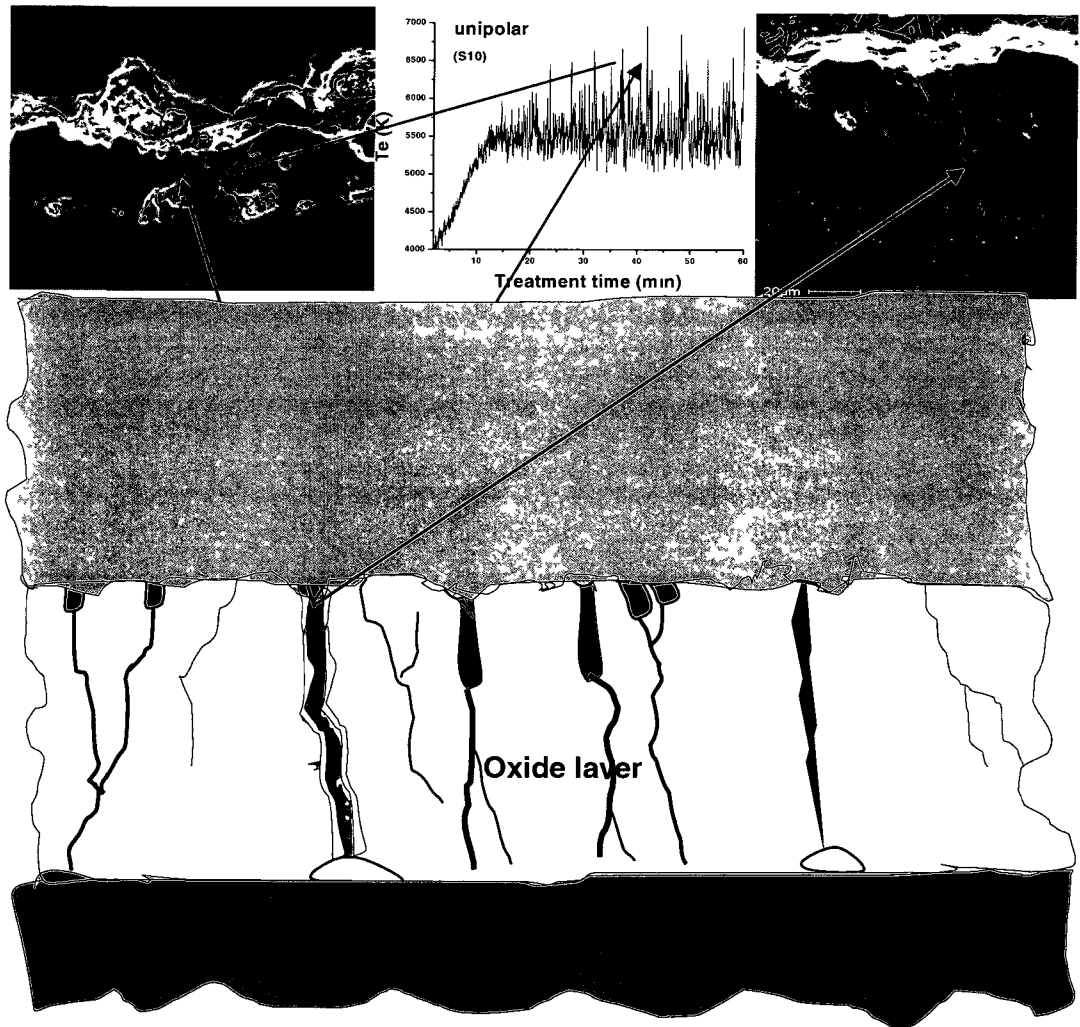
Figure 6.17 Schematic diagram of the discharge model showing the influence of B-type discharges on plasma temperature profile and on the cross section of the oxide coating.

CHAPTER 7 CONCLUSIONS AND FUTURE WORK

7.1. Conclusions

1- The measurement and analysis of visible and NUV wavelength emissions from plasmas using OES provides a valuable diagnostic tool for the study of the PEO process. From answering relatively simple questions such as what ions compose the plasma and when they appear during the discharge, to issues such as electron temperature, and electron concentration, the analysis of the visible and NUV wavelength spectra collected from the PEO plasma using OES provides valuable insights into understanding the processes in the PEO plasma.

2- The plasma concentration was successfully calculated from Stark broadening of the H_β line $(1.5 \pm 0.23) \times 10^{22}$ m^{-3} to $(2.4 \pm 0.36) \times 10^{22}$ m^{-3} for the PEO at a current density of 0.15 A/cm^2. Plasma electron temperatures were determined by the line intensity ratios and were found to be in the range of 4500 ± 450 K to 10000 ± 1000 K. This may be the first time that a complete electron temperature profile for the whole coating period has been obtained and linked with the collective discharge behavior.

3- Based on the locations of discharging intensities, three plasma discharge types have been proposed: metal-oxide interface discharge type (B) and oxide-electrolyte interface discharge types within the coating upper layer (A) and at the coating top layer (C). The discharge behavior within the PEO coating and on the coating surface was responsible for the profiles of plasma concentration and temperature, as well as the coating surface morphologies. The study has provided connections between plasma discharge behavior and plasma electron temperature profile as well as coating surface morphology.

4- Five different PEO processing methods were carried out in silicate electrolytes to produce oxide coating on an Al alloy substrate. High temperature spikes corresponding to the strong discharges (B-type discharge), were initiated at the sample coating interface. These temperature spikes significantly affected the microstructure and morphology of the coating, as can be seen by changing the current mode form DC to pulsed unipolar DC at

different frequencies. The strong discharges can be eliminated by appropriately adjusting the unipolar DC current on and off time interval, but a change in pulse frequency (up to 20 KHz) had little effect in controlling the strong discharging. The unipolar mode for the intermediate frequencies in the range of 2-3 KHz can improve the coating quality compared with the DC mode, both in terms of surface morphology and cross- section structure.

5- Two different current modes during the PEO processes in silicate electrolytes were used to produce oxide coatings on an Al substrate. Compared to the unipolar current process, the application of pulsed bipolar current resulted in reducing the high spikes on temperature profiles and the average plasma temperature.

6- The aluminum oxide coating morphology, microstructure and corrosion reistance were also significantly different under different current operating modes. The bipolar current mode could improve the coating quality compared with the unipolar current mode, in terms of surface morphology, cross-sectional microstructure and corrosion resistance. A dense coating morphology could be achieved by adjusting positive to negative current ratio and their timing to eliminate or reduce the strongest plasma discharges and thus the high temperature spikes. Therefore, this work showed that by appropriately controlling the ratio of the positive to negative pulse currents as well as their timing, the very strong plasma discharges and the resulted high temperature spikes could be eliminated and hence the quality of the coatings was considerably improved.

7.2 Future Work

Based on this study, the following suggestions are made for future work:

1. Extend the process parameters beyond the range in the present study in order to further understand the relationship between discharges, porosity, thickness and corrosion resistance.

2. Apply the same OES procedure to the PEO process for different metallic substrates to support the discharge model.

3. Furthermore research is needed in order to better understand the influence of the discharge modes on the coating growth rates and mechanisms at the difference stages.

4. Determine whether the OES technique can be used to "control" the process parameters in PEO Coating.

5. Additionally, more research needs to be conducted to reduce the strong discharge (type B) by adjusting the process parameters.

References

[1]   C. Blawert, N. Hort and K. Kainer, "Automotive applications of magnesium and its alloys" (2004) Trans Indian Inst Met **57**(4): p.397–408.

[2]   H. Friedrich and S. Schumann "Research for a ''new age of magnesium in the automotive industry" (2001) Journal of Materials Processing Technology **117**: p. 276–281.

[3]   J.J. Michalek, P.Y. Papalambros and S.J. Skerlos "A study of fuel efficiency and emission policy impact on optimal vehicle design decisions" (2004) J Mech Des **126**(6): p.1062–1070.

[4]   H. Dieringa and K.U. Kainer, "Magnesium – der Zukunftswerkstoff für die Automobilindustrie" (2007) Materialwissenschaft und Werkstofftechnik **38**(2): p. 91–95.

[5]   E. Aghion, B. Bronfin, D. Eliezer, "The role of the magnesium industry in protecting the environment" (2001) Journal of Materials Processing Technology" **117**(3): p. 381–385.

[6]   Y. Sun, "Thermally oxidised titanium coating on aluminium alloy for enhanced corrosion resistance" (2004) Materials Letters **58**: p. 2635-2639.

[7]   X. Zhang, S. Lo Russo, S. Zandolin, A. Miotello, E. Cattaruzza and P.L. Bonora, "The pitting behavior of Al-3103 implanted with molybdenum" (2001) Corrosion Science **43**: p. 85-97.

[8]   P. Preston, R. Smith, A. Buchanan and J. Williams," Characterization of blister formation and pitting of tungsten ion implanted aluminum" (1995) Scripta Metallurgica et Materialia **32**: p. 2015-2020.

[9]   M. Sheffer, A. Groysman and D. Mandler, "Electrodeposition of sol–gel films on Al for corrosion protection" (2003) Corrosion Science **45**: p. 2893-2904.

[10] J. Masalski, J. Gluszek, J. Zabrzeski, K. Nitsch and P. Gluszek," Improvement in corrosion resistance of the 316l stainless steel by means of Al_2O_3 coatings deposited by the sol-gel method" (1999) Thin Solid films **349**(1-2): p. 186-190.

[11] J. Zhao, J. Xia, A. Sehgal, D. Lu, R. McCreery and G. Frankel," Effects of chromate and chromate conversion coatings on corrosion of aluminum alloy 2024-T3" (2001) Surface and Coatings Technology **140**: p. 51-57.

[12] A. L. Yerokhin, X. Nie, A. Leyland, A. Matthews and S. J. Dowey, "Plasma electrolysis for surface engineering" (1999) Surface and Coatings Technology **122**: p. 73-93.

[13]   L. O. Snizhko, A. L. Yerokhin, A. Pilkington, N. L. Gurevina, D. O. Misnyankina, A. Leyland and A. Matthews, Anodic processes in plasma electrolytic oxidation of aluminum in alkaline solutions (2004) Electrochimica Acta **49**: p. 2085-2095.

[14]   W. Xue, Z. Deng, R. Chen and T. Zhang," Growth regularity of ceramic coatings formed by microarc oxidation on Al]Cu]Mg alloy" (2000) Thin Solid Films **372**: p. 114-117.

[15]   F. Mécuson, T. Czerwiec, T. Belmonte, L. Dujardin, A. Viola and G. Henrion, "Diagnostics of an electrolytic microarc process for aluminum alloy oxidation" (2005) Surface and Coatings Technology **200**: p. 804-808.

[16]   A.V. Timoshenko and Y.V. Magurova," Investigation of plasma electrolytic oxidation processes of magnesium alloy MA2-1 under pulse polarization modes (2005) Surface and Coatings Technology **199**: p. 135-140.

[17]   H. Ryu, S. Hong, Corrosion Resistance and Antibacterial Properties of Ag-containing MAO coatings on AZ31 Magnesium Alloy Formed by Microarc Oxidation" (2010) Journal of Electrochemical Society, **157** (4): p. C131-C136.

[18]   X. Nie, X. Li, D. Northwood, Corrosion behavior of metallic materials in ethanol-gasoline alternative fuel cell (2007) Materials Science Forum, **546-549**: p. 1093-1100.

[19]   P. Zhang, X. Nie, D. Northwood," Influence of coating thickness on the galvanic corrosion properties of Mg oxide in an engine coolant" (2009) Surface and Coatings Technology **203**: p. 3271-3277.

[20]   C. S. Dunleavy, I. O. Golosnoy, J. A. Curran and T. W. Clyne," Characterisation of discharge events during plasma electrolytic oxidation" (2009) Surface and Coatings Technology **203**: p. 3410-3419.

[21]   A. L. Yerokhin, L. O. Snizhko, N. L. Gurevina, A. Leyland, A. Pilkington and A. Matthews, "Discharge characterization in plasma electrolytic oxidation of aluminum' (2003) J. Phys. D: Appl. Phys. **36**: p. 2110-2120.

[22]   M. D. Klapkiv, H. M. Nykyforchyn and V. M. Posuvailo, "Spectral analysis of an electrolytic plasma in the process of synthesis of aluminum oxide (1995) Mat. Sci. **30** [3]: p. 333-343.

[23]   F. Me´cuson, T. Czerwiec, G. Henrion, T. Belmonte, L. Dujardina, A. Viola, J Beauvir, " Tailored aluminum oxide layers by bipolar current adjustment in the Plasma Electrolytic Oxidation (PEO) process" (2007) Surface and Coatings Technology **201** : p. 8677-8682.

[24]   A. I. Maximov and A. V. Khlustova, Optical emission from plasma discharge in electrochemical systems applied for modification of material surfaces" (2007) Surface and Coatings Technology **201**: p. 8782-8788.

[25]   H. R. Griem, Plasma Spectroscopy (Cambridge: McGraw-Hill) (1964).

[26] B. Kasalica, M. Petkovic, I. Belca, S. Stojadinovic and Lj Zekovic, Electronic transitions during plasma electrolytic oxidation of aluminum (2009) Surface and Coatings Technology" **203** : p. 3000-3004.

[27] J. A. Curran and T. W. Clyne, Thermo-physical properties of plasma electrolytic oxide coatings on aluminum" (2005) Surface and Coatings Technology **199**: p. 168-176.

[28] G.A. Markov and G.V. Markova, USSR Patent 526961, Bulletin of Inventions, **32** (1976), 1

[29] A.V. Nikolaev, G.A. Markov and B.I. Peshchevitskij, (1977), Izv. SO AN SSSR. Ser. Khim. Nauk, **5**(12): p. 32.

[30] G.A. Markov, V.V. Tatarchuk and M.K. Mironova, (1983), Izv. SO AN SSSR. Ser. Khim. Nauk, **3**(7): p. 34.

[31] L.A. Snezhko, L.A. Beskrovnyj and Yu.M. Nevkrytyj V.I. Tchernenko, (1980) Zashch. Met., **16**(3): p. 365.

[32] L.A. Snezhko and G.A. Rozenboym, V.I Tchernenko, (1981), Zashch. Met., **17**(5): p. 618.

[33] L.A. Snezhko and V.I. Tchernenko, (1983), Elektron. Obrab. Mater., **2**: p. 25.

[34] L.A. Snezhko and V.I. Tchernenko, (1983), Elektron. Obrab. Mater., **4**: p. 38.

[35] V.I. Tchernrnko, L.A. Snezhko and C.B. Tchernova, (1984), Zashch., Met. **20**(3): p. 454.

[36] L.A. Snezhko, S.G. Pavlus and V.I. Tchernova, (1984), Zashch., Met. **20** (4): p. 292.

[37] G.A. Markov, M.k. Mironova, O.g. Potapova, (1983), Izv. AN SSSR. Ser. Neorgan. Mater., **19**(7): p. 1110

[38] A.A. Petrosyants, V.N. Malyshev,V.a. Fyedorov and G.A. Markov, (1984), Trenie Iznos, **5**(2): p. 350.

[39] V.N. Malyshev, S.I. Bulychev, G.A.Markov, V.A. Fyedorov, A.A. Petrosyants, V.V. Kudinov, M.H. Shorshorov and Fiz. Khim. Obrab. (1985), Mater. **1**: p. 82.

[40] V.A. Fyedorov, V.V. Belozerov, N.D. Velikosal'skaya, S.I. Bulychev and Fiz. Khim. Obrab. (1988), Materialov,**4** : p. 92.

[41] V.S. Rudnev, P.S. Gordienko, preprint no.3384-B87, Inst. Khimii DVO AN SSSR Vladivostok, 1987.

[42] P.S Gordienko, P.M. Nedozorov, L.M. Volkova, T.P. Yarovaya and O.A. Khrisanfova, "Phase composition of anodic films on NTsU alloy, formed at sparking potentials in aqueous electrolytes" (1989), Zashch. Met., **25**(1): p. 104-106.

[43] W. Krysmann, P. Kurze, K. Dittrich, H. Schneider, "Process Characteristics and Parameters of Anodic Oxidation by Spark Discharge (ANOF)" (1984), Cryst. Technol., **19** (7): p. 973-979.

[44] P. Kurze, W. Krysmann, J. Schreckenbach, Th. Schwarz and K. Rabending, "Coloured ANOF layers on aluminium" (1986), Crystal Research and Technology, **22**: p. 53-58.

[45] V.A. Fyedorov, A.G. Kan. R.P. Maksutov, Surface Strengthening of OIL & Gas Trade Facilities by Micro Arc Oxidation, VNIOENG, Moscow, (6) 1989.

[46] R. Arabal, E. Matykina, T. Hashimoto, P. Skeldon and G. E. Thompson Characterization of AC PEO coatings on magnesium alloys" (2009) Surface and Coatings Technology **203**: p. 2207-2220.

[47] J. A. Curran and T. W. Clyne, Porosity in plasma electrolytic oxide coatings (2006) Acta Materialia **54**: p. 1985-1993.

[48] A.L. Yerokhin, A. Shatrov, V. Samsonov, P. Shashkov, A. Pilkington, A. Leyland and A. Matthews, Oxide ceramic coatings on aluminium alloys produced by a pulsed bipolar plasma electrolytic oxidation process" (2005) Surface and Coatings Technology **199**: p. 150-157.

[49] W.B. Xue, X.L. Wu, X.J. Li, H. Tian, Anti-corrosion film on 2024/SiC aluminum matrix composite fabricated by microarc oxidation in silicate electrolyte (2006) Journal of Alloys and Compounds **425** (1–2): p. 302-306.

[50] X. Nie, E. I. Meletis, J. Jiang A. Leyland and A. Matthews, Abrasive wear/corrosion properties and TEM analysis of Al2O3 coatings fabricated using plasma electrolysis (2002) Surface and Coatings Technology **149**: p. 245-251.

[51] V. V. Narulkar, S. Prakash, K. Chandra, "Ceramic coated Y1 magnesium alloy surfaces by microarc oxidation process for marine applications" (2007), Bull. Mater. Sci., **30**(4): p. 399–402.

[52] P. Kurze,W. Krysmann and H.G. Schneider, Anodic oxidation under spark discharge (ANOF). A new coating procedure in medical technology (1986), Zeitschrift fur Klinische Medizin **41[3]**: p. 219-222.

[53] G. Sundararajan, L. Rama Krishna, "Mechanisms underlying the formation of thick alumina coatings through the MAO coating technology" (2003) Surface and Coatings Technology **167**: p. 269-277.

[54] F. Monfort, A. Berkani, E. Matykina, P. Skeldon,G.E. Thompson, H. Habazaki and K. Shimizu, A Tracer Study of Oxide Growth during Spark Anodizing of Aluminum (2005) Journal of The Electrochemical Society **152(6)**: p. C382-C387.

[55] X. Nie, L. Wang, E. Konca and A. Alpas, Tribological behaviour of oxide/graphite composite coatings deposited using electrolytic plasma process (2004) Surface and Coatings Technology **188–189**: p. 207-213.

[56] A.K. Vijh, Electrochemistry of metals and semiconductors, Marcel Dekker, New York, 1973, Chapter 5.

[57] E. Meletis, X. Nie, F. Wang and J. Jiang, Electrolytic plasma processing for cleaning and metal-coating of steel surfaces (2002) Surface and Coatings Technology **150**: p. 246-256.

[58] G.E. Thompson, H. Habazaki, K. Shimizu, M. Sakairi, P. Skeldon, X. Zhou and G. C. Wood, "Anodizing of aluminium alloys" (1999) Aircraft Engineering and Aerospace Technology, **71**: p. 228-238.

[59] A.L. Yerokhin, A.A. Voevodin, V.V. Lyubimov, J. Zabinski, M. Donley, "Plasma electrolytic fabrication of oxide ceramic surface layers for tribotechnical purposes on aluminum alloys (1998 Surface and Coatings Technology **110**: p. 140-146.

[60] E. Matykina, A. Berkani, P. Skeldon and G. E. Thompson, Real-time imaging of coating growth during plasma electrolytic oxidation of titanium (2007) Electrochimica Acta **53**: p. 1987-1994.

[61] S. Ikonopisov, A. Girginov and M. Machrova Electrical breaking down of barrier anodic films during their formation (1979) Electrochimica Acta **24(4)**: p. 45-456.

[62] N. Klein, "Electrical breakdown mechanisms in thin insulators" (1978) Thin Solid Films **50**: p. 223-232.

[63] J. M. Albella, I. Montero and J. M. Martinez-Duart, A theory of avalanche breakdown during anodic oxidation (1987) Electrochimica Acta **32**: p. 255-258.

[64] A. V. Epelfeld, V. B. Lyudin, O. N. Dunkin and O. S. Nevskaya 2000 Bull. Russ. Acad. Sci. Phys. 64: p. 610

[65] W. Krysmann, P. Kurze, K-H. Dittrich and H. G. Schnieder, (1984) Cryst. Res. Technol. **19**: p. 973

[66] A. Hickling and M. D. Ingram, "Contact glow-discharge electrolysis"(1964) Transactions of the Faraday Society **60**: p. 783-793.

[67] G. Sundararajan and L.R. Krishna, Mechanisms underlying the formation of thick alumina coatings through the MAO coating technology (2003) Surface and Coatings Technology **167**: p. (2–3) 269-277.

[68] L. Rama Krishna, K.R.C. Somaraju and G. Sundararajan, The tribological performance of ultra-hard ceramic composite coatings obtained through microarc oxidation (2003) Surface and Coatings Technology **163–164**: p. 484-490.

[69] R. McPherson, "Formation of metastable phases in flame- and plasma-prepared alumina" (1973) Journal of Material Science **8**: p. 851-858.

[70] D.H. Trinh, K. Back, G. Pozina, H. Blomqvist, T. Selinder, M. Collin, I. Reineck, L. Hultman and H. Högberg, Phase transformation in κ- and γ-Al2O3 coatings on cutting tool inserts (2009) Surface and Coatings Technology **203**: p. 1682-1688.

[71] J. Tian, Z. Luo, S. Qi, and X. Sun, "Structure and antiwear behavior of micro-arc oxidized coatings on aluminum alloy (2002) Surface and Coatings Technology **154**: p. 1-7.

[72] E.K. Tillous, T. Toll-Duchanoy, E. Bauer-Grosse, Microstructure and 3D microtomographic characterization of porosity of MAO surface layers formed on

aluminium and 2214-T6 alloy (2009) Surface and Coatings Technology **203**: p. 1850–1855.

[73] G. S. Selwyn, Optical Diagnostic Techniques for Plasma Processing. AVS Press, New York, 1993.

[74] J.E. Sansonetti and W.C. Martin, Handbook of Basic Atomic Spectroscopic Data, (2005) Journal of Physical and Chemical Reference Data, **34** [4]: p. 1559-2260.

[75] http://physics.nist.gov/cgi-bin/ASD.

[76] H. R. Griem, Principles of Plasma Spectroscopy, Cambridge University Press, 1997.

[77] V. M. Donnelly, in Plasma Diagnostics (O. Auciello and D. L. Flamm, eds.). Vol. I, Chapter 1, p. 1. Academic Press, Boston, 1989.

[78] N. P. Sluginov, (1880) J. Rus. Chem. Soc. **12**, 1-2: p.193.

[79] A. Gunterschultze and H. Betz, Electrolytkondensatoren (Berlin: Krayn) 1937.

[80] A. Despic, V. Parkhutik, in: D.H. Desty, K.T. Gillen, B.E. Conway (Eds.), Modern Aspects of Electrochemistry, Vol. 20, Plenum press, New Yourk, 1989, p. 401.

[81] X. Li, X. Nie, L. Wang, D.O. Northwood, "Corrosion protection properties of anodic oxide coatings on an Al–Si alloy" (2005) Surface and Coatings Technology **200**: p.1994-2000.

[82] M. Klapkiv, N. Povstyana and H. Nykyforchyn, " Production of conversion oxide-ceramic coating on zirconium and titanium coatings" (2006) Materials Science **42** [2]: p. 277-286.

[83] V. M. Pusuvailo, "Analysis of the radiation spectra in the process of synthesis of zirconium oxide in an electrolytic plasma (2001) Materials Science **37** [4]: p. 677-679.

[84] D. Kharitonov, Y. Betcevich, G. Novikov and A. Fridman, On the mechanism of impulse electrolytic spark oxidation of aluminium in concentrated sulphuric acid, (1988) TcNIIAtomInform, (Moscow, 16p).

[85] M. Klapkiv, H. Nykyforchyn and V. Pusuvailo, "Simulation of synthesis of oxide-ceramic coatings in discharge channels of a metal-electrolyte system" (1999) Materials Science **35** [2]: p. 279-283.

[86] H. Nykyforchyn, M. Klapkiv and V. Posuvailo, "Properties of synthesised oxide-ceramic coatings in electrolyte plasma on aluminum alloys" (1998) Surface and Coating Technology **100-1001**: p. 219-221.

[87] M. Klapkiv, H. Nykyforchyn and N. Povstyana, "Spectral analysis of electrolytic plasma during oxides synthesis on aluminum (1994) Materials Science **30** [3]: p. 70-81.

[88] W. Dietzel, M. Klapkiv, H. Nykyforchyn and N. Povstyana and C. Blawert"Porosity and corrosion properties of electrolyte plasma coatings on magnesium alloys" (2004) Materials Science **40** [5]: p. 585-590.

[89] R.W. Revie, Uhlig's Corrosion Handbook, (2nd edition), John Wiley & Sons, New York, 2000.

[90] D. J. Jones, Principle of prevention of corrosion(2nd Edition), Prentice-Hall, Inc., USA. 1996.

[91] B. Welz and M. Sperling, Atomic Absorption Spectrometry (Weinhein: Wiley-VCH) 1999.

[92] J. M. Mermet Inductively Coupled Plasma Spectrometry and its Applications, Ed. Hill S J (Sheffield: Sheffield Academic Press) 1999.

[93] X. Nie, A. Wilson, A . Leyland and A. Matthews, Deposition of duplex Al_2O_3/DLC coatings on Al alloys for tribological applications using a combined micro-arc oxidation and plasma-immersion ion implantation technique (2000) Surface and Coatings Technology **121**: p. 504-513.

[94] P. Su, X. Wu, Y. Guo and A. Jiang, "Effects of cathode current density on structure and corrosion resistance of plasma electrolytic oxidation coatings formed on ZK60 Mg alloy" (2009) J. Alloys Compd **475**: p. 773-777.

[95] W. Xue, C. Wang, R. Chen and Z. Deng, "Structure and properties characterization of ceramic coatings produced on Ti–6Al–4V alloy by microarc oxidation in aluminate solution" (2002) Mater. Lett. **52**: p. 435-441.

VITA AUCTORIS

NAME: Riyad Hussein

PLACE OF BIRTH: Baghdad, Iraq

YEAR OF BIRTH: 1963

Education: from Baghdad University

                                 1981-1985 B.Sc. in Physics

                                 Strathclyde University, U.K.

                                 1986-1990, PhD in Plasma physics

                                 University of Windsor, Canada

                                 2008-2010, M. A. Sc.